



UNIVERSITÀ
DEGLI STUDI
FIRENZE

INTERNATIONAL DOCTORATE IN

Atomic and Molecular Photonics

CICLO XXVIII

COORDINATORE Prof. Roberto Righini

QUANTUM EMITTERS NEAR METALLIC INTERFACES

Settore Scientifico Disciplinare FIS/03

Dottoranda

Dott. Sahrish Rizvi

Tutore

Dott. ssa Costanza Toninelli

Coordinatore

Prof. Roberto Righini

Anni 2012/2015

Acknowledgements

First of all, I would like to thank my supervisor, Dr. Costanza Toninelli, for giving me the opportunity to work in her research group. Her scientific enthusiasm and attention to detail will always be an inspiration to me. Further, I would like to thank her for her patience with me during our many discussions. I would also like to thank Prof. Francesco Saverio Cataliotti for sharing his expertise and his support during the last three years.

I wish to give my thanks to the many people I had the opportunity to work with, at LENS and at the Physics Department in Polo Scientifico. I am deeply grateful for the friendships I forged in Lab 66. I would like to thank Andrea Tabani for teaching me the nuances of experimental physics, Pietro Lombardi for his ever-ready nature to help (and entertain) everyone, and Fabrizio Sgrignuoli for his friendly persona. Thanks to Cosimo Lovecchio for being a source of laughter in the lab and Sofia Pazzagli for our countless discussions about everything! Special thanks to Giacomo Mazzamuto for his enormous support in and out of lab, and I hope Simona Checcucci always retains her sweet nature. (Please note that) the above-mentioned people are very talented scientists and it would not have been possible to finish this thesis without their help and support. I really wish them the best with their careers. I would also like to give my thanks to Maria Maccari and Frederik Dieleman for the pleasant working atmosphere in the lab.

It was an absolute pleasure working with Sara Nocentini for various experiments and I thank her for her help for sample fabrication and related things. I also thank Lorenzo, Eva, Francesco S, Francesco B, Hao, Hua, Dmitry for their company during my time here. Special mention to Riccardo Tani who helped me to navigate the official issues.

I would like to thank my family and friends in India whose love and support has kept me going through all the happy and difficult times I have faced. I wish to dedicate this thesis to them.

Contents

General Introduction	7
1 Theoretical background	13
1.1 Emitter-field interaction	13
1.2 Dynamics of a Two-level system	15
1.3 Dynamics of a Three-level system	20
1.4 Fluorescence near Interfaces	23
2 Experimental setup	29
2.1 Single molecule detection	29
2.1.1 Confocal microscope	32
2.2 Hanbury-Brown and Twiss Setup	35
2.3 Experimental upgrades of the setup	39
2.3.1 Back-focal plane imaging	39
2.3.2 Kretschmann configuration	41
2.3.3 Raman spectroscopy of Graphene	44
3 Emitter System	47
4 Angular emission patterns in multilayer systems	55
4.1 Design principle	56
4.2 Reference sample	62
4.3 Planar optical antennas	64
4.3.1 One mirror configuration	65
4.3.2 Two mirror configuration	71
4.4 Outlook	78
5 Coupling to surface plasmons	79
5.1 Introduction	79
5.1.1 Properties of surface plasmon polaritons	79
5.1.2 SPP excitation	82
5.2 Crossing over from weak coupling to strong coupling	85
5.3 DBT molecules on a flat gold surface	87
5.4 Plasmonic concentric-ring resonators	93
5.5 Plasmonic waveguides	97

6 Coupling to Lossy waves in Graphene	101
6.1 Introduction	101
6.2 Graphene-DBT coupling	102
6.3 Experimental details	105
6.4 Results and discussion	107
Bibliography	111
List of figures	126

General Introduction

In the field of optics, the determination of dipole radiation in planar layered media is of significance for many areas of research. It is encountered in fundamental research activities such as antenna design, cavity quantum electrodynamics, and molecular spectroscopy, as well as in applications among which is, the design of integrated electro-optic circuits, surface electrochemistry, development of display technology, quantum computing and so on. Even while considering a simple case, the presence of a single interface in the vicinity of an emitter can significantly perturb its emission properties: first, by modifying the boundary conditions of the electromagnetic (em) field, it may alter both the radiative decay rate and the spatial distribution of the emitted radiation; and second, the excited molecule may lose its energy to the interface via non-radiative energy transfer [1]. It is the purpose of this thesis work to understand the concepts and elucidate the underlying physics behind the processes mentioned above, and to discuss recent results and current problems faced in the laboratory.

In the weak coupling regime, the perturbation induced by the interface can be determined by Fermi's golden rule [2]: $\Gamma_{ij} \propto |M_{ij}|^2 \rho(E)$ where Γ_{ij} is the rate of transition from state i to state j , M_{ij} is the transition element connecting the said states and is determined by the wavefunctions associated with those states, and $\rho(E)$ is the density of optical modes at the transition frequency. This control of the spontaneous emission rate was first pointed out by Purcell in 1946 [3]. This relation is a testament to the fact that the decay rate of an emitter is not an absolute quantity but rather a function of its interaction with the environment. Also non-radiative decay processes often compete with radiative decay and affect the net decay rate of the emitter's excited state.

Pioneering experiments were carried out by Drexhage and co-workers [4] where they observed decay rates of Eu^{3+} ions placed in the vicinity of a silver mirror as a function of the distance d between the emitter and the surface. Here the dipole can be considered as a forced damped oscillator that is driven by the radiation field of the dipole moment reflected by the interface. At the dipole position, the reflected field results in the modification of the photonic density of states and hence the transition rate of the emitter dipole. Since both the magnitude and phase of the reflected field is distance-dependent, so is the modification in decay rates.

In the near-field of the dipole, i.e. at distances comparable to the emission wavelength, there exist a wide range of wavevectors some of which have a higher in-plane component compared to the net amplitude of the wavevector, and hence give rise to *stationary* evanescent waves in the near-field. Thus, in addition to coupling to photonic

modes, the dipole can also couple to other modes on the interface (particularly a metal interface), which have a higher in-plane momentum compared to freely propagating waves, provided that the evanescent field of the dipole is brought within the interaction distance from the interface. Such a coupling gives rise to hybrid light-matter modes on the metal surface called surface plasmon polaritons (SPPs). These are confined to the surface and decay exponentially in the transverse direction due to their evanescent nature. The surface field enhancement coupled with the confinement of SPP modes in tiny mode volumes on metal surfaces has enabled the observation of a characteristic interaction regime in which many quantum emitters reversibly exchange energy with the plasmon field. In fact, even ultra strong coupling has been achieved between photochromic molecules and plasmonic structures at room temperatures, without the need for closed cavities [5].

When the dipole emitter is brought within still smaller separations from the interface, for example $d \leq 20$ nm, direct energy transfer to *lossy surface waves* can take place, and a strong distance-dependent quenching sets in due to the presence of the additional non-radiative decay channel. The energy transfer can excite, for example, electron-hole pairs in the metal layer, that are dissipated through scattering in the substrate.

In this work, we systematically study light-matter interaction in the different distance-dependent regimes as described above. In particular we consider the optical properties of single emitters closed to structured interfaces, because of their relevance as integrated single photon sources and nanoscopic sensors. Nowadays, quantum emitters are widely used as single photon sources, those including single atoms or ions, quantum dots, colour centers in diamonds, fluorescent molecules, carbon nanotubes etc [6]. Even though the choice of a source depends on the application and the wavelength of operation, in general, an optical source is required to be stable, robust and easy to use. Dibenzoterrylene (DBT) dye molecules embedded in anthracene (Ac) used in this work present a viable option for realisation as single photon sources at both room and low temperatures, with a quantum yield of almost unity and very low blinking and photobleaching rates. The relatively easy fabrication techniques compared to other sources and the fixed orientation of the transition dipole of DBT molecules parallel to one of the crystal faces of anthracene, facilitate the modelling and utilisation of these emitters in quantum optics experiments.

This thesis has been organised in six chapters, which are summarized as follows:

Chapter 1 first presents a broad theoretical framework that allows us to model the emitter-field interaction and quantify the dynamics of the emitters used in this thesis. In particular we see how the results obtained by the quantum two-level atom approximation can be extended to explain dipole transitions in solid-state matter in the presence of a resonant excitation field. The concept of Rabi oscillations is introduced, where the populations of the atom states oscillate coherently due to interaction between atom and field. But in real systems, damping mechanisms such as spontaneous decay of the emitter and pure dephasing mechanisms can destroy the coherence of such

oscillations and this results in the broadening of the transition lineshape instead of a sharp transition at a single resonant frequency. This is particularly true for solid-state systems at room temperatures that exhibit very high dephasing rates. Thus, decay rates for two-level and three-level emitters are determined through rate equations that include damping, where the non-linear behaviour of the quantum system is underlined resulting in saturation of the excited state. The final part of the chapter introduces the scenario of a dipole situated near an interface, in particular a metallic interface, in which different coupling mechanisms that take place depending on the dipole-interface distance are enumerated. These coupling mechanisms are discussed in detail in later chapters.

Chapter 2 explains in detail the experimental setup that was used for characterization and measurements undertaken during this work. Here we explore the methods to accomplish single molecule detection using a confocal microscope which has the capability to address diffraction-limited microscopic volumes. I was actively involved in the assembly of the home-built inverted epifluorescence scanning microscope which can be used both in a wide-field and confocal configuration for identification and measurement from single molecules. The optical setup is coupled to an EM-CCD camera, spectrometer and APDs for detection, and is capable of performing various measurements both at room temperature and at cryogenic temperatures by making use of a closed-cycle cryostation. The optical properties measured at room temperature include photoluminescence intensity, fluorescence saturation intensity and lifetimes of DBT molecules, while lifetime-limited Zero-phonon line measurements are done at cryogenic temperatures. The APDs are arranged in a Hanbury-Brown Twiss arrangement and can perform second-order correlation measurements $g_2(t)$, where single-photon emission from single DBT molecules is characterised by an antibunching dip - a clear sign of the quantum nature of radiation. This chapter also discusses about the additional upgrades that we made to the experimental setup for the study of specific optical properties/phenomena, such as measurement of the angular emission pattern of molecules, excitation of surface plasmons over planar gold films, and measurement of Raman spectrum of graphene monolayer specimens.

Chapter 3 is dedicated to the optical characterization of the emitter system chosen for this thesis work: Dibenzoterrylene (DBT) molecules embedded in anthracene (Ac) performed using the experimental setup described in the previous chapter. The DBT:Ac system exhibits excellent emitter stability and high saturation count rates which is favourable for low-noise single molecule experiments. I take special interest in the preparation and fabrication of DBT:Ac samples, in which I'm assisted by my previous research experience. Two fabrication techniques for obtaining DBT:Ac crystals are described, which result in crystals having different physical properties appropriate for different experimental scenarios.

In **Chapter 4** we first present a theoretical model that describes the angular emission characteristics of dipole emitters embedded inside a multilayer structure. In particular,

we study how the emission patterns are modified in the presence of a gold reflective layer where absorptions have also been taken into account. The effect of different layers on the dipole emission is modeled in terms of their Fresnel reflection and transmission coefficients and various multilayer configurations are explored. The reflected signals at multiple interfaces can give rise to interferences, and this property can be exploited to design specific emission patterns in wavevector-space. By comparing the radiated power as a function of polar angles w.r.t. the optical axis, this study has led to the development of powerful yet simple multilayer structures that perform as planar optical antennas which are extremely efficient in collecting the radiation emitted by the embedded dipole source into a narrow range of polar angles, thus enabling efficient interfacing with low numerical aperture optics such as optical fibers. The versatile simulation code was developed and programmed in MATLAB by my colleague Miss Simona Checcucci and I was involved in the fabrication and experimental investigation of the designed structures. The results obtained through this work have enormous potential in a wide range of applied and basic sciences ranging from quantum optics experiments and optical information transfer to fluorescence detection in biological samples.

Chapter 5 deals with the study of surface plasmons on gold surfaces. First, properties of SPPs are elaborated in relation to the dispersion relation, alongwith their dissipation properties due to ohmic losses in the metal. Surface plasmons are characterised by an in-plane momentum that is higher than the one for propagating em waves in free space. This property induces the need for excitation schemes that can increase and match the wavevector of excitation light with the surface plasmon wavevector. Several such schemes have been enlisted out of which two are utilised in this work, namely the Kretschmann configuration and near-field coupling with molecules. Next, we address the theoretical description of *strong coupling* between quantum emitters and surface plasmons and discuss about the various factors affecting its experimental observation, including the problems specific to the our system (at a later stage in the next section). First a simple configuration was tested for observing coupling of molecules to surface plasmons, comprising of DBT:Ac layers spin coated over a planar gold thin film. The coupling bewteen molecules and plasmons is verified in various ways including the observation of surface plasmon coupled emission (SPCE) at the plasmon angle, enhanced decay rates due to the additional decay channel into plasmons, and by obtaining the attenuated total reflectometry measurements in the Kretschmann configuration. Additionally, plasmonic nanostructures are known to achieve a higher degree of mode confinement than planar films and three geometries were chosen for experiments considering their potential for increased emitter-field interaction: plasmonic concentric-ring nanocavities, and wedge and channel waveguides. The nanocavities can support localised surface plasmon modes as opposed to propagating ones and result in deep subwavelength confinement to provide high Purcell enhancements. The waveguides combine high mode confinement with moderate propagation lengths and are potential candidates for observing long-range intermolecular coupling through propagating plas-

mons. The work regarding the above-mentioned plasmonic structures is in progress, and only the ring cavities and wedge waveguides are mentioned in this text.

As mentioned earlier, when the molecule is brought within nanometric distances to the metallic interface, the decay of the molecular excited state can happen via coupling to several loss mechanisms on the surface. In **Chapter 6**, we demonstrate the coupling mechanism that occurs when DBT molecules are interfaced with an undoped graphene monolayer sheet. Undoped graphene is considered a semi-metal due to its gapless band structure and exhibits a nearly constant absorption across the visible spectral region. The characterization of the graphene monolayer sample was done with Raman spectroscopy. With the particular sample configuration used in this work, excited DBT molecules relax through energy transfer which creates electron-hole pairs in graphene. Such non-radiative energy transfer is similar to Förster resonance energy transfer (FRET) mechanism between dipoles, and results in quenching of the molecular fluorescence and an enhanced total decay rate. In this work, we perform a statistical analysis of the fluorescence lifetimes obtained from single DBT molecules in the vicinity of the graphene layer and compare them with lifetimes of molecules in a reference configuration. The extracted lifetime distributions are compared to an analytical model that describes this interaction following a d^{-4} distance-dependence, with other parameters being universal constants. Being dependent only on the emitter-graphene distance, this system can be exploited as a ruler capable of measuring distances at the nanoscale.

1 Theoretical background

1.1 Emitter-field interaction

In this section, mainly a semi-classical approach is taken to explain light-matter interaction in which the atoms and molecules are treated as quantum-mechanical objects while the light is treated as a classical electromagnetic(em) wave, and is consistent with the fully-quantum description for the systems discussed in this thesis.

Quantum mechanically, atoms and molecules are described as multi energy-level systems. Each energy level corresponds to a state $|i\rangle$ and the difference in energy between two subsequent levels is written in terms of frequency as:

$$\Delta E_{ji} = E_j - E_i = \hbar\omega_{ji} \quad (1.1)$$

where $E_i = \hbar\omega_i$ is the quantized energy of the i -th energy level and $E_j > E_i$.

For many physical considerations, it is sufficient to account for only two of the possible energy eigenstates, since for most experimental cases a monochromatic laser source is used to probe a quantum emitter. If the laser frequency ω coincides with only one of the optical transitions, light-matter interaction can be expressed in terms of the *two-level atom approximation*. In this approximation, the quantum system can be treated as a simple two-level atom with eigenstates $|1\rangle, |2\rangle$ and energies E_1, E_2 with $|E_2 - E_1| = \hbar\omega_0$; all other energy levels, being far from resonance, only weakly interact with light and are hence neglected. In the case of molecules in condensed states with multiple energy levels, it is possible to treat the resonant transition as an independent two-level atom in the presence of a bath of phonons.

In 1913, Bohr postulated that a quantum of light is absorbed or emitted whenever an atom jumps between two quantised levels, the angular frequency of the light satisfying the relation: $E_2 - E_1 = \hbar\omega$, as illustrated in figure 1.1. In this picture, the absorption process is viewed as the destruction of a photon from the incident light beam with simultaneous excitation of the atom, while the emission process corresponds to the addition of a photon to the light field and the simultaneous de-excitation of the atom. Although this basis assumes a quantum nature of both atom and radiation, the processes of absorption and emission are being discussed here only in a phenomenological way.

The processes depicted above can be quantified in terms of *Einstein rate equations* [7]. Considering a system of total $N = N_1 + N_2$ atoms, where N_1 is the number of

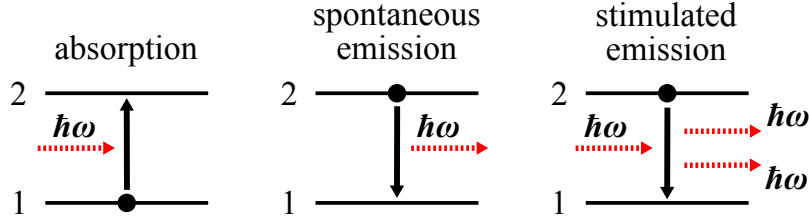


Figure 1.1: Schematic illustration of the absorption and emission processes.

atoms in the ground state and N_2 in the excited state at time t , the probability per unit time that, starting from a given state, a particular transition will take place is directly proportional to the number of atoms in that state. The *absorption* rate of the atomic transition from level 1 to 2 can be written as:

$$\frac{dN_1(t)}{dt} = -B_{12}^\omega N_1(t)\rho(\omega) \quad (1.2)$$

where B_{12}^ω is the Einstein B coefficient for absorption, and $\rho(\omega)$ is the spectral energy density of the em field at angular frequency ω .

The rate at which *spontaneous emission* occurs is governed by the Einstein A coefficient for the transition:

$$\frac{dN_2(t)}{dt} = -A_{21}^\omega N_2(t) \quad (1.3)$$

This equation can be solved for $N_2(t)$ to give:

$$N_2(t) = N_2(0)\exp(-A_{21}t) \equiv N_2(0)\exp(-t/\tau) + c \quad (1.4)$$

where $\tau = 1/A_{21}$ is the *radiative lifetime* of the excited state. However, as will be discussed shortly, the spontaneous emission rate of an atom is not an absolute quantity but can in fact be controlled by modifying the density of photonic states available to the atom.

The incoming light field can also induce downward transitions from the excited state in addition to upward absorption transitions. The *stimulated emission* rate is specified by the second Einstein B coefficient B_{21} , and is given by:

$$\frac{dN_2(t)}{dt} = -B_{21}^\omega N_2(t)\rho(\omega) \quad (1.5)$$

Stimulated emission is a coherent quantum-mechanical effect where the photons emitted are in phase with the incident radiation.

In the steady state, due to thermal equilibrium, the rate of upward transitions balances the rate of downward transitions, which gives:

$$B_{12}^\omega N_1\rho(\omega) = A_{21}N_2 + B_{21}^\omega N_2\rho(\omega) \quad (1.6)$$

The ratio of steady state populations at temperature T is given by Boltzmann's law:

$$\frac{N_2}{N_1} = \frac{g_2}{g_1} e^{-\hbar\omega/k_B T} \quad (1.7)$$

where g_1 and g_2 are the degeneracies of levels 1 and 2 respectively. By substituting the energy density given by Planck formula, we find:

$$(g_1 B_{12}^\omega = g_2 B_{21}^\omega) \equiv (B_{12}^\omega = B_{21}^\omega) \text{ for a non degenerate atom} \quad (1.8)$$

$$\text{and,} \quad A_{21} = \frac{\hbar\omega^3}{\pi^2 c^3} B_{21}^\omega \quad (1.9)$$

These equations suggest that transitions with high absorption probability also have a high probability for emission, both spontaneous and stimulated.

Einstein's analysis is however, only limited to *statistical mixtures*, where the atom can either be in level 1 or level 2 (but not both) at one time. It is known that quantum systems can exhibit wave function interference and give rise to *mixed states*, and they can be represented by a density matrix [8], which takes the form:

$$\rho = \begin{pmatrix} \rho_{11} & \rho_{12} \\ \rho_{21} & \rho_{22} \end{pmatrix} \quad (1.10)$$

where the diagonal elements, ρ_{11} and ρ_{22} , represent populations and give the measurement probability for the system to be in the ground and excited states respectively. The off-diagonal elements, ρ_{12} and $\rho_{21} = \rho_{12}^*$ account for the interference between these states and are thus referred to as *coherences*. They represent the *joint* probability of finding the system in those states.

1.2 Dynamics of a Two-level system

To study the transient dynamics of the atom-field interaction, the main objective is then to solve the time-dependent Schrödinger equation for the atom in presence of the light:

$$\hat{H} = \hat{H}_{\text{atom}} + \hat{H}_{\text{field}} + \hat{H}_{\text{int}} \quad (1.11)$$

where \hat{H}_{int} is the interaction Hamiltonian. Here, considering that the driving em field is sufficiently strong and remains largely unaffected by the atom, it can be neglected from the dynamics of the coupled system and considered as a *reservoir*. Thus equation 1.11 can be reduced to:

$$\hat{H} = \hat{H}_{\text{atom}} + \hat{H}_{\text{int}} \quad (1.12)$$

which divides the Hamiltonian into a time-independent part $\hat{H}_0 (= \hat{H}_{\text{atom}})$ which describes the atom in the dark and a time-dependent interaction term.

In many problems, \hat{H}_{int} can be considered as a perturbation and thus the calculation of radiative transition rates by quantum mechanics is based on time-dependent perturbation theory. The light-matter interaction is described by transition probabilities, which can be calculated for the case of spontaneous emission using *Fermi's golden rule* [2]. According to this rule, the transition rate is given by:

$$\Gamma_{1 \rightarrow 2} = \frac{2\pi}{\hbar} |\langle 2 | \hat{H}_{\text{int}} | 1 \rangle|^2 \rho(E) \quad (1.13)$$

where $\rho(E)$ is the density of final states defined so that $\rho(E)dE$ is the number of final states per unit volume within the range $(E, E + dE)$.

Note that equation 1.13 is derived via first order perturbation theory, thus it is always valid when light and matter interact weakly. In the case of strong laser fields, Fermi's golden rule holds when the time of the measurement is much larger than the time needed for the transition.

The transition rate given by equation 1.13 is mostly due to the electric dipole transition in an atom, since the transition rates for magnetic and other higher order polarities are reduced by several orders of magnitude. Moreover, atoms are small compared to the wavelength of excitation light and the amplitude of the field does not vary significantly over the dimensions of the atom. This is called the *electric dipole approximation*.

In the semi-classical approach, the perturbation is given by the energy shift of the atomic dipole due to the time-dependent electric field $E(t)$ of excitation light:

$$\hat{H}_{\text{int}}(t) = -\hat{p} \cdot E(t) \quad (1.14)$$

where the atomic dipole $\hat{p} = -e \cdot \hat{r}$, \hat{r} being the position operator. The dipole matrix element μ_{12} can be defined as:

$$\mu_{12} = -e \langle 2 | \hat{r} | 1 \rangle \quad (1.15)$$

Thus for an electric field $E(t)$ given by $E(t) = E_0 \cos \omega t$, the perturbation matrix element $\langle 2 | \hat{H}_{\text{int}} | 1 \rangle$ is given by:

$$H_{12}(t) = -\frac{E_0}{2} (e^{i\omega t} + e^{-i\omega t}) \mu_{12} \quad (1.16)$$

This can be further written as:

$$H_{12}(t) = -\frac{\hbar\Omega}{2} (e^{i\omega t} + e^{-i\omega t}) \quad (1.17)$$

where $\Omega = |\mu_{12}E_0/\hbar|$ is the *Rabi frequency* and is associated with the strength of the atom-field coupling.

Now the Schrödinger equation for an unperturbed two-level atom can be written as:

$$\hat{H}_0 \Psi_i = i\hbar \frac{\partial \Psi_i}{\partial t} \quad (1.18)$$

whose solution is given by:

$$\Psi(\mathbf{r}, t) = c_1(t)\psi(\mathbf{r})e^{-iE_1t/\hbar} + c_2(t)\psi(\mathbf{r})e^{-iE_2t/\hbar} \quad (1.19)$$

where $|c_i|^2 = \rho_{ij}$ for $i = j$ and $c_i c_j^* = \rho_{ij}$ for $i \neq j$, relating them to terms from the atom density matrix (defined in equation 1.10). Substituting the solutions for \hat{H}_0 and \hat{H}_{int} in equation 1.12, for non-resonant coupling, we eventually get:

$$\frac{dc_1(t)}{dt} = \frac{i\Omega}{2}(e^{i(\omega-\omega_0)t} + e^{-i(\omega+\omega_0)t})c_2(t) \quad (1.20)$$

$$\frac{dc_2(t)}{dt} = \frac{i\Omega}{2}(e^{-i(\omega-\omega_0)t} + e^{i(\omega+\omega_0)t})c_1(t)$$

In the rotating wave approximation¹ the higher frequency terms $\omega + \omega_0$ are neglected. Moreover in realistic systems, there exist decoherence mechanisms which hamper the Rabi oscillations. The resulting equations of motion for the density matrix elements can be obtained by solving the master equation which includes the losses due to these decoherence mechanisms in Lindblad form and are given as (calculation not shown):

$$\frac{d\rho_{22}}{dt} = -\frac{d\rho_{11}}{dt} = \frac{i\Omega}{2}(\tilde{\rho}_{21} - \tilde{\rho}_{12}) - \Gamma\rho_{22} \quad (1.21)$$

$$\frac{d\tilde{\rho}_{12}}{dt} = \frac{d\tilde{\rho}_{21}^*}{dt} = \frac{i\Omega}{2}(\rho_{11} - \rho_{22}) - (\gamma_C + i\Delta)\tilde{\rho}_{12} \quad (1.22)$$

where $\Delta = \omega - \omega_0$ is the atom-field detuning, $\Gamma = 1/\tau$ is the excited-state population decay rate and γ_C is the coherence damping rate.

Damping is the process of destroying the coherences of the superposition states of the atomic system. It occurs through two distinct mechanisms: population decay and population-conserving scattering processes, i.e. *pure dephasing* processes arising from interactions with the environment and characterized by a dephasing time T_2' . The resultant decoherence time $T_2 = 1/\gamma_C$ is given by:

$$\frac{1}{T_2} = \frac{1}{2\tau} + \frac{1}{T_2'} \quad (1.23)$$

and determines the linewidth (full-width at half-maximum) of the transition:

$$\Delta\omega = 2\gamma_C = \frac{1}{\tau} + \frac{2}{T_2'} \quad (1.24)$$

that describes the broadening of the transition lineshape.

In the absence of collisional damping, equation (1.24) reduces to the *lifetime-limited* linewidth $\Delta\omega_{\text{nat}} \equiv 1/\tau = \Gamma$ and the lineshape exhibits an intrinsic *homogeneous* broadening with a Lorentzian profile.

¹This approximation holds for $\omega \gg \Omega$ and $|\omega - \omega_0| \ll \omega + \omega_0$, i.e. the rapidly oscillating terms with frequency $\omega + \omega_0$ can be neglected in the Hamiltonian \hat{H} . In the rotating frame of the Bloch vector, populations don't change while coherences become $\tilde{\rho}_{21} = \rho_{21}e^{i\omega t}$

Figure 1.2 shows excited state populations for different values of the damping rate. For most quantum systems in condensed matter, the environment strongly affects the photophysics of the emitter. At room temperature, optical transitions involve phonons and are inhomogeneously distributed over a broad range of frequencies. In this case,

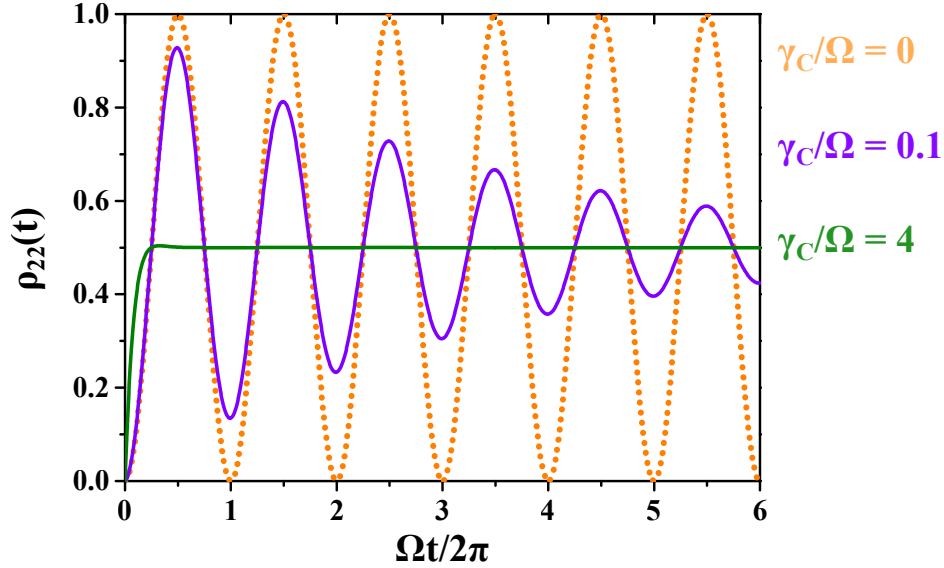


Figure 1.2: Excited-state population behaviour at resonant excitation ($\Delta = 0$) for different values of the damping rate γ_C . All the curves for non-zero damping tend to a steady-state value. The dotted curve shows the oscillations when no damping is present.

the dephasing time T_2' is shorter than the excited-state lifetime τ by several orders of magnitude and a strong damping sets in ($\gamma_C \gg \Gamma, \Omega$). This means that coherences will be damped very quickly, whereas the populations will continue to evolve on much longer timescales. Coherences can thus be considered null in equilibrium, i.e. $d\tilde{\rho}_{ge}/dt \sim 0$, and the dynamics depend solely on the population decay:

$$\frac{d\rho_{22}}{dt} = -\frac{d\rho_{11}}{dt} = -\frac{\Omega^2}{2\gamma_C(1 + \Delta^2/\gamma_C^2)}(\rho_{22} - \rho_{11}) - \Gamma\rho_{22} \quad (1.25)$$

With the following substitutions,

$$\rho_{22} = N_2/N, \quad \rho_{11} = N_1/N, \quad \Gamma = A_{21}$$

equation (1.25) is comparable to the combined Einstein rate equations for $N = N_1 + N_2$ atoms:

$$\frac{dN_2}{dt} = -\frac{dN_1}{dt} = -A_{21}N_2 - B_{21}\rho(\omega)(N_2 - N_1) \quad (1.26)$$

Summed over all frequencies, total energy density becomes $\rho = I/c$ where I is the intensity of the driving em field. Then the equation above is modified:

$$\frac{dN_2}{dt} = -A_{21}N_2 - \sigma(\omega)\frac{I}{\hbar\omega}(N_2 - N_1) \quad (1.27)$$

where $\sigma(\omega)$ is the *absorption cross-section* [9], defined as:

$$\sigma(\omega) = \frac{A_{21}\lambda^2}{4}s(\omega) \quad (1.28)$$

for the em field wavelength λ and the lineshape function $s(\omega)$. The cross-section has the dimensions of area, and is defined such that $\sigma(\omega)I$ is the power absorbed by a single atom when irradiated by intensity I .

In the other limit, if the electric field is increased to very high values such that $\Omega > \gamma_C$, it is possible to observe Rabi oscillations in the populations of the upper and lower levels. In the strong-field limit, level populations can be approximated to:

$$\rho_{11} = \cos^2(\Omega t/2), \quad \rho_{22} = \sin^2(\Omega t/2) \quad (1.29)$$

For transitions in the visible-frequency range, experimental observation of Rabi flopping requires powerful laser beams. Another way to increase Rabi frequency ($\Omega = \mu_{12}E_0/\hbar$) is to increase the dipole element by using a coherent ensemble of many two-level systems. This approach would be discussed further in section 5.2.

To summarise, it can be stated that at low fields, we are in the strongly damped regime where there are discrete transitions and the Einstein analysis is valid. As the field is increased, the ratio of damping rate to the Rabi frequency decreases, and we can eventually reach the case where coherent oscillations are observable.

In the steady state with non-zero damping, the dynamics of the quantum emitter can be described by Einstein rate equations. Here $\gamma_{\text{spn}} = A_{21}$ and $\gamma_{\text{abs}} = B_{12} \equiv B_{21} = \gamma_{\text{stim}}$. The rate equations (1.26) for a two-level system interacting with a strong laser field can be written as:

$$\frac{d\rho_{22}}{dt} = -\frac{d\rho_{11}}{dt} = -\gamma_{\text{spn}}\rho_{22} - \gamma_{\text{abs}}(\rho_{22} - \rho_{11}) \quad (1.30)$$

Assuming that the system is driven to *saturate*, meaning that the excitation rate is equal to the spontaneous emission rate in the steady state, and then the excitation source is switched off after a reasonably long time. The excited state population decay is determined by the relation:

$$\rho_{22}(t) = \rho_{22}(t \rightarrow \infty)e^{-(\gamma_{\text{spn}}t)} \quad (1.31)$$

The population decay of the excited state is determined by measuring the radiated intensity in fluorescence experiments. Since the emitted photon rate is proportional

to the excited state population decay $\rho_{22}(t)$, the fluorescence intensity also decays exponentially as

$$I(t) = I(t_0)e^{-\gamma_{\text{spont}}t} \quad (1.32)$$

As fluorescence emission is a random process, only few emitters will emit their photons at precisely $t = \tau$ while the 63% of the emitters decay at shorter times and the 37% decay at $t > \tau$ [10].

1.3 Dynamics of a Three-level system

This thesis largely deals with the solid state quantum system made of DBT molecules embedded in a crystalline anthracene matrix. In this case, the energy levels of the emitters are more accurately described by a multi-level system as shown in the Jablonski diagram in figure 1.3. The electronic singlet states S_0 and S_1 are complemented by

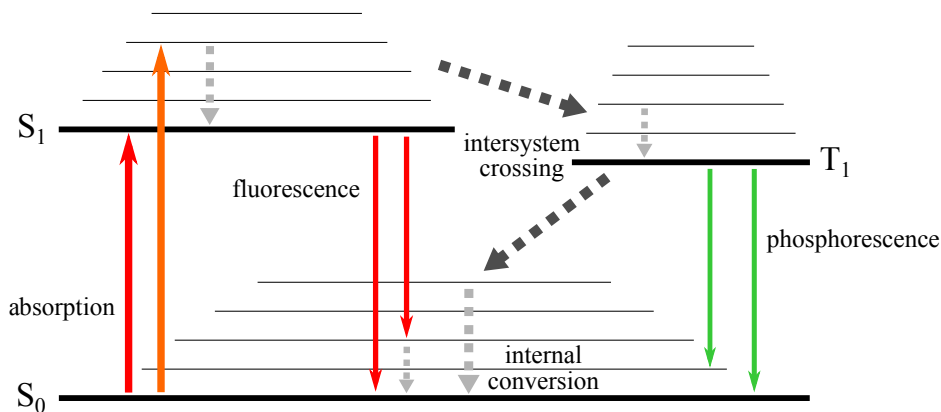


Figure 1.3: Jablonski diagram of a three-level molecule. S and T label the singlet and triplet electronic states respectively, above which vibrational levels are present for each state. Radiative transitions are represented by solid arrows while dashed arrows indicate non-radiative transitions.

a manifold of vibrational states, and transitions between them give rise to all the radiative and non-radiative processes depicted here. After excitation, the molecule quickly relaxes non-radiatively to the vibronic ground state of the first excited state (Kasha's rule [11]). This is called *internal conversion*, which occurs on the ps-timescale, involving the transition from an excited vibrational level to the ground vibrational level within the same electronic state. From here the molecule can decay either radiatively (*fluorescence*) or non-radiatively (dissipation to heat/phonons).

The singlet state S_1 and the triplet state T_1 have a different electron spin multiplicity, and the transition between them is *spin forbidden* and hence occurs with a low probability. *Intersystem crossing* is the radiationless process due to spin-orbit coupling and involves the transition between two almost iso-energetic electronic states with different

spin multiplicity. From the triplet state, the electron can decay back to one of the vibrational levels of S_0 either by non-radiative intersystem crossing followed by internal conversion, or it can decay radiatively into *phosphorescence*. Since this transition is spin forbidden too, it takes place with a lifetime in the ms-to-s-range, much longer than the fluorescence lifetime which is typically in the ns-range.

Similar to the two-level case, it can be considered that we operate in the strongly damped regime due to dissipative coupling to vibrations and pure dephasing mechanisms, and derivations for the transition rates can be made. Labelling the additional triplet state as level 3, and neglecting stimulated emission, the rate equations are given as:

$$\frac{d}{dt}\rho_{11}(t) = -\gamma_{abs}\rho_{11}(t) + (\gamma_{spon} + \gamma_{nr})\rho_{22}(t) + \gamma_{31}\rho_{33}(t) \quad (1.33)$$

$$\frac{d}{dt}\rho_{22}(t) = \gamma_{abs}\rho_{11}(t) - (\gamma_{spon} + \gamma_{nr} + \gamma_{23})\rho_{22}(t) \quad (1.34)$$

$$\frac{d}{dt}\rho_{33}(t) = \gamma_{23}\rho_{22}(t) - \gamma_{31}\rho_{33}(t) \quad (1.35)$$

$$1 = \rho_{11}(t) + \rho_{22}(t) + \rho_{33}(t) \quad (1.36)$$

where equation 1.36 means that the emitter is in one of the three states at any time. Intersystem crossing can be neglected in a first rough approximation, since it occurs with a low probability as mentioned above. For the specific system analysed in this thesis, the intersystem crossing branching ratio is about 10^{-7} .

The presence of a non-radiative decay channel modifies the excited state lifetime τ and it is given by:

$$\tau = \frac{1}{\gamma_{spon} + \gamma_{nr}} \quad (1.37)$$

and the ratio of the radiative decay rate and the total decay rate $\Gamma = 1/\tau$ is denoted as the quantum efficiency of the molecule:

$$Q = \frac{\gamma_{spon}}{\gamma_{spon} + \gamma_{nr}} \quad (1.38)$$

Using these relations, the molecular photon emission rate is given by:

$$N(t) = \Gamma\rho_{22}(t)Q \quad (1.39)$$

Solving for the population ρ_{22} using equations 1.33 through 1.36, for a constant source intensity I , we find that:

$$N(I) = N_{\infty}\left(\frac{1}{1 + I_{sat}/I}\right) \quad (1.40)$$

where N_{∞} describes the emission rate at infinitely strong intensities and I_{sat} is the intensity when saturation sets in and emission rate is equal to $N_{\infty}/2$. They are char-

acterising values for a given emitter and are defined as:

$$N_{\infty} = \frac{\gamma_{31}\gamma_{spon}}{\gamma_{23} + \gamma_{31}} \quad (1.41)$$

$$I_{sat} = \frac{(\Gamma + \gamma_{23})\gamma_{31}}{\sigma(\gamma_{23} + \gamma_{31})} \hbar\omega \quad (1.42)$$

for an absorption cross-section σ . In the absence of intersystem crossing, I_{sat} can be approximated to:

$$I_{sat} = \frac{\hbar\omega_0}{2\sigma_0\tau} \quad (1.43)$$

This kind of saturation behaviour described above is a consequence of the finite lifetime of the excited state, which limits the average time between two photo-emissions to a finite value and prevents it from emitting at arbitrarily high rates. However, this is only valid in the case of a quantum emitter and thus verifies the quantum nature of the atom.

The absorption and emission spectra of molecules in the solid state (shown in Figure 1.4) exhibit features that depends on the interaction of molecules with the embedding matrix, as briefly discussed below.

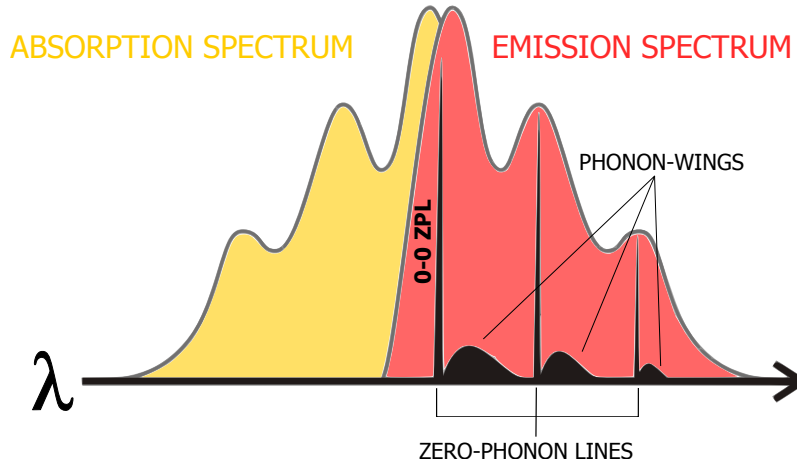


Figure 1.4: Absorption (yellow) and emission (red) spectra of single molecules embedded in solid matrix at room temperature. When the temperature is lowered, the spectra become narrower (black) and the zero-phonon lines and the phonon wings are resolved. Specifically, the zero-phonon line shape becomes Lorentzian, with a width determined by the excited-state lifetime τ . The phonon sideband shape shows instead a Poisson distribution, as it expresses a discrete number of events, i.e. electronic transitions involving phonons, during a period of time. At higher temperatures, or when the molecules strongly interact with the matrix, the phonon sideband approximates a Gaussian distribution, expressing a continuum of events, as the probability of multiphonon coupling becomes higher. The distribution of intensity between the zero-phonon line and the phonon sideband depends on temperature and it is characterized by the Debye-Waller factors.

Direct radiative transitions from the lowest vibrational level of an excited level to the lowest vibrational levels of S_0 correspond to the *zero-phonon lines* (ZPL) in the spectrum. Transitions between the singlet states and corresponding vibrational levels are determined by the so-called Franck-Condon factors. At temperature $T \neq 0$, or when the molecules strongly interact with the matrix, transitions from S_1 to S_0 involve coupling with matrix phonons and the momentum conservation results in *phonon wings* in the detected spectrum. Note that, when a transition involves phonons, the corresponding fluorescence photon is red-shifted (or *Stokes-shifted*) with respect to the photon needed to excite the molecule.

The existence of Stokes shift is critical for fluorescence imaging measurements, since the red-shifted fluorescence can be separated from the excitation laser by means of suitable optical filters. As will be discussed in Chapter 2, this feature can be exploited to detect the weak fluorescence signal emitted by individual excited molecules, enabling single molecule experiments.

1.4 Fluorescence near Interfaces

Following Purcell's analysis in 1946 [3], it is known that the environment in which an emitter is embedded modifies its radiative properties. This effect is expressed by Fermi's golden rule (equation 1.13), showing that the spontaneous emission rate can be modified by altering the density of photonic states available to the emitter. Since then, numerous experimental demonstrations of this effect have been published by coupling quantum emitters to: mirror surfaces [4], waveguides [12], photonic crystals [13], planar or spherical cavities [14, 15], etc. In fact, following advances in fabrication techniques, high Q-factor microcavities are now widely used to tune radiation rates, spectral response, and the emission direction of various emitter species.

More recently, the alteration in spontaneous emission features due to different geometries, as e.g. sharp metallic tips [16], structured microresonators [17], miniature photonic dots [18] and gold nanorings [19] has been demonstrated.

To understand the photophysics of a quantum emitter embedded in an inhomogeneous environment, is it useful to first consider a simple geometry: an emitter in the vicinity of a planar metallic surface as shown in figure 1.5(b). Such an interface can by itself cause the modification of optical processes and additionally, surface roughness and specially designed optical gratings have been shown to greatly influence the light-matter interaction over these surfaces [20].

An emitter located in free space above a metallic planar mirror can be semi-classically described as a damped harmonic oscillator that is driven by the reflected radiation field of the dipole moment associated with the oscillator [21]. In this case, the electric field at the dipole's position can be explained as a superposition of the primary dipole field

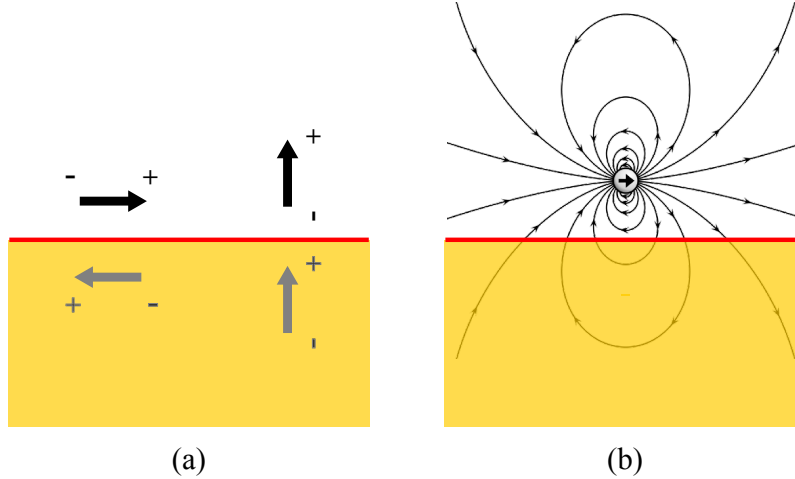


Figure 1.5: (a) Image dipoles produced by a reflecting surface for small surface-emitter distance. A dipole that is parallel to the surface tends to get cancelled out by its image while the perpendicular one gets enhanced. (b) Electric field of an emitter nearby an interface. This field would be modified by the presence of a substrate.

and the scattered field from the environment:

$$E(r_0) = E_0(r_0) + E_s(r_0) \quad (1.44)$$

where E_0 and E_s are the primary and scattered fields respectively. Thus the *change* in energy dissipation originates from the effect of this scattered field, affecting the dipole's decay rate and resonant frequency, when compared to the free space values [22]. For most emitters in the visible range (VIS), the frequency shift due to the reflected field is of the order of MHz and may be ignored. The spontaneous emission rate and the angular emission profile, instead, exhibit peculiar features that can be derived with the calculation of the reflected field at the dipole site.

Calculation of the reflected field is done by first expanding the dipole field in terms of plane waves, characterized by different wavevectors in the surface plane. The net reflected field is then calculated by using the summation over all k -vectors, with individual terms weighted by their respective *Fresnel reflection coefficients* (which depend on the complex permittivities of the two half-spaces).

Since the net field is dependent on the interference of the two fields, it is therefore important to consider the orientation of the dipole with respect to the interface. Figure 1.5(a) shows how for a horizontal dipole, the reflected dipole tends to cancel the source field, while that for a perpendicular dipole it is reinforced. Note that apart from radiative effects due the reflected field, the dipole oscillator can also couple to non-radiative channels at the interface due to absorption. However, these channels only

open up at reduced distances from the interface, comparable to the emission wavelength λ . This behaviour is explained briefly in the following discussion.

The field emitted by the dipole is characterized by wavevectors with magnitude k , in a medium with index of refraction n such that:

$$k = 2\pi n/\lambda \quad (1.45)$$

In loss-free media, this amplitude is real while in absorbing media it has a complex value. For each wavevector, the field can be written as a Fourier integral of plane waves represented by real wavevector components k_x and k_y (the interface lies in the xy plane). Considering the in-plane wavevector to be $k_{\parallel} = (k_x^2 + k_y^2)^{1/2}$, the out-of-plane wavevector k_z can be calculated by:

$$k_z = (k^2 - k_{\parallel}^2)^{1/2} \quad (1.46)$$

Depending on the magnitude of k_{\parallel} with respect to k , two situations arise:

If k is real and $k > k_{\parallel}$, then it results in a propagating plane wave with a real wavevector; if k is complex or $k < k_{\parallel}$, then waves are evanescent and decrease in amplitude in the z -direction. The range of available wavevectors is dependent on the distance from the interface and so is the value of k_z .

Figure 1.6 shows the results from one of the first experiments on the effect of planar interfaces on the spontaneous decay rate of dipolar systems. The spontaneous emission rate exhibits a damped oscillating behaviour with distance, due to the distance-dependence of both phase and amplitude of the reflected field. These oscillations die out at larger distances as the magnitude of the reflected field becomes too weak. Hence, depending on the distance between the emitter and the interface, three different *coupling mechanisms* take place, and the work undertaken in this thesis explores each of the coupling mechanisms as follows:

- **Coupling into radiation** - for distances larger than λ , i.e the *far-field*, the emitter primarily decays into radiative modes. Radiation is characterized by particular wavevectors given by the interference between the direct and the reflected fields, and the decay rate is only weakly modified. Therefore, in the far-field, the interface effect acts mainly in the angular distribution of the emitted radiation. This effect has been exploited to design thin-film optical antennas that can control the direction of emission from single molecules and have been described in **Chapter 4**.
- **Coupling into surface modes** - for intermediate distances comparable to λ , defined as the *near-field*, there is a larger range of available k -vectors. For $k < k_+$, the decay is still into photons that can propagate into the far-field. For $k > k_+$, they give rise to evanescent modes that couple non-radiatively to modes on the surface of the metal called surface plasmons (SPs), which can propagate along the

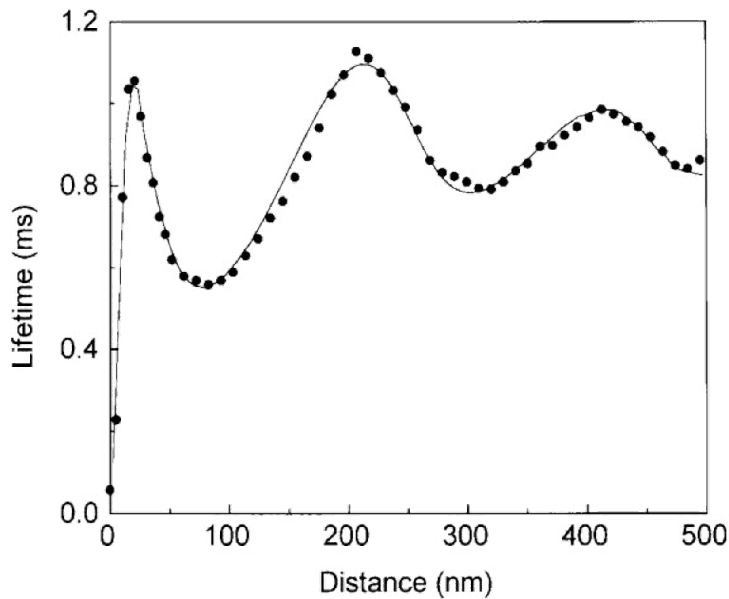


Figure 1.6: Distance dependence of the spontaneous emission lifetime of Eu^{3+} ions in the vicinity of an Ag mirror, whose dipole is free to rotate rapidly within the spontaneous emission lifetime and hence is an average over all orientations [4]. The solid curve is the theoretical fit proposed by [21]. Note how coupling to non-radiative modes in the metal becomes significant at small emitter-surface separations d and results in a strong quenching of the emitter fluorescence

interface as electron density oscillations. The branching ratio into each of these modes is again partly determined by the Fresnel reflection coefficients. For example, for higher reflectivities (say, by using a thicker metal film), radiative decay becomes the dominant decay channel due to a large reflected field, while for lower reflectivities (thinner metal film) decay into plasmons becomes more efficient. This distance regime is thus useful for both applications: radiation-engineering by planar optical antennas, and coupling to surface plasmons on metal films which will be described in **Chapter 5**.

- **Coupling into lossy waves** - for very small distances ($d < 20\text{nm}$), non-radiative processes other than SP-coupling dominate the decay rate, and these are determined by the intrinsic loss mechanisms in the metal: interband absorption, electron scattering losses and electron-hole excitations. It involves the transfer of energy to the substrate and a strong distance-dependent quenching of the fluorescence sets in. This energy transfer mechanism between an excited emitter and an induced dipole within the interface, as for example an electron-hole pair, is usually described with the standard Förster model [23] as a short-range dipole-dipole interaction. This mechanism has been explored for coupling to graphene excitons in **Chapter 6**.

It is worth mentioning that in the weak coupling regime between the dipole and field, this semi-classical approach is equivalent to the fully quantum description, and both lead to the same expression for the variation in the decay rate. In the end, the radiative decay rate in either case satisfies the relation:

$$\frac{\Gamma_r}{\Gamma_{r0}} = \frac{P_r}{P_{r0}} \quad (1.47)$$

where P_r and P_0 denote the power radiated in the photonic structure and vacuum respectively. This expression provides a simple means to calculate lifetime variations in arbitrary environments and in many experiments, the value $\frac{\Gamma_r}{\Gamma_{r0}}$ is informally dubbed as the Purcell factor.

2 Experimental setup

In this chapter, the setup configurations and their utility in different experiments has been described. While the work done in this thesis benefits from both single molecule and ensemble studies depending on the experiment, single molecule detection has been explained in this chapter to convey its significance as a method for probing interesting photophysics on the local level.

2.1 Single molecule detection

As seen earlier in chapter 1, molecules embedded in condensed phases feel a heterogeneous environment that correspondingly modifies their emission properties. Single molecule microscopy is thus a handy tool to probe the local environment in complex systems, removing the effects of ensemble-averaging. It can be used to explore the hidden heterogeneity of the system as well as to directly observe the dynamical state changes that occur after excitation, without the need for synchronisation between different molecules.

Since the first successful observation of single pentacene molecules in p-terphenyl in 1987 [24], single molecule spectroscopy has come a long way and subsequently been used in many experiments: observing quantum-limited linewidths of single molecules [25], temperature-dependent dephasing [26], optical saturation [27], effects of applied electric fields in crystals [28], etc.

For successful detection of single molecules, we need to ensure that: **only one molecule is in resonance in the volume probed by the laser**, and **signal-to-noise ratio (SNR) is high enough** to distinguish between molecule and background light. Today, the most common technique to detect single molecules is to measure their fluorescence through a microscope objective.

Provided that the excitation beam overfill the objective back-aperture, the minimum volume probed by a focused laser is limited by the *Abbe criterion*, which determines the resolution of detection as:

$$D = 0.5 \frac{\lambda_{\text{exc}}}{\text{NA}} \quad (2.1)$$

where D is the smallest resolvable distance between two objects, λ_{exc} is the excitation wavelength and NA is the numerical aperture of the microscope objective [29]. The concentration of the emitters is selected accordingly, so that only one molecule is present in the excitation volume (given by $V \simeq \pi(\frac{D}{2})^2 h$, where h corresponds to the minimum

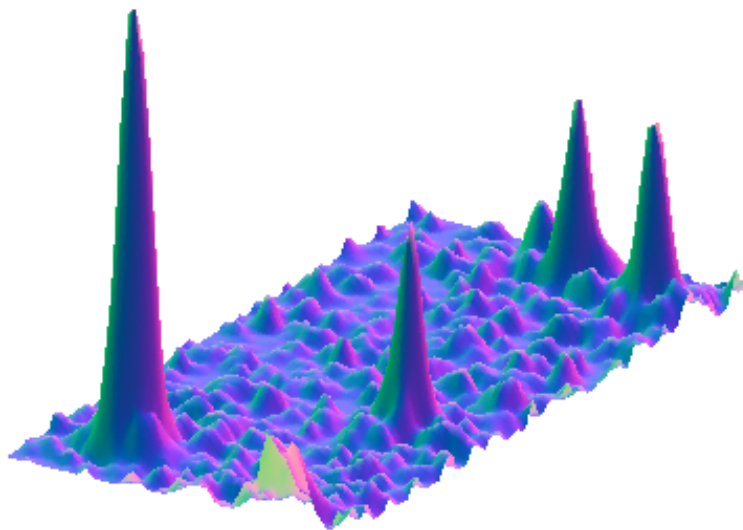


Figure 2.1: 3-D intensity map of a single molecule sample. Individual molecules stand out as bright points when the SNR is high.

value between the objective focal depth and the sample thickness). At low temperatures, the presence of inhomogeneous broadening can also be exploited to selectively excite only those molecules resonant with the laser, further reducing the probability of exciting more than one molecule within the excitation volume.

Achieving the required SNR relies on maximising the emitter fluorescence signal while minimising the background counts. To obtain as large a signal as possible, it is required that the emitter is photostable with a high quantum yield and that its absorption cross-section is maximised. Dibenzoterrylene-anthracene (DBT:Ac) condensed systems have been used in this thesis work, which are estimated with a three-level energy diagram as shown in Figure 1.3 and have a quantum yield of almost unity with high saturation count rates (refer chapter 3) resulting in a good SNR. Moreover, they are photostable for several hours under strong illumination [30], which makes it possible to overcome one of the main problems of single molecule studies and probe the same molecule for different measurements.

Several factors determine the classical absorption cross-section, i.e. the *effective photon-capture area*, for a single molecule in a solid matrix. Starting with the absorption cross-section for a two-level system in vacuum defined as [31]:

$$\sigma(\omega) = \frac{\lambda^2}{2\pi} \frac{\Gamma}{\Delta\omega} \quad (2.2)$$

where isotropic resonant radiation with wavelength λ is assumed and $\Delta\omega$ is the linewidth of the molecule. The above value is reduced by the Franck-Condon α_{FC} and the Debye-Waller α_{DW} factors, expressing the extent of vibrational relaxation and electron-phonon

coupling respectively. The former determines the shape of the intrinsic absorption spectrum while the latter is a measure for the intensity distribution between the zero-phonon line and the phonon wing, which is determined by the properties of the molecule-matrix system and decreases exponentially with temperature [32].

Another parameter is the angle θ between the transition dipole moment of the molecule and the electric field vector of the excitation light, that gives rise to an additional factor of $3 \cos^2(\theta)$. Taking into account all these factors, the absorption cross-section in equation 2.2, can be modified for a single molecule in a solid matrix as:

$$\sigma(\omega) = \alpha_{\text{FC}} \alpha_{\text{DW}} \frac{3\lambda^2}{2\pi} \frac{\Gamma}{\Delta\omega} \cos^2(\theta) . \quad (2.3)$$

At low temperatures, the absorption cross-section in equation 2.3 approaches the limit of $3\lambda^2/2\pi$ which is much larger (typically by 7 orders of magnitude) than the absorption cross-section of the same molecule at room temperature and about 10^4 times bigger than the physical size of the molecule itself [33].

Due to limited count rates in single molecule detection, reducing noise is fundamental to obtain an acceptable SNR. The dark-counts of the detector as well as the background signals all contribute to this factor. Using high efficiency detectors such as Avalanche Photo Diodes (APDs), Photo Multiplier Tubes (PMTs) and electron-multiplying CCDs that exhibit low dark-counts reduces the Poisson noise. The background to the fluorescence signal refers to photons arriving at the detector from any source other than the molecule in question. This includes the excitation laser and other molecules in the vicinity.

As previously discussed, excitation in a molecule is typically followed by a fast non-radiative relaxation process to the lowest vibrational level of the electronic excited state. The optical decay to the ground state (or to its vibrational sublevels) follows, with the emission of a fluorescent photon at longer wavelengths with respect to the excitation light (Stokes shift). By means of suitable optical filters (for example a *long pass filter*) placed in front of the detectors, the Stokes-shifted fluorescence can be measured while suppressing the excitation light. Further, it is clear that any excitation power over and above the molecular saturation would only raise the background levels while fluorescence counts would remain constant.

In an *epifluorescence microscope*, excitation of the fluorophore and detection of the fluorescence are done through the same light path, and it's possible to separate fluorescence by spectral filtering with a *dichroic mirror* which splits an incoming light into two beams of different wavelengths. The epifluorescence configuration is the basis for more advanced microscope designs, such as the *confocal microscope* and *wide-field* configuration, which are discussed in the next section.

2.1.1 Confocal microscope

Even though the use of a microscope objective already reduces the probe volume, all the molecules within the excited volume contribute to the fluorescence signal, as shown in the inset in Figure 2.2.

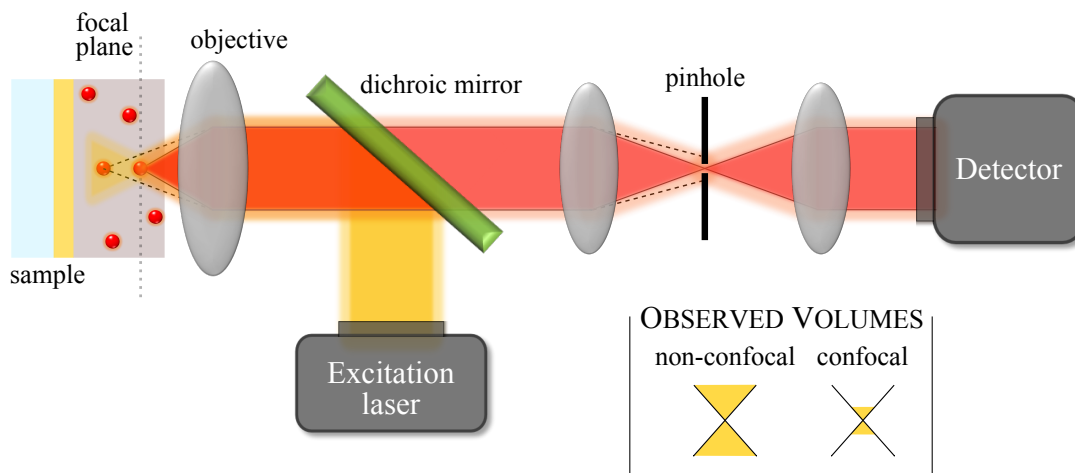


Figure 2.2: The confocal principle: the pinhole is placed at a focal point in the detection light path. By ray-tracing the light path, one can see that light from above or below the focal plane is not focused onto the pinhole and does not reach the detector.

An appropriately-sized pinhole in the detection line can further decrease the volume of observation, isolating light coming from the focal plane. Referring to Figure 2.2, light not originating from the focal area will not be able to pass through the detection pinhole and hence cannot reach the detector. Beams originating from points displaced along the optical axis will not be focused in the detection plane and are therefore strongly attenuated. This detection method strongly reduces the background signal and optimizes single molecule fluorescence detection [34]. When only a point-like volume of the sample is imaged onto the photodetector, the microscope is termed confocal.

A confocal microscope is a detection system that can fulfill both of the requirements for efficient single molecule detection: low probe volume and high SNR. There are two main ways in which a sample area can be scanned point-by-point (raster scanning) with a confocal microscope: by either physically moving the sample or by moving the excitation spot by tilting mirrors. The experimental setup used in this work is an assembled inverted epifluorescence scanning confocal microscope, whose main components are depicted in Figure 2.3.

The sample-holder is mounted on a piezoelectric scanning stage (Physik Instrumente NanoCube P-611.3), with a linear positioning repeatability of 100nm, placed onto a micrometric manual 3D-stage. Measurements were done with two objectives: an oil-immersion objective (Zeiss Plan Aplanachromat, 100X, NA= 1.4) and an air objective (Mitutoyo M Plan Aplanachromat 378-806-3 100X). Several laser sources can be coupled

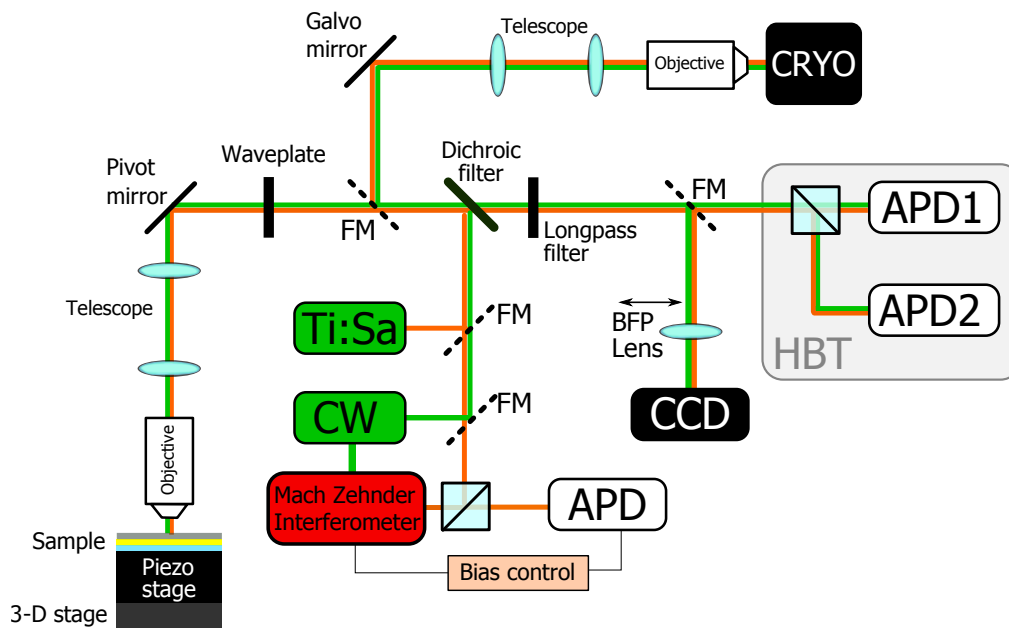


Figure 2.3: Scheme of the combined setup (explanation in text).

into the microscope by means of flippable mirrors (FM) and, depending on the experiment, are used for fluorescence imaging and spectroscopy and to measure the emitter saturation curve and autocorrelation function. Among these, two pulsed sources have been employed for lifetime measurements, namely an 80 MHz Ti:sapphire pulsed laser and a 767 nm Continuous-Wave laser light *chopped* into pulses by a Mach-Zehnder (MZ) interferometric modulator that provides 7 ns pulses with repetition rate of 39 MHz. A MZ interferometer works on the principle of dividing an input beam into two through a beamsplitter and then introducing a phase delay on only one of the optical paths, which results in interference patterns upon recombination at the other end. To get a pulsed source, a MZ modulator is inserted in the excitation path of the continuous wave laser such that destructive interference (with an extinction ratio of about 20 dB) at the output effectively results in pulsed light. Since lifetime measurements are not affected by the excitation method and apparatus efficiency, a MZ interferometer can provide a cost-effective way to obtain a pulsed source compared to commercially available Ti:sa pulsed lasers.

The excitation laser beam should overfill the back aperture of the objective lens and impinge as a collimated Gaussian beam in order to exploit the full numerical aperture of the system. Each laser light is spatially filtered by coupling it to a single-mode optical fiber, with a core diameter of 4 μm , allowing for efficient confocal excitation. The stability of the laser sources is monitored by directing a small portion (8%) of the beam through a pellicle beamsplitter into a scanning Fabry-Perot cavity (FP) (FSR = 5 GHz). For optimal excitation, the polarization of the excitation beam is aligned with the transition dipole moment of the target molecule by means of a half-waveplate.

A converging achromatic (WF) lens can be inserted in the excitation path (while simultaneously removing the detection pinhole) to switch from confocal to wide-field excitation. As the laser beam is focused onto the objective back-aperture, it illuminates a wider area ($\simeq 50 \times 50 \mu\text{m}^2$) than in the confocal excitation mode. The same can also be used with a white light (WL) source instead of a laser to obtain a standard microscope image.

The emitted red-shifted fluorescence signal is collected by the objective and travels back in the excitation path, where it is separated from the laser signal by the dichroic mirror (DM) and then enters the detection line. To further filter the laser light and increase SNR, a long pass (LP) filter with optical density > 6 is inserted after DM.

A (flippable) spatial filter (SP), a $50 \mu\text{m}$ pinhole is inserted at the focal point of a 1:1-telescopic system ($f = 100$) which is placed after the LP, thus allowing to detect the fluorescence signal in confocal mode.

To detect the weak fluorescence signal, highly efficient detectors with reduced electronic background are used. Depending on the measurement to be performed and thus on the specific configuration of the fluorescence microscope, single-element (pixel) APDs (Picoquant Tau-Spad) or a multi-element electron multiplying CCD (EMCCD) camera (Andor iXon3) can be used. A Czerny-Turner spectrometer with 0.1 nm resolution that is directly connected to the EMCCD camera is utilised for spectrometric measurements. The APDs can be used to measure the saturation curve, lifetimes or the intensity autocorrelation function in an *Hanbury-Brown-Twiss (HBT) configuration*, which is described in the next section. The detection elements are also coupled by a separate optical path to the cryostation (Montana Instruments), which is a closed-cycle cryostat that uses liquid helium as the coolant and the cooling of the sample is done by attaching them to a metallic cold-finger platform inside the vacuum chamber which is in thermal contact with the helium vapour chamber.

In wide-field (WF) configuration, the EMCCD camera is used for one-step acquisition of a sample image. In Figure 2.4, examples of white light, wide-field and scanned-confocal images are shown.

A PicoHarp300 TCSPC (Time Correlated Single Photon Counting) system is used to study the dynamics of the sample. The principle of TCSPC is based on the detection of single photons and the measurement of their arrival times with respect to a reference signal. For excited-state lifetime measurements, the emitter is excited with a pulsed laser which is used as the reference signal. As discussed earlier, the lifetime of a quantum emitter is a statistical average and the intensity decay given in equation 1.32 represents the time distribution of the emitted photons. A high repetition rate laser source is employed in order to accumulate a sufficient number of photon events and hence collect significant statistics. The fall-time of the excitation pulse should be short enough not to affect the oncoming fluorescence signal. However, this fall-time is limited by the optical elements in the beam path and thus contributes towards the final time

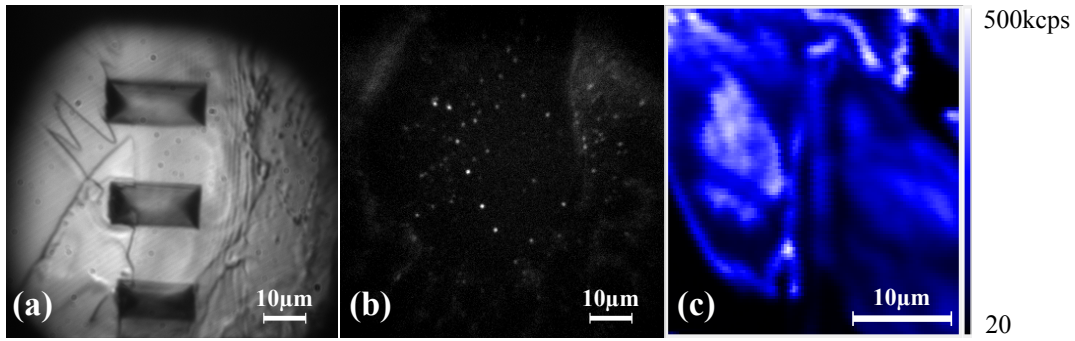


Figure 2.4: (a) White light image of plasmonic wedge waveguides (b) Wide-field fluorescence image of a single molecule sample and (c) Confocal fluorescence scan image of a crystalline film embedded with a high concentration of dye molecules spin coated over wedge structures. The confocal scan was taken with a resolution of $0.3 \mu\text{m}$.

response function of the system. A post-analysis for deconvolution of this signal from the output is helpful to go beyond this instrumental value. When the trigger from the pulsed laser is used as a start signal and the fluorescence intensity detected by a single APD as a stop signal, the TCSPC system allows to measure the molecule decay trace, from which the molecule excited-state lifetime can be extracted (as shown in Chapter 6).

With the same operational principle, a TCSPC card coupled to the HBT setup allows to perform intensity autocorrelation experiments and to build up the *antibunching curve*, which can be obtained when the start and stop signals are both derived from the molecule fluorescence signal divided equally over the two APDs.

2.2 Hanbury-Brown and Twiss Setup

Consider an ideal photon-counting experiment in which the quantum efficiency of the detectors is high enough, so that the intrinsic photon statistics of the light beam are conserved in spite of the statistical nature of the photodetection process. Although the average number of photons detected can have a well defined value, the photon number on short timescales fluctuates due to the discrete nature of light. This is the *photon shot noise* and just as with other forms of shot noise, the fluctuations in the photocurrent can be expressed in term of the average intensity, i.e. an average number of n photons, \bar{n} .

The photon statistics describing these fluctuations lend to a classification of light that highlights the original features of a single-photon source with respect to standard light sources [31].

Additionally, the statistical character of the intensity fluctuations of an electromagnetic field can be also described by the **second order correlation function** $g_2(\tau)$,

which is the joint probability of detecting two photons in a time interval τ [35]. The $g_2(\tau)$ function is classically written in terms of the intensities I of the detected fields as:

$$g_2(\tau) = \frac{\langle I(t+\tau)I(t) \rangle}{\langle I(t) \rangle^2} \quad (2.4)$$

where the average is taken over a temporally-stable state of light [8].

Setting $\tau = 0$, with some calculations the second order correlation function can be written [36], in terms of the number of detected photons, as:

$$g_2(0) = 1 + \frac{(\Delta n)^2 - \bar{n}}{\bar{n}^2} \quad (2.5)$$

This expression clearly underlines the connection between $g_2(\tau)$ and photon statistics, and can be used to make some important inferences that establish the quantum nature of light.

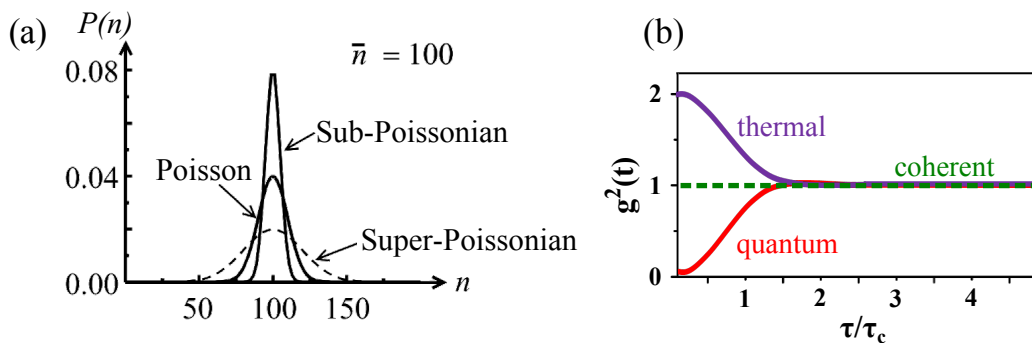


Figure 2.5: (a) Comparison of the photon number distributions of super-Poissonian and sub-Poissonian light to that of a Poissonian distribution with the same mean photon number \bar{n} . (b) Second-order correlation functions $g_2(\tau)$ for coherent, thermal and quantum light.

According to the standard deviation Δn of the photon number distributions $P(n)$, and hence g_2 , light can be classified into three categories:

coherent light An ideal single-mode laser is a reasonably good approximation of a perfectly coherent light beam characterised by a constant phase and intensity. It can be shown that perfectly coherent light has Poissonian photon statistics: $\Delta n = \sqrt{\bar{n}}$.

Substituting in equation 2.5, we get $g_2(0) = 1$. Although average intensities remain constant, photons arrive at random time intervals. Thus coherent light is also referred to as **random light**.

thermal or chaotic light Thermal light from a black body source is characterized by partial coherence and intensity fluctuations, and is therefore noisier than perfectly coherent light in both the classical sense - it has larger intensity variations - and also in the quantum sense - it has larger photon number fluctuations. In fact, it

According to	statistics	$g_2(0)$
coherent	$\Delta n = \sqrt{\bar{n}}$	$g_2(0) = 1$
thermal	$\Delta n > \sqrt{\bar{n}}$	$g_2(0) > 1$
quantum	$\Delta n < \sqrt{\bar{n}}$	$g_2(0) < 1$

Table 2.1: Classification of light

can be shown that incoherent light is described by the super-Poissonian statistics: $\Delta n > \sqrt{\bar{n}}$.

Similarly, $g_2(0) > 1$ which means that if we detect a photon at time $t = 0$, there is a higher probability of detecting another photon at short times than at long times. In this case the photon stream is characterized by photons emitted in bunches, thereby the name **bunched light**.

quantum light Certain individual emitting species (i.e. a single atom, molecule, quantum dot, or colour centre), when excited with a laser, emit one photon and it will take a time approximately equal to the radiative lifetime of the transition before the next photon can be emitted. Thus photons emitted by an individual quantum emitter come out with regular gaps between them, rather than with a random spacing. This light is described by the sub-Poissonian statistics: $\Delta n < \sqrt{\bar{n}}$. This means that sub-Poissonian light has an even narrower distribution than the Poissonian (ideal) case, and thus has no classical counterpart.

$g_2(0) < 1$ signifies that after the detection of one photon, the probability of detecting another photon is small for small time intervals and increases with τ . Sub-Poissonian light is also referred to as **antibunched light**.

Table 2.1 summarises the classification made above and figure 2.5 illustrates the difference between coherent, thermal and quantum light. In figure 2.5(b) the $g_2(\tau)$ function is plotted as a function of the time delay normalized to the coherence time τ/τ_c .

For perfectly antibunched light, the correlation function vanishes for zero time delay and this is incompatible with the classical equation 2.4, since any classical stationary random function of time must satisfy the Schwartz inequality $\langle I(t')I(t) \rangle \leq \langle I(t)^2 \rangle$. Therefore, photon antibunching and the related (but not equivalent [37]) sub-Poissonian photon statistics are evidences of the quantum nature of light. However, these effects are very sensitive to optical losses and inefficient detection and therefore have been observed relatively recently, following the development of highly efficient detectors. The straightforward method to measure the second-order coherence function would be to simply note the times of the detection events at the photodetector, and to explicitly compute the correlation function. However, this approach prevents the measurement of timescales smaller than the photodetectors dead time, that is typically around 50 ns. To overcome this problem, the Hanbury Brown-Twiss (HBT) [38] arrangement is chosen.

With this setup, Kimble et al. in 1977 [39] gave the first successful demonstration of photon antibunching.

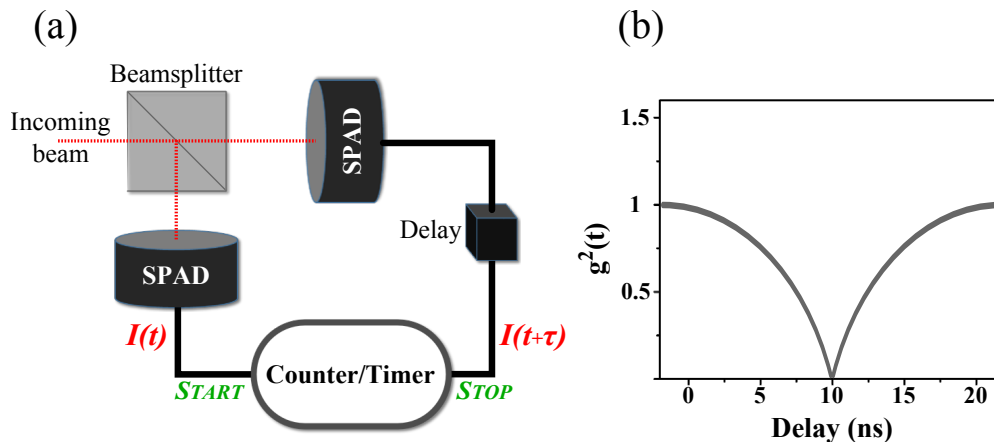


Figure 2.6: (a) Schematic diagram of a HBT. Coincidences between counts on the two detectors give access to the $g_2(\tau)$ correlation function. (b) At room temperature and thus for very short coherence lifetime T_2 , $g_2(\tau)$ function presents a dip for time delay $\tau = 10\text{ns}$ (offset from zero by a manufactured delay) and tends exponentially to its long-time value $g_2(\tau \rightarrow \infty) = 1$

The **HBT setup** consists of two highly efficient photodetectors monitoring the outputs of a 50:50 beamsplitter, as shown in Figure 2.6(a). At the beamsplitter, the incoming photon stream is equally split i.e. giving equal detection probabilities at each detector. Photons impinge on the detectors and the resulting output pulses are fed into to the start and stop inputs of an electronic counter/timer, typically a TCSCP module (discussed in the previous section). The counter/timer records the time that elapses between the pulses from D1 and D2, while simultaneously counting the number of pulses at each input. The results of the experiment are presented as a histogram that displays the number of events that are registered at each value of the time between the start and stop pulses. The stop pulses can be delayed by a few ns (for example by putting an extra length of electrical cable) to place the coincidence point in the centre of the recorded time interval, as shown in Figure 2.6(b), a 10 ns delay between start and stop signal.

When the incoming light originates from millions of atoms as in a discharge lamp, there is a high probability that the two detectors click simultaneously and photon bunches are observed. In the case of a single quantum emitter instead, the incoming stream is mainly one photon at a time and thus it is more probable that only one detector clicks. The distribution of coincidences for short time scales obtained as normalized by the average photon count rate gives the normalized autocorrelation:

$$g_2(\tau) = 1 - e^{(\gamma_{\text{abs}} + \gamma_{\text{spont}})\tau} \quad (2.6)$$

illustrated in Figure 2.6 (b). For $\tau = 0$ the second order correlation function is zero which means that the probability for the detection of two photons at the same time vanishes. For long time delay τ , the $g_2(t)$ function reaches one, indicating that photon arrival times are uncorrelated.

2.3 Experimental upgrades of the setup

2.3.1 Back-focal plane imaging

In the confocal setup described earlier, it's also possible to measure the angles in which radiation is emitted from a point-like source at the focus of the objective. This can be achieved by measuring intensities in the Fourier plane (also called the back-focal plane) of the objective lens, hence the name back-focal plane (BFP) imaging. The emission pattern is usually a clear indication of the orientation of the emission dipole [40]. It can also give additional insight about the observed emitter such as identification of different radiation channels, changes in the emission characteristics due to coupling effects [41] or material properties [42]. The significance of angular emission pattern imaging will be described in detail later in Chapter 4.

Placing an emitter in a multilayer structure changes its emission pattern compared to that in a homogeneous medium. Consider now that the emitter lies at the interface of a bi-layer configuration, with the two layers having refractive indices n_1 and n_2 respectively with $n_1 < n_2$. The fractions of radiation emitted in different angular regions can be depicted as in Figure 2.7(a). The total radiated power P can be divided

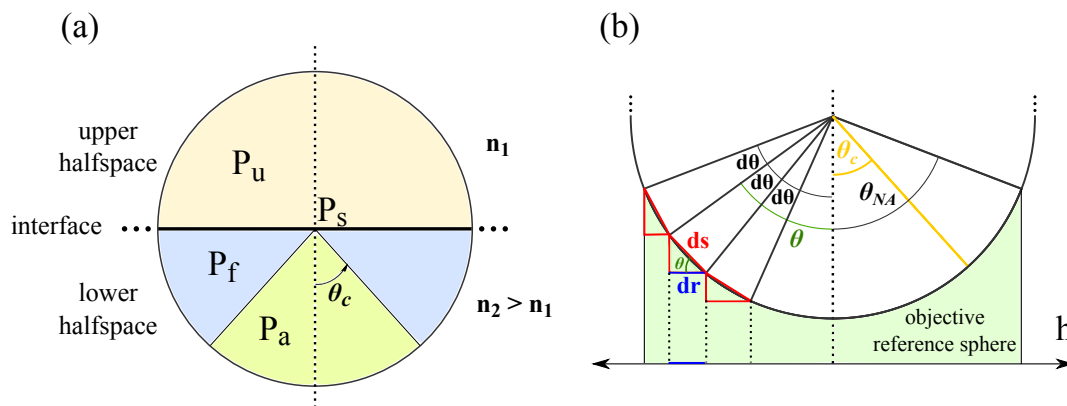


Figure 2.7: (a) Schematic diagram of the power distribution in the upper and lower half spaces given by equation 2.7. (b) Schematic of the projection of angular emission by an imaging lens onto the BFP. The emitter is situated in the center of the emission sphere. Adapted from [43].

into emission into the upper half-space P_u , the forbidden zone of the lower half-space P_f for angles larger than the critical angle θ_c , the allowed zone P_a for angles smaller

than θ_c , and power dissipated into the surface P_s [44]:

$$P = P_u + P_f + P_a + P_s \quad (2.7)$$

This geometry represents a typical microscopy situation where an emitter is placed on a glass slide and in the focus of a high NA objective. The objective collects the light emitted in the lower half-medium of the glass slide, in the allowed region and parts of light emitted in the forbidden zone. To calculate the intensities in the BFP of the objective lens as a function of emission angle θ , it is useful to consider the Weyl representation [45] which uses the decomposition of the spherical wave started by the emitter into planar and evanescent waves, when it hits the reference sphere of an aplanatic high-NA objective lens. With this approximation, the intensity distribution in the Fourier plane of an objective lens can in general be expressed by the fields generated by the emitter E_{emit} :

$$I_{\text{BFP}} \propto \frac{1}{\cos \theta} |E_{\text{emit}}|^2 \quad (2.8)$$

This includes the factor $\frac{1}{\cos \theta}$ to correct for the projection onto a flat BFP as illustrated in Figure 2.7(b). The amount of power radiating into equally sized angular sections $d\theta$ is collected through ds , and then projected onto dr in the BFP.

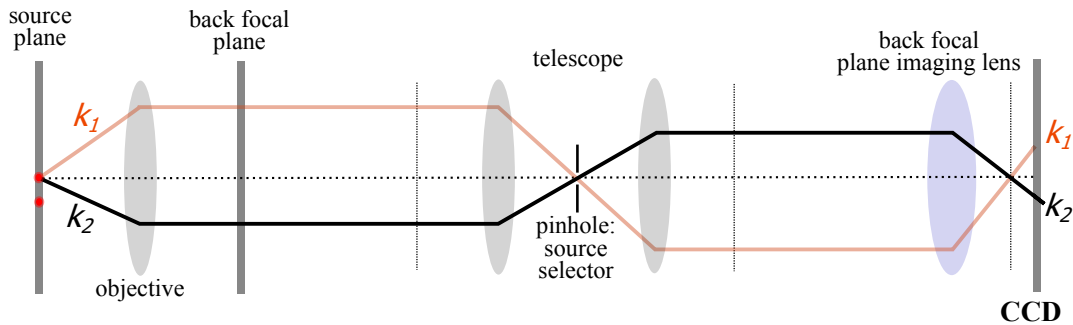


Figure 2.8: Schematic of the BFP imaging setup. Light rays with different wavevectors k map different points on the CCD camera, where distances from the optical axis depend on the angle of emission associated with that wavevector.

Experimentally, imaging of the Fourier plane is done by placing a suitable lens, also called Bertrand lens, at the exit port of a regular microscope. This lens is focused such that it directly maps the intensity distribution in the BFP onto the CCD camera as shown in Figure 2.8. The magnification of this lens is chosen on the basis of a compromise between angular resolution and SNR, specially relevant for single molecule observation. The figure also depicts the spatial filter (pinhole $50 \mu\text{m}$) used for confocal detection. Each emission angle α corresponds to an axial distance $h(\alpha)$ in the Fourier

plane, then according to the sine condition [46],

$$h(\alpha)(\text{mm}) = n_{\text{obj}} f \sin \alpha \quad (2.9)$$

where f and n_{obj} are the focal length and refractive index of the objective respectively. When this plane is mapped onto the camera, the radial distance from the optical axis in pixels h_{px} can be converted back into angles by the relation:

$$\alpha(h_{\text{px}}) = \arcsin \left(\frac{h_{\text{px}}/a}{n_{\text{obj}} f} \right) \frac{180}{\pi} \quad (2.10)$$

where a is the calibration factor in pixels/mm determined by the magnification of the optical setup.

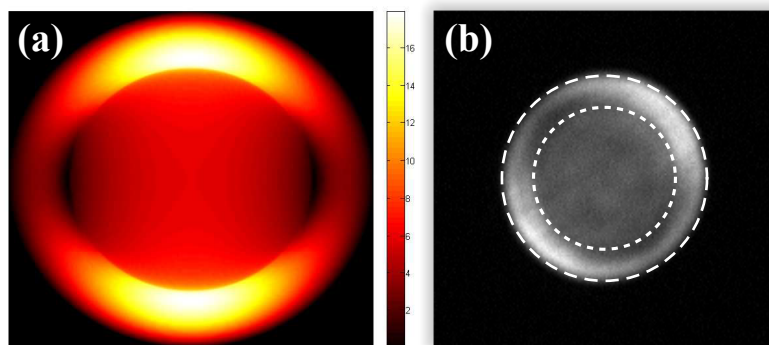


Figure 2.9: (a) Simulated and (b) Observed angular emission pattern of a horizontal dipole. The inner circle corresponds to the critical angle and the outer circle corresponds to maximum angle collected by the objective.

Figure 2.9(a) shows a simulation of the emission pattern of a dipole lying parallel to the sample plane. Note that the final intensities are also modulated by the system response due to limited NA of the objective as shown in Figure 2.9(b). Calculations show that for all dipole orientations the majority of light is emitted into the forbidden zone above the critical angle θ_c , and hence it's required to use a high NA objective for increased detection efficiency. This issue is the main motivation towards the project discussed in Chapter 4, which enables the observation of dipolar emission patterns using low NA optics by using a simple sample configuration.

2.3.2 Kretschmann configuration

Chapter 5 deals with the study of light-matter interaction that happens at metal interfaces in a certain distance regime as described in section 1.4, and leads to the creation of hybrid light-electron complexes called surface plasmon polaritons (SPPs). A detailed description can be found in section 5.1.1 for properties of SPPs. There are several

methods which can be used to excite SPPs on planar metal films. Here in this section, the workings of the setup based on one of those methods has been described.

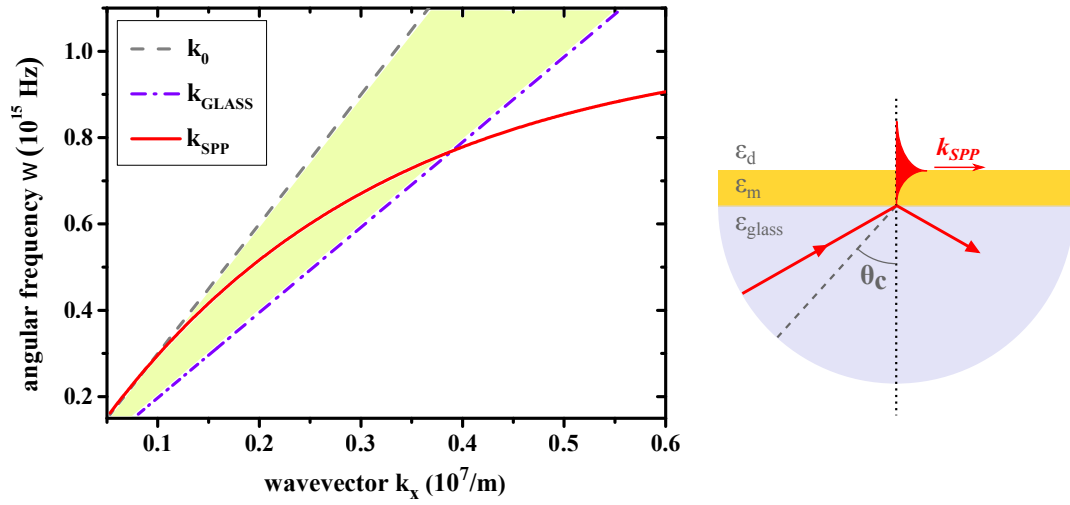


Figure 2.10: Dispersion relation for an SPP mode (left): the *light line* with momentum k_0 approaches the curve asymptotically but never intersects it. Kretschmann configuration (right): light passing through a medium with a higher refractive index than air is able to excite surface plasmons since the dispersion relation now intersects the SPP curve and the momentum-matching condition is fulfilled. The shaded area represents the range of possible momenta from the maximum at $k_{\text{glass}}(\theta = 90^\circ)$ to the minimum at the light line ($\theta = \theta_c$).

Figure 2.10(a) shows the dispersion relation i.e. the relation between in-plane momentum and energy for an SPP mode. An important feature of this mode is that for a given energy $\hbar\omega$, the in-plane wavevector k_x is always greater than the wavevector of light in free space. Excitation of an SPP is only possible if the wavevector of the excitation beam is brought to match the wavevector required to generate a surface plasmon. The Kretschmann configuration takes advantage of the fact that light propagating in a dielectric medium has a momentum proportional to the refractive index of that medium. Thus, if the excitation light comes through a medium of higher refractive index compared to the medium that forms the metal-dielectric interface, it's possible to match the SPP momentum and launch a surface plasmon on the upper interface (see figure 2.10(b)).

This method was developed by E. Kretschmann in 1971 by depositing a thin metal film on top of a glass prism [47] and introducing light from the bottom half at a certain angle greater than θ_c to enable the evanescent field arising from total internal reflection to excite SPPs over the metal-air interface. The excitation of an SPP would show up as a minimum in the totally reflected light, hence the name Attenuated Total Reflection (ATR) method. By changing the angle of incidence, it's possible to tune the resonance

condition for SPP excitation according to the following relation:

$$k_{\text{SPP}} = k_{\text{glass}} = \frac{\omega}{c} n_{\text{glass}} \sin \theta \quad (2.11)$$

The occurrence of a dip in the ATR spectra can be interpreted in two ways: first, as the destructive interference between light reflected directly from the interface and light emitted due to radiation damping (decay of SPP mode into propagating radiation in the glass), or second, as the *missing* light which gets converted into the surface bound SPP mode and hence is inaccessible to the detector.

Figure 2.11 shows a picture of the setup used in this thesis to realise the Kretschmann configuration. The excitation arm is coupled to a broadband source (Thorlabs OSL1) and the detection arm is coupled to a spectrometer (Ocean Optics USB2000+) through optical fibers. Both arms can be rotated around the central vertical axis which coincides with the center of the prism. The excitation whitelight enters the path through a 100 μm

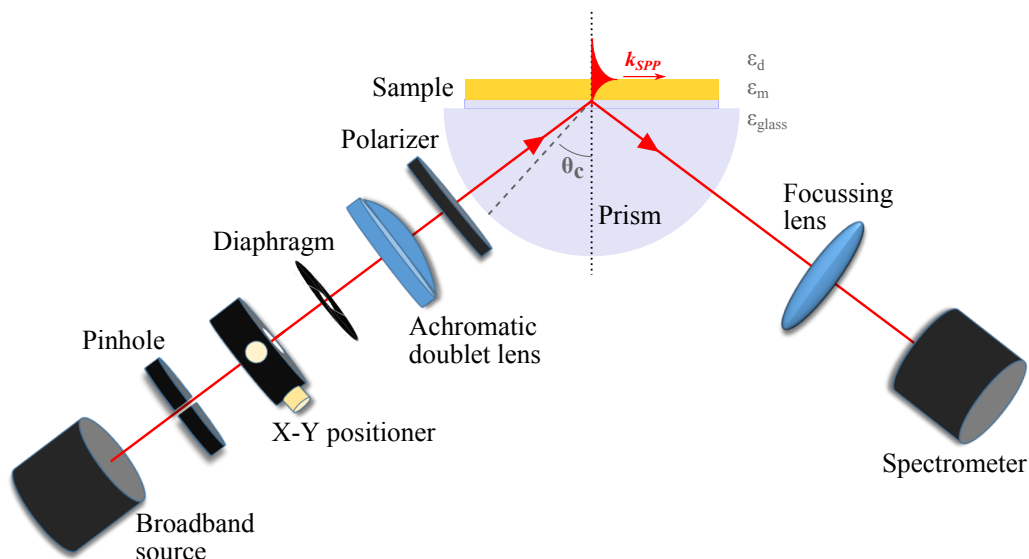


Figure 2.11: Schematic of the Kretschmann setup in the lab.

pinhole which acts as a fixed point source, which is useful as it enables coupling of different light sources and optical fibers without disturbing the rest of the setup. After being centered by an X-Y aligner, it passes through a diaphragm. The diaphragm is used to set the amount of k-vectors impinging on the sample, which influences the resolution in the dispersion curve. The filtered light is then focused into a smaller spot by an achromatic doublet lens (Thorlabs AC-254), which is used to reduce the chromatic dispersion of the wide range of optical frequencies present in the excitation white light. The polariser at the end is used to select the p-polarised component of the impinging beam, since it is known that only this polarization is responsible for excitation of SPPs on a metal surface [48]. This light after being reflected at the prism face, is sent to the spectrometer through an optical fiber. A simple modification is

made: the gold layer resides on a glass coverslip and not directly on the prism face. An index matching oil is used to temporarily *stick* the sample to the prism, all refractive indices of prism, oil and coverslip being the same (RI=1.52). This enables coupling of different samples with the setup without introducing additional interfaces. The total length of the excitation arm is 135 mm, and the lens is situated at 35 mm from the sample interface. This gives a magnification of about 0.3, which starting from a 100 μm source at the pinhole, gives a spot size of 30 μm on the sample.

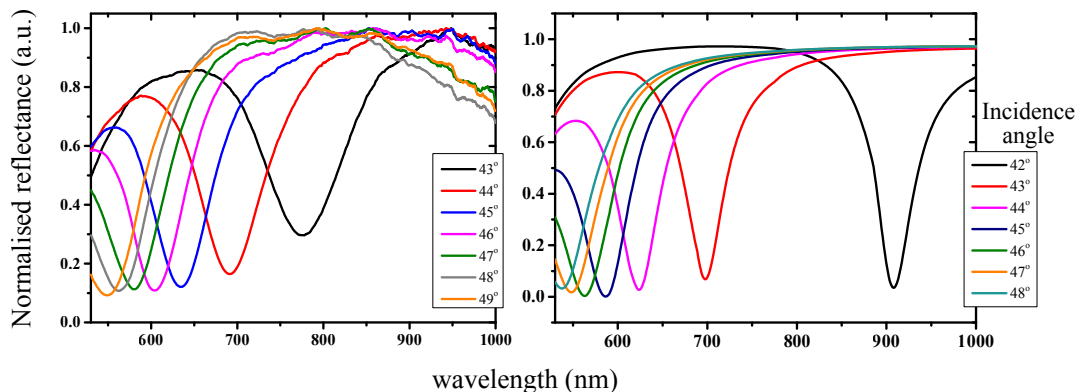


Figure 2.12: (a) Observed ATR curves (b) Simulated ATR curves

Figure 2.12(a) shows a typical collection of reflection curves obtained by changing the incidence angle for a gold/air interface. The widening of the curves compared to simulations is attributed to the limited resolution for the incidence angle, which is determined by the diaphragm aperture. For 1mm aperture diameter, the convergence angle can be found out by $\tan \theta = (r_{\text{aperture}} - r_{\text{spot}})/q = (500 - 15)\mu\text{m}/35\text{ mm}$ that gives $\theta = 0.77^\circ$.

2.3.3 Raman spectroscopy of Graphene

In Chapter 6, the coupling of single molecules to a graphene monolayer has been discussed. We here describe the setup implemented for the purpose of identifying the quality of the graphene layer done by Raman spectroscopy. Raman spectroscopy is a commonly used technique to identify vibrational modes in matter. Raman scattering is the inelastic scattering of a coherent monochromatic laser caused by rotational or vibrational transitions in that chemical species [49]. The laser light interacts with molecular vibrations, phonons and other excitations in the system that results in scattered laser photons having a higher or lower energy than the incoming photons, the difference in energy corresponding to the vibrational modes of the system. This vibrational information is unique to a molecular structure and hence a chemical fingerprint by which it can be identified [50].

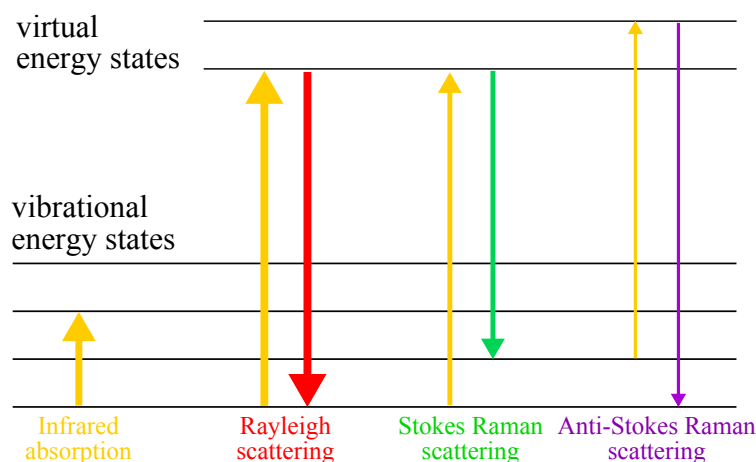


Figure 2.13: Energy level diagram showing different types of scattering processes, where the width of the arrows indicates the strength of the scattering process. Most of the light is elastically (Rayleigh) scattered, and rest of the signal correlates to inelastic scattering processes. Note that the energy spacing between the virtual levels is equal to the corresponding vibrational energies, and thus the Stokes and Anti-Stokes lines form a symmetric pattern around the central Rayleigh frequency.

Experimentally, a laser beam is directed at the sample and the reflected/transmitted light is spectrally analysed. The laser excites the molecule to a virtual energy state, i.e. a vacuum state that does not match any of the energy levels of the molecule. Typically light can be scattered in two ways: elastic (Rayleigh) or inelastic (Raman) scattering, each having probabilities of about 100000:1. Thus Raman scattering is an extremely weak effect and hence it is imperative that Rayleigh scattering is filtered out with high performance filters which let pass only a narrow wavelength range (*notch*-filters). If inelastically scattered, the emergent photon can have a lower or higher frequency with respect to the excitation frequency, both offset by an amount equal to the vibrational frequency (see figure 2.13). A lower frequency corresponds to Stokes' shift and a higher frequency to the Anti-Stokes' shift¹.

Graphene is an entirely two-dimensional organic material made up of carbon atoms. Like all organic molecules it has a typical Raman signature: a so-called G-band appearing at 1582 cm^{-1} , characteristic of graphite, and the 2D-band at about 2678 cm^{-1} , as shown in Figure 2.14. The 2D-band lineshape can be used to determine the number of graphene layers. In particular, for a graphene monolayer at room temperature, the 2D-band exhibits a single Lorentzian lineshape with an intensity about two times higher than the G-band [51].

It can be shown that Raman signal intensities scale with $1/\lambda^4$ [52], and thus reported graphene Raman spectra acquired using green laser lines are more intense than the ones

¹Since molecules tend to be in the ground state in equilibrium conditions, a Stokes' shift is much more probable than an Anti-Stokes' shift.

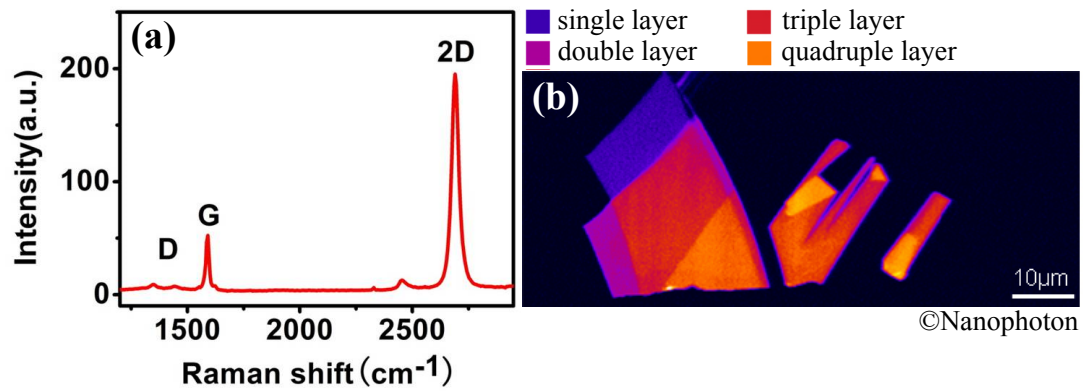


Figure 2.14: (a) Raman spectrum of graphene, showing the first order Raman G-band and the very strong 2D band, which has an intensity about two times higher than the G-band and a single Lorentzian lineshape for monolayer graphene. (b) The number of layers can be distinguished by the 2D/G-bands intensity ratio and inspecting the lineshape of the 2D-band.

obtained with longer excitation wavelengths [53]. For this reason, a green CW laser with central emission wavelength around 532 nm has been used in this work. The details of the measurements have been discussed later in Chapter 6.

3 Emitter System

This chapter elaborates on the characterization of a particular single photon emitter system that has been used in this work, at both room and low temperatures. Here we first describe the spectroscopic properties of the fluorescent dye molecules followed by fabrication techniques for obtaining the dye-doped crystals that can be integrated with different photonic devices. Finally, characterization of single molecules has been presented thereafter.

Dibenzoterrylene molecules in anthracene

In this work, the emitter system used for coupling to different photonic structures is Dibenzoterrylene (DBT) dye molecules embedded as *impurities* in a solid state matrix of Anthracene (Ac). This dye-host pair has been put together relatively recently and has been described as a promising system to study conduction at low temperatures [54] and as a stable single photon source in the near-infrared (NIR) at room and at low temperatures [30, 55].

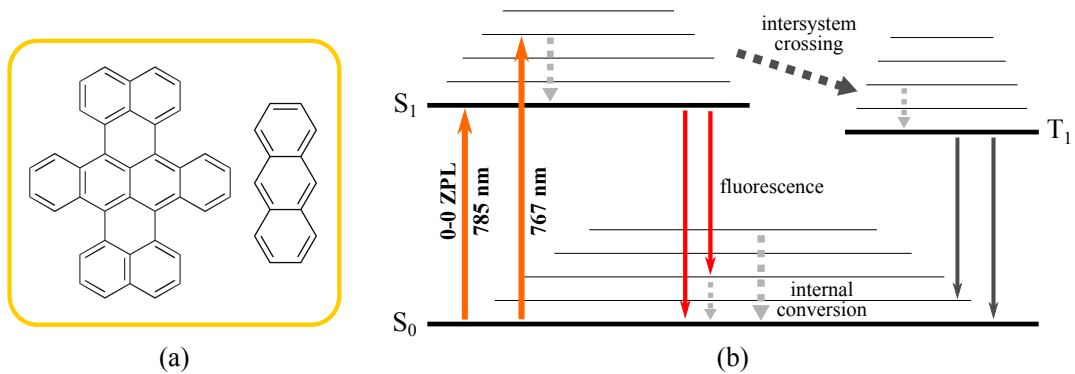


Figure 3.1: (a) Chemical structures of DBT and Ac (b) Jablonsky diagram for a single DBT molecule embedded in anthracene. Radiative transitions are represented by solid arrows, while dashed arrows indicate non-radiative transitions, via phonons (internal conversion) or via intersystem crossing.

Figure 3.1(a) shows the chemical structure of DBT and anthracene. Both DBT and anthracene are solid polycyclic aromatic hydrocarbons (PAHs) composed of benzene rings, and thus have compatible structures to ensure an efficient packing of the host molecule (Ac) around the the bigger guest molecule (DBT), which has several advantages. Besides protecting DBT from external agents and preventing *photobleaching*,

this solid matrix makes the dye molecule sit rigidly with the dipole moment aligned parallel to one of the crystal faces (and hence the sample surface) and has been verified by back-focal plane imaging described in section 2.3.1 [30]. It has been shown that dye molecules have an increased quantum yield in rigid environments, possibly due to suppression of coupling to rotational modes [56]. The transition dipole moment lies parallel to the surface, usually along the molecule's long-axis [57], and this knowledge is useful in designing experiments for coupling to various photonic devices.

The energy-level scheme of a single DBT molecule embedded in anthracene can be mapped into a three-level system consisting of the electronic singlet ground state S_0 , the first electronic singlet excited state S_1 and a triplet state T_1 [58]. Each state presents a band of vibrational levels, as shown in the Jablonski diagram in Figure 3.1(b).

The purely electronic transition from the lowest vibrational level of S_0 to the lowest vibrational level of S_1 , i.e. the 0-0 ZPL, occurs at around 785 nm in the near-infrared. The lifetime of this transition has been measured to be 4.8 ± 0.5 ns [30], yielding a lifetime-limited linewidth of about 40 MHz at cryogenic temperatures. At room temperature, the emission is peaked at 790 nm with a width of around 50 nm due to the broad phonon wing (see figure 3.2).

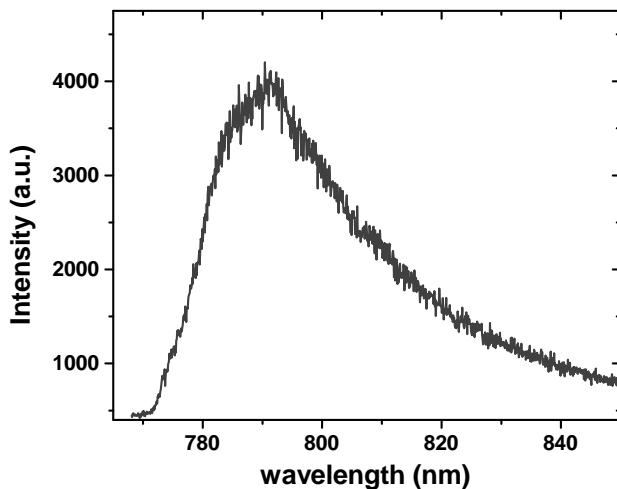


Figure 3.2: Emission spectrum of a single DBT molecule embedded in anthracene at room temperature

As noted earlier, the transition to the triplet state T_1 is spin forbidden and hence occurs with a low probability. When the molecule is in the triplet state, no photons are emitted and going into this dark state is called *blinking*. The triplet state parameters are specific to the dye-host system. Among different organic crystals, anthracene, with its triplet state at 680 nm, is a good host candidate for DBT molecules. In the DBT:Ac system, the triplet state lifetime is found to be equal to 1.5 μ s together with a very low

ISC branching ratio (of about 10^{-7}) [30]. Therefore, when no external loss channels are available, an excited DBT molecule relaxes mainly through radiative emission with a QY close to 1, showing a single exponential decay of the fluorescence intensity, since the anthracene matrix does not contribute to the depopulation of the excited state.

DBT molecules embedded in anthracene exhibit remarkable photostability compared to other dye molecule systems (considered photostable) which photobleach in a few minutes [59]. The samples used in this work were stable upto several days of intermittent use when stored properly, and this system has been shown earlier to survive more than 10 hours of continuous strong illumination [30].

Sample fabrication techniques are as a matter of course, mostly determined by physical properties of the anthracene matrix. Anthracene is a transparent crystalline substance and fabrication of samples thus results in crystalline structures. There are two procedures used in this work to prepare DBT-doped anthracene layers: co-sublimation and spin coating of DBT:Ac mixtures. Co-sublimation is done by heating DBT and anthracene together in a single nitrogen-controlled atmosphere, where pressure and temperature (above the melting point of anthracene at 220 °C) are variables that control the relative concentrations, and the physical properties of the resultant crystals respectively. The pressure used is 240 mbar at temperatures in the range of 300–400 °C. With these values, the concentration of DBT is high and single molecules can only be addressed by resonant excitation at cryogenic temperatures, when their resonant frequencies differ on the order of MHz due to inhomogeneous broadening. The co-sublimated crystals are hexagonal (figure 3.3(a)), with a thickness upward of 150 nm and a wide range of lateral sizes, from tens of micrometers to even a few millimeters. They usually possess better structural quality than spin coated crystals, and are hence better suited for precise low temperature measurements.

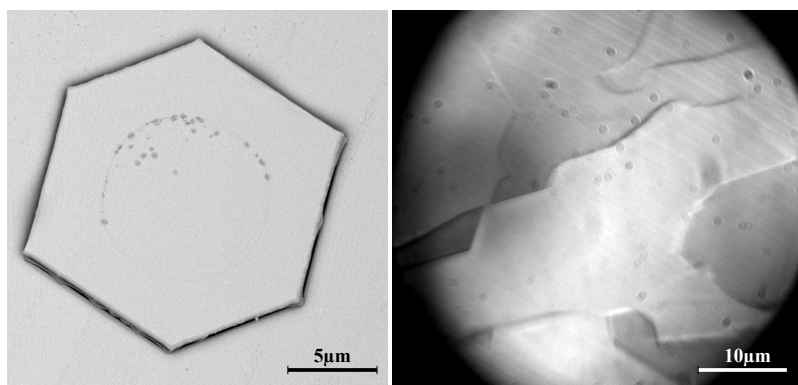


Figure 3.3: (a) SEM image of a co-sublimated DBT:Ac crystal (b) Microscope image of a sample produced by spin coating

For spin coating, anthracene and DBT are dissolved in a suitable solvent such as diethyl ether, and spun on substrates to yield thin crystalline films (which are typically

40 to 80 nm for a spin speed of 3000 rpm). As seen in figure 3.3(b), spin coating of anthracene results in creation of thin films which are of the order of 10 micrometers in lateral dimensions. Final film thickness and other properties highly depend on the nature of the fluid material (viscosity, drying rate, surface tension, etc.) and the parameters chosen for the spin process. While dealing with different substrates, additional parameters such surface hydrophobicity and planarity have to be considered.

Doping emitters into thin films has several advantages, especially in the context of single emitter experiments, as that performed in this work. First, background fluorescence is strongly suppressed due to the optimized ratio between emitter and matrix. Second, emitters in thin films are at limited distances from the surface by design, and thus have access to the near-field in photonic devices. Moreover, they can easily be integrated into a layered structure for a more complex architecture.

As pointed out earlier in section 2.1, it's interesting to use *single* fluorescent molecules to probe various environmental conditions at the microscopic scale. For a DBT:Ac system, this is achieved by simply diluting the concentration of dye molecules. A dye concentration of 1nMolar or below in solution results in crystals showing single bright centers as seen in figure 3.4(b). However, the concentration stated is merely indicative in a manner of magnitude, as exact local concentrations are not easily known.

Figure 3.4 shows the images taken of a typical sin coated sample on a planar surface obtained using the setup described in Chapter 2. Single DBT molecules are $\simeq 1$ nm in size and therefore, appear as diffraction-limited spots in fluorescence images. An intensity profile of a single spot is fitted with a Gaussian function with a FWHM of $0.4\ \mu\text{m}$ which is compatible with the resolution of about $0.3\ \mu\text{m}$ obtained for 767nm excitation. The varying intensity of the molecules can be attributed to different depths in the anthracene crystal and to slightly different orientations of DBT molecules within the host crystalline matrix (and hence different for a fixed excitation polarization that was used to capture the image).

In order to verify that the observed fluorescence signal comes from individual emitters, molecules are singled out and an antibunching measurement is performed in confocal mode with the HBT setup. As discussed in section 2.2, the absence of coincidence at zero delay yields a clear evidence of single photon emission. However in lab experiments, a faint but present background (BG) signal needs to be accounted for, which changes the expected dip-depth of the antibunching curve and can be estimated from the experimental signal-to-background ratio. With typical measured values of 300 kcps for the DBT fluorescence signal and 20 kcps for the overall BG signal ($\text{SNR} \sim 15$), the dip-depth is expected at around $1 - g_2(0) \simeq 88\%$. An experimental autocorrelation function $g_2(\tau)$ is shown in Figure 3.5. It shows a dip at delay $\tau = 16$ ns at which the reduction of the coincidence probability is 89%.

To further characterize the DBT:Ac system, fluorescence saturation curves from several single molecules were recorded by varying the excitation power. As shown in Figure 3.6, the fluorescence signal from a DBT molecule is plotted as a function of the excita-

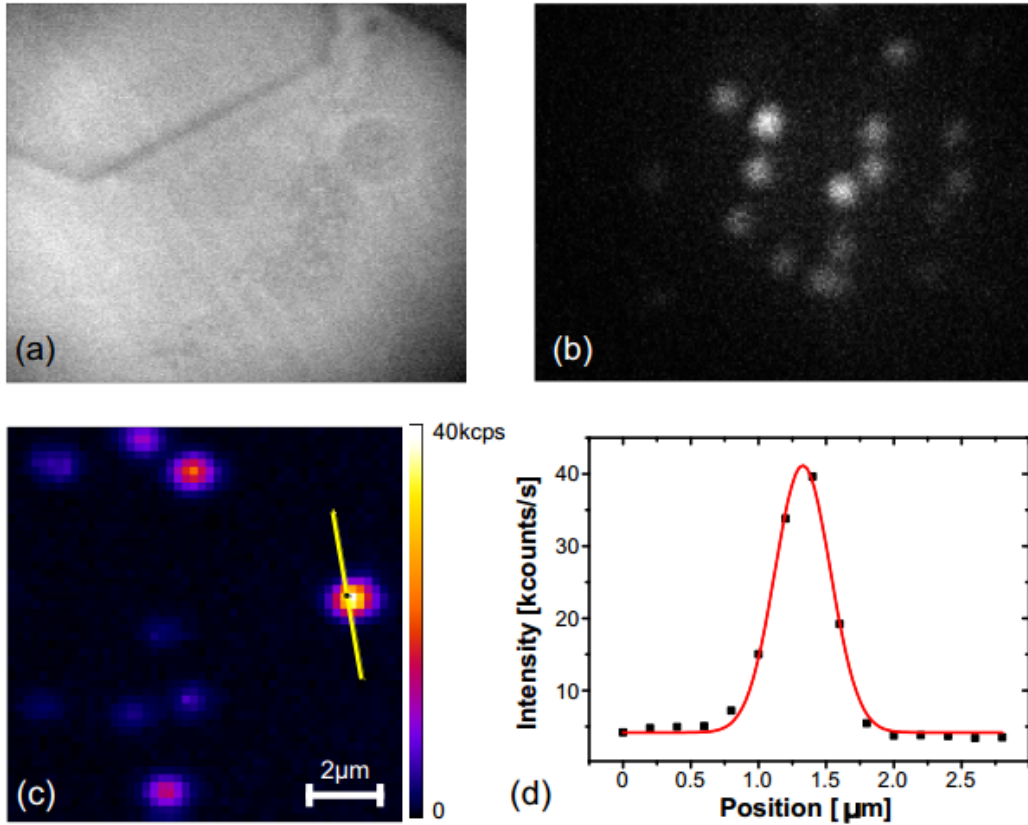


Figure 3.4: (a) Whitelight (b) Widefield (c) Confocal scan (d) Intensity profile for a DBT molecule has a Gaussian shape with a width of $0.4\ \mu\text{m}$. Using the EM-CCD camera, anthracene crystals are first selected using whitelight images, after which single molecules are identified looking at the widefield fluorescence image of the same location. Individual emitters can then be excited confocally to take the required measurements.

tion intensity and fitted with the saturation model given by equation 1.40. The change in intensity of the background signal due to laser scattering is also taken into account and modelled as a linear variation of the excitation intensity.

The fit-procedure (red line) yields a saturation intensity $I_{\text{sat}} = 164.3\ \text{kW cm}^{-2}$ and a detection rate at saturation $N_{\infty} = 2530\ \text{kcsps}$, which are typical values for a reference sample on a glass coverslip observed with an oil objective of $\text{NA}=1.4$. Considering the APD quantum efficiency at about 65%, the maximum value of the collected photon rate comes to $N \sim 3.8\ \text{MHz}$.

At cryogenic temperatures, the interaction with phonons in the matrix is reduced drastically and DBT molecules exhibit a lifetime-limited response in the ZPL. As stated previously, the FWHM of the DBT resonance spectrum is about 40 MHz at 1.4 K. As the laser is scanned over a range within the inhomogeneous broadening ($0.1\ \text{nm} \simeq 50\ \text{GHz}$) caused due to inhomogeneously varying local environments, different molecules light up (in case of widefield excitation) when their ZPL coincides with the incident laser

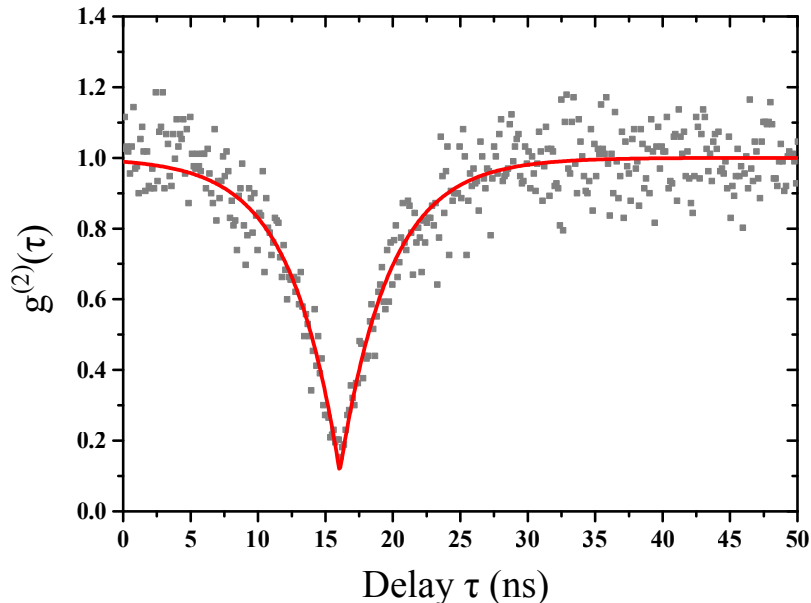


Figure 3.5: Measured photon anti-bunching from single DBT molecule emission without any background correction (grey points). The measured autocorrelation is fitted with the function $g_2(\tau) = 1 - Ce^{(\gamma\tau)}$ (see equation 2.6), where $\gamma = \gamma_{\text{abs}} + \gamma_{\text{spon}}$ is the decay parameter and C is the contrast of the measured correlation, which is reduced by the BG signal (red curve). The experimental coincidence reduction obtained at zero-time delay is 89%, which is perfectly compatible with the expected value of about 88%.

frequency. Figure 3.7 shows the excitation spectrum of a molecule excited confocally at 2.9 K with linewidth of 52.6 MHz. As expected, the linewidth increases as a function of both incident power and temperature (according to the Arrhenius relation [60]).

Stable single photon sources such as the DBT:Ac system described in this chapter are sought after for on-demand photon production in many areas, both in fundamental science and quantum-information-processing applications. At low temperatures, when the coherence times are high, indistinguishable photons from such sources enable interference mechanisms and longer transport paths in quantum-optical circuits. At room temperatures, they are used as non-linear media to probe local nanometric conditions and observe coupling mechanisms with photonic structures.

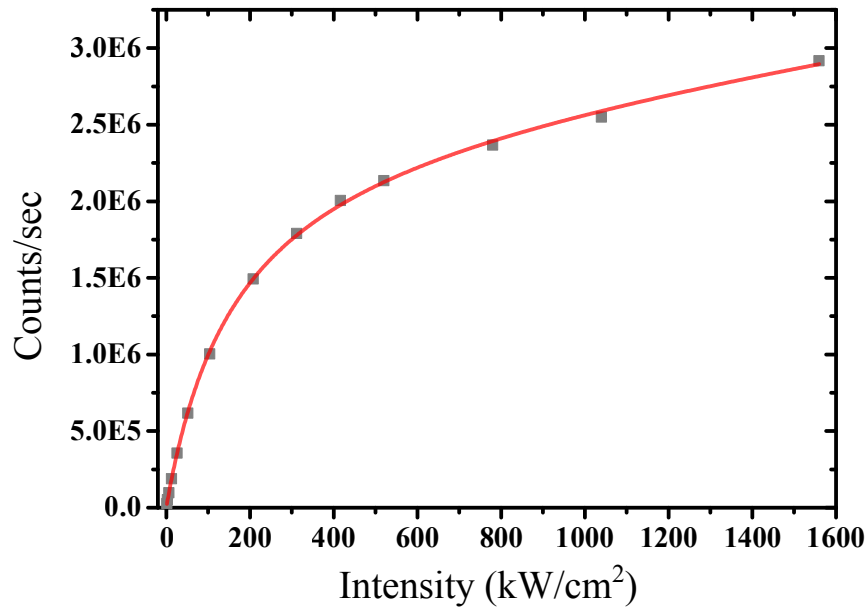


Figure 3.6: Detected rates for the fluorescence of a single DBT molecule performed with the CW red laser in confocal configuration and plotted as a function of the excitation intensity. The fluorescence signal is fitted with the function $N_{\text{det}}(I) = N_{\infty}(1 + I_{\text{sat}}/I)^{-1} + bI$, where referring to equation (1.40), N_{∞} is the maximum value reachable by the photon rate due to the emitter saturation, I_{sat} is the saturation intensity, and b is the factor representing linear-dependency of the background count rate on excitation intensity.

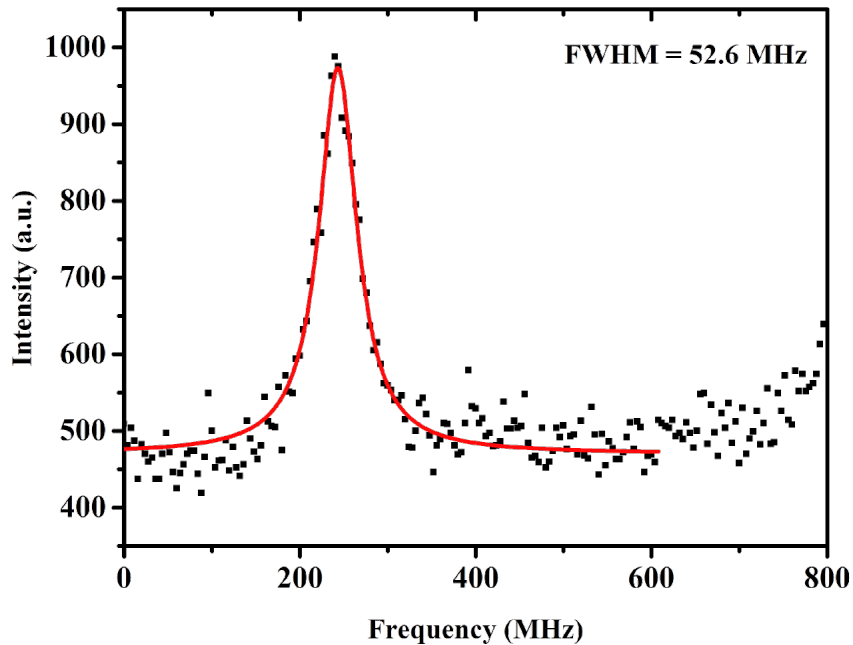


Figure 3.7: Linewidth of a DBT molecule at a temperature of 2.9K.

4 Angular emission patterns in multilayer systems

A point dipole emits isotropically in all directions when placed in a homogeneous medium, and even today with all the advanced high numerical aperture (NA) optics available, routine experiments suffer from low light collection efficiencies. This is specially relevant for single molecule studies where signal-to-noise ratio (SNR) is inherently low, and device configurations with low NA such as optical fibers used in on-chip light transport. To increase the emission collection efficiency, dielectric cavities are often discussed, but they require complicated structures and have low spectral widths. In this chapter, we propose a novel and simplistic design of an optical antenna for collection of emission from fluorescent molecules, which does not require elaborate sample preparation and can be adapted to serve in a wide range of operating wavelengths.

Such a design has been achieved using highly reflective planar metal films. As discussed in section 1.4, there are mainly three phenomena that take place for an emitting dipole and a metal interface at distances comparable to the emission wavelength λ : decay into photons (with modified wavevectors compared to free space emission), coupling to surface waves, and coupling to lossy channels in the metal. These coupling mechanisms occur predominantly at different distances from the metal-dielectric interface. At higher distances in this range, there is negligible effect on the decay rate of the emitter due to little change in the available density of states, and the final effect is manifested mainly in the angular emission profile of far-field radiation, due to the interference of the emitted field and the field reflected by the metal surface.

Here we use a model for the simulation of this physical scenario (in which absorption and transmission losses are taken into account) based on the one presented in [61], and then the experimental realization is compared with the simulated results. The high correlation between simulation and experiment verifies the model and provides a way to design antennas for maximum power collection efficiency from radiating sources in different scenarios. The final model was developed and programmed in MATLAB by Ms. Simona Checcucci, and I was involved in the fabrication of samples and their experimental investigation.

4.1 Design principle

The propagation of optical waves in and through thin films is governed by their complex refractive indices and therefore, light propagation through a multilayer structure with well-defined interfaces is affected by the complex reflection and transmission coefficients, known as *Fresnel coefficients*, at each successive interface. Due to reflections, there is also a high probability of observing interferences, which become important in certain special cases and result in an emission limited to certain preferential directions. To predict the final distribution of light emitted by a source embedded within such a system, the effect of each successive layer is modelled using Fresnel coefficients and applied iteratively, resulting in a net coefficient containing the behaviour of all layers towards the incident field vector. In the following discussion, a brief description of such a model is presented.

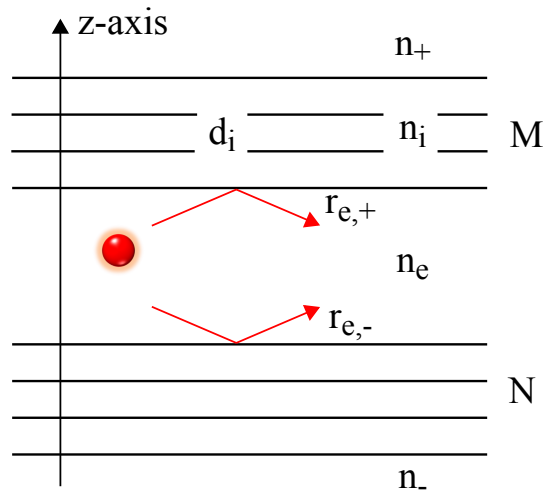


Figure 4.1: Thin-film structure: active medium containing the emitter with refractive index n_e and thickness d_e situated between a number of M and N layers. The axis perpendicular to the plane of the thin films is assigned as the z -axis.

Consider a thin film multilayer structure shown in figure 4.1, with an active medium with refractive index n_e and thickness d_e situated between a stack of M and N layers in either direction, each layer characterised by thickness d_i and index of refraction n_i . The emitter lies in the active layer with an arbitrary orientation. The axis perpendicular to the plane of the thin films is assigned as the z -axis, and thus all films are oriented parallel to the x - y plane. The furthestmost layers in the $+z$ and $-z$ directions are semi-infinite media with refractive indices denoted by n_+ and n_- respectively. The emitting layer is considered to be non-absorbing and hence n_e is a real number, while the other layers are defined by complex indices of refraction, which means they can be transmitting or absorbing depending on assigned values. Finally, all media are considered linear, homogeneous and isotropic.

Given that the materials involved are linear, each frequency component of the light interacts independently with the media, and therefore, we consider only a single monochromatic source of angular frequency ω and free space wavelength given by $\lambda = 2\pi c/\omega$, where c is the velocity of light. By Fourier analysis, each wavevector component of the electric (or magnetic) field associated with this monochromatic wave can be expanded into plane waves [62]. In linear media, the propagation of these waves is described by linear differential Maxwell's equations, and thus individual waves do not influence each other. This means that the total field vector at each point is always the sum of individual field vectors. In interference phenomena, the reason for the apparent interaction between waves is that the quantity observed is not the field amplitude of the waves but the energy density (represented by intensity), which is a non-linear function of the em field.

In a material with index of refraction n_i , the amplitude of the wavevector is given by:

$$k_i = 2\pi n_i/\lambda = (k_{\parallel,i}^2 + k_{z,i}^2)^{1/2}$$

or conversely, $k_{z,i} = (k_i^2 - k_{\parallel,i}^2)^{1/2}$ (4.1)

where $k_{\parallel,i} = (k_{x,i}^2 + k_{y,i}^2)^{1/2}$ is the in-plane component of the wavevector. By equation 4.1, depending on the magnitude of $k_{\parallel,i}$ with respect to k_i , $k_{z,i}$ can be imaginary and represent evanescent fields that decrease exponentially in both directions; or it can be real, signifying plane waves with a propagation direction at an angle θ with the z -axis with:

$$k_{\parallel,i} = k_i \sin \theta$$

$$k_{z,i} = k_i \cos \theta \tag{4.2}$$

where $\theta < \pi/2$ for waves travelling in the $+z$ direction and $\theta > \pi/2$ for waves in the $-z$ direction, as shown in figure 4.2(a). When k_i is not real or its value is less than $k_{\parallel,i}$

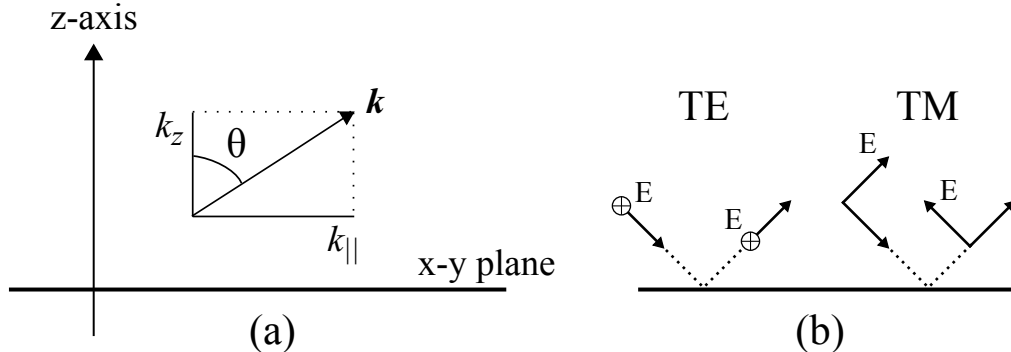


Figure 4.2: (a) wavevector k of a plane wave making an angle θ with the z -axis (b) TE and TM polarizations

(resulting in an imaginary $k_{z,i}$), the wave is evanescent and it is not possible to assign a real angle θ for the propagation of this wave. In this problem, plane and evanescent waves can have a TM or TE polarization, and hence polarizations have to be taken into account. For the sign conventions shown in figure 4.2(b), the complex Fresnel coefficients for reflection of a wave in medium n_i on an adjacent medium n_{i+1} are given as:

$$r_{i,i\pm 1}^{\text{TM}} = \frac{\frac{k_{z,i}}{n_i^2} - \frac{k_{z,i\pm 1}}{n_{i\pm 1}^2}}{\frac{k_{z,i}}{n_i^2} + \frac{k_{z,i\pm 1}}{n_{i\pm 1}^2}}, \quad r_{i,i\pm 1}^{\text{TE}} = \frac{k_{z,i} - k_{z,i\pm 1}}{k_{z,i} + k_{z,i\pm 1}}. \quad (4.3)$$

and the corresponding transmission coefficients are given by $t_{i,i\pm 1} = 1 + r_{i,i\pm 1}$.

As stated earlier, in the case of multiple layers in either direction, the calculation of the net effective reflection and transmission coefficients is done by taking into account the effect of each interface iteratively, starting from the outermost semi-infinite layers. In this way, it is possible to arrive at a structure composed of a single medium containing the emitter enclosed by two semi-infinite materials on each side, where information about the presence of other interfaces is contained within the net reflection and transmission coefficients:

$$r_{i,j} = \frac{r_{i,i\pm 1} + r_{i\pm 1,j} \exp(2ik_{z,i\pm 1}d_{i+1})}{1 + r_{i,i\pm 1}r_{i\pm 1,j} \exp(2ik_{z,i\pm 1}d_{i+1})} \quad (4.4)$$

$$t_{i,j} = \frac{t_{i,i\pm 1}t_{i\pm 1,j} \exp(ik_{z,i\pm 1}d_{i+1})}{1 + r_{i,i\pm 1}r_{i\pm 1,j} \exp(2ik_{z,i\pm 1}d_{i+1})} \quad (4.5)$$

using the relation at each interface: $r_{i\pm 1,i} = -r_{i,i\pm 1}$.

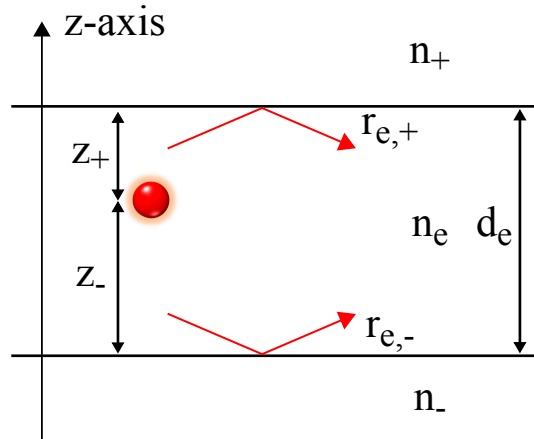


Figure 4.3: Dipole position in the resultant three-layer structure located at a distance z_+ from the interface on the $+z$ side and z_- from the interface on the $-z$ side. The two outer layers represent the sum effect of all the other layers by using a net Fresnel coefficient that contains their behaviour.

To evaluate the radiated power from the dipole transmitted outside the multilayer structure, we consider the situation shown in figure 4.3. The dipole with a dipole moment \vec{p}_0 and angular emission frequency ω , is positioned at the origin inside the lossless medium with refraction index n_e and thickness d_e . If the medium is infinite, the total power radiated by the dipole would be [63]:

$$L_{\infty,e} = \frac{\omega k_e^3}{12\pi n_e^2 \epsilon_0} p_0^2 \quad (4.6)$$

where k_e is the emission wavevector in the medium and ϵ_0 is the free space permittivity. This is the total power radiated by the dipole and is defined as the time-average of the normal component of the energy flow density $\langle S \rangle = 1/2 \text{Re} \{E \times H\}$ through a surface enclosing the dipole, and can be calculated by integrating the Poynting vector \vec{S} over all polar angles θ and azimuthal angles ϕ . For the calculation of the em field generated by an electric dipole in the presence of multiple interfaces, the net field can be decomposed into three components: one for the field directly emitted by the dipole and the other two for the reflected fields from the top and bottom interfaces, where each component can in turn be further broken down into propagating and evanescent modes. By using the superposition of plane and evanescent waves, the total power radiated $L(\vec{x}_0)$ by the dipole, normalised to the power emitted in an infinite medium, can be written as:

$$\left(\frac{L(\vec{x}_0)}{L_{\infty,e}} \right) = \int_0^\infty K(k_{\parallel}) dk_{\parallel}^2 \quad (4.7)$$

where \vec{x}_0 is the position of the dipole and K is the power density per unit dk_{\parallel}^2 [63, 64]. For an electric dipole making an angle θ with the z -axis, the radiated power is simply the sum of two contributions:

$$K_\theta = K_{\perp} \cos^2 \theta + K_{\parallel} \sin^2 \theta \quad (4.8)$$

If the dipole is located at distance z_+ and z_- from the upper and lower interfaces respectively as shown in figure 4.3, the power densities for a dipole oriented perpendicular to the plane are given by:

$$\begin{aligned} K_{\perp}^{\text{TM}} &= \frac{3}{4} \text{Re} \left[\frac{k_{\parallel}^2}{k_e^3 k_{z,e}} \frac{(1 + a_+^{\text{TM}})(1 + a_-^{\text{TM}})}{1 - a^{\text{TM}}} \right] \\ K_{\perp}^{\text{TE}} &= 0 \end{aligned} \quad (4.9)$$

and for a dipole parallel to the plane, they are given by:

$$\begin{aligned} K_{\parallel}^{\text{TM}} &= \frac{3}{8} \text{Re} \left[\frac{k_{z,e}}{k_e^3} \frac{(1 - a_+^{\text{TM}})(1 - a_-^{\text{TM}})}{1 - a^{\text{TM}}} \right] \\ K_{\parallel}^{\text{TE}} &= \frac{3}{8} \text{Re} \left[\frac{1}{k_e k_{z,e}} \frac{(1 + a_+^{\text{TE}})(1 + a_-^{\text{TE}})}{1 - a^{\text{TE}}} \right] \end{aligned} \quad (4.10)$$

where Re stands for the Real part, while $a_+^{\text{TM/TE}}$ and $a_-^{\text{TM/TE}}$ are the reflection coefficients corresponding to the location of the dipole inside the emitting medium:

$$\begin{aligned} a_+^{\text{TM/TE}} &= r_{e,+}^{\text{TM/TE}} \exp(2ik_{z,e}z_+) \\ a_-^{\text{TM/TE}} &= r_{e,-}^{\text{TM/TE}} \exp(2ik_{z,e}z_-) \end{aligned} \quad (4.11)$$

Here the superscript TM/TE has been used to denote TM *or* TE polarization, one factor for each one. Thus the factor a^{TM} is the product of a_+^{TM} and a_-^{TM} with similarly the corresponding term for TE polarization. Then using the relations above:

$$a^{\text{TM/TE}} = a_+^{\text{TM/TE}} a_-^{\text{TM/TE}} = r_{e,+}^{\text{TM/TE}} r_{e,-}^{\text{TM/TE}} \exp(2ik_{z,e}d_e) \quad (4.12)$$

In equations 4.9 and 4.10, the factor $(1 \pm a_+)(1 \pm a_-)/(1 - a)$ accounts for the interferences that take place due to the multilayer structure. The factor $(1 \pm a_+)(1 \pm a_-)$ in the numerator describes the wide-angle interference between directly emitted and reflected radiation that have the same k-vector, and thus the distance of an emitter from the interface plays an important role. The factor $(1 - a)$ in the denominator describes multiple-beam interference, which occurs when a single beam is repeatedly reflected between two interfaces, yielding an infinite sum: $1 + a + a^2 + a^3 + \dots$, which then amounts to $1/(1 - a)$ as the sum of this geometric progression.

Recalling that wavevectors $k_{\parallel} > k_e$ will result in the formation of evanescent waves (equation 4.1) which when formed at both interfaces, can also interfere provided that the emitting medium is thin enough to make a spatial overlap possible. The net field resulting from this superposition can then also undergo multiple reflections as discussed above, and thus produce multiple-wave interference. When the spatial overlap is not possible, the evanescent waves decay exponentially in their respective media. In the case where one of the media is absorbing with a complex refractive index, energy can be transported through such evanescent waves and give rise to surface polaritons.

For the emission into the medium in the $+z$ direction with an angle θ , by using equation 4.7, the power density $P(\theta)$ per solid angle $d\Omega$ can be calculated by:

$$\frac{L_+(\vec{x}_0)}{L_e} = \int_0^{2\pi} [P_+^{\text{TE}}(\theta, \phi) + P_+^{\text{TM}}(\theta, \phi)] d\Omega \quad (4.13)$$

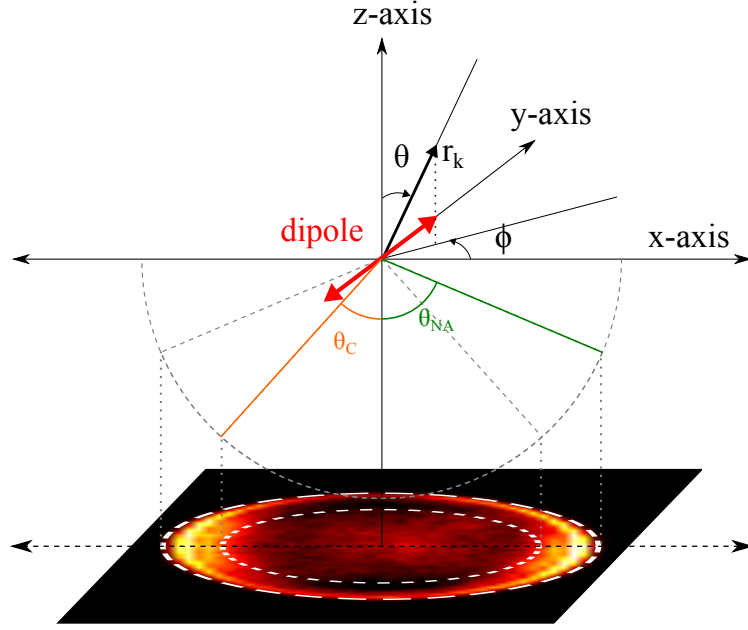


Figure 4.4: Schematic depicting the mapping of k -vectors in the BFP, where the direction is represented by vector r_k with a polar angle θ and an azimuthal angle ϕ . A sample BFP pattern for a horizontal dipole oriented along the y -axis is shown where θ_c is the critical angle for a glass-air interface and θ_{NA} is the maximum angle collected by the objective.

Integrating over the azimuthal angle ϕ , for a dipole perpendicular or parallel to the plane, (due to the rotational symmetry around z -axis) we get:

$$\begin{aligned} \int P^\perp(\theta, \phi) &= 2\pi P(\theta) \\ \int P^\parallel(\theta, \phi) &= \pi P(\theta) \end{aligned} \quad (4.14)$$

Now by using the relation $k_\parallel = k \sin \theta$, the angular distribution is related to the transmitted power $K_{+,T}$ by:

$$\begin{aligned} P_+^\perp(\theta_+) \cdot 2\pi \sin \theta_+ d\theta_+ &= K_{+,T}^\perp(k_\parallel) dk_\parallel^2 \\ P_+^\parallel(\theta_+) \cdot \pi \sin \theta_+ d\theta_+ &= K_{+,T}^\parallel(k_\parallel) dk_\parallel^2 \end{aligned} \quad (4.15)$$

for $K = K_+ + K_-$ and in turn, $K_\pm = K_{\pm,A} + K_{\pm,T}$ where A and T signify absorption and transmission into the far-field respectively. This finally gives:

$$\begin{aligned} P_+^\perp(\theta_+) &= \frac{k_+^2 \cos \theta_+}{\pi} K_{+,T}^\perp(k_+ \sin \theta_+) \\ P_+^\parallel(\theta_+) &= \frac{k_+^2 \cos \theta_+}{2\pi} K_{+,T}^\parallel(k_+ \sin \theta_+) \end{aligned} \quad (4.16)$$

These relations give the expression for the power density radiated by the dipole in the outermost semi-infinite media, but not all of it is collected due to the limited numerical aperture of a real objective lens. An objective collects a fraction of this emitted light in a range of angles from 0 to β determined by its NA, and can be calculated by the following expression:

$$P_{coll}(\beta) = \int_0^\beta P(\theta) \sin \theta \, d\theta \quad (4.17)$$

This limitation hampers the performance statistics of photonic devices and has driven various experiments, like this one, to engineer maximum collection efficiency from radiating sources using low NA optics.

The model outlined above describes the working principle of many light emitting devices based on thin-film technology [65, 66]. In this work, it was utilised for identifying special cases which result in high light-collection efficiencies in a preferential direction, simultaneously keeping the device structure as flexible and cost-effective as possible. All experiments have been carried out with DBT molecules embedded in anthracene (DBT:Ac), which forms the emitting layer, and the emission dipole of the DBT molecule lies parallel to the plane of the layer. The wavelength of emission is around 785 nm and the anthracene forms thin layers with thicknesses about 50–80 nm by spin coating, which have a real refractive index of 1.6. The angular emission patterns were observed using the BFP imaging setup, which can map emission wavevectors onto radial space vectors in the back focal (Fourier) plane of the objective, and then onto the CCD camera. It has been described in section 2.3.1.

4.2 Reference sample

To first test the BFP setup and characterize the emission of the dipole embedded in anthracene, a reference sample was taken with a DBT:Ac layer spin coated over a glass coverslip with a refractive index of 1.5. The oil objective with NA=1.4 ($\theta_{max} = 67^\circ$) is placed at the top to collect the emitted signal and interfaced with the sample with a refractive index matching oil, thus resulting in a continuous medium of RI $\simeq 1.5$ which can be considered semi-infinite.

Figure 4.5(a) depicts the reference configuration in which a DBT molecule is embedded in anthracene and its dipole is oriented parallel to the substrate. A simulation of the emission pattern is shown in (b) where the intensity distribution represents the power distribution $P(\theta)$ in k-space as a function of the (polar) angle of emission, and the distance from the center represents the angle with reference to the out-of-plane z -axis. However it worth mentioning here that the power $P(\theta)$ does not correspond to the absolute value of radiated power, but rather to the power normalised to the power radiated by the dipole in free space, as given in equation 4.7. As seen in (b), most of the emission lies beyond the critical angle, the main contribution being the conversion of evanescent waves in the near-field of the dipole into plane waves propagating in the

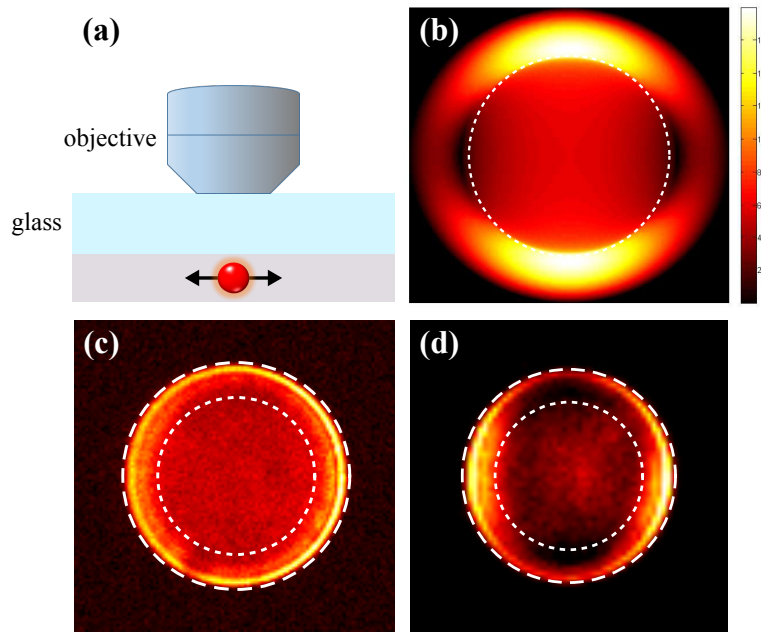


Figure 4.5: (a) Reference sample configuration where the dipole of a DBT molecule in anthracene (RI=1.6) lies parallel to the plane of the glass substrate. (b) Simulated emission pattern with the z -axis pointing out of the plane towards the observer, and hence growing distance from the center represents increasing polar angle θ while the azimuthal angle ϕ lies in the plane (visualized in figure 4.4). The intensities in the figure represent $P(\theta)$ at corresponding angles in the back focal plane. Experimentally obtained (c) High concentration and (d) Single molecule emission patterns. The inner circle corresponds to the critical angle and the outer circle corresponds to maximum angle collected by the objective.

far-field in glass, due to wavevector matching [44]. In the sample, the emitter is situated in the middle of the anthracene layer, with a certain variability in height. Simulations were made with different heights of the dipole inside the anthracene layer from 0-80nm and power densities as a function of polar angle θ were calculated. They are plotted in figure 4.6 along with the cutoff indicated at a certain angle ($\theta_{max} = 67^\circ$) corresponding to the maximum angle that can be observed with given NA of the objective. It is apparent, considering the system response, that the height of the dipole inside the emitting medium does not cause much deviation in the final collected power. Following this conclusion, each new configuration was first tested with a high concentration of molecules for a better signal to noise ratio, since averaging over light from molecules at different heights does not qualitatively change the final result. Single molecule studies were performed thereafter, thus fully verifying the simulated versions. Note that the emission patterns obtained with high concentration is a summation of signals from individual molecules and spread over a wider range of azimuthal angles, and hence appear

as bright *rings* (figure 4.5(c)) instead of *lobes* in case of single molecules as shown in (d).

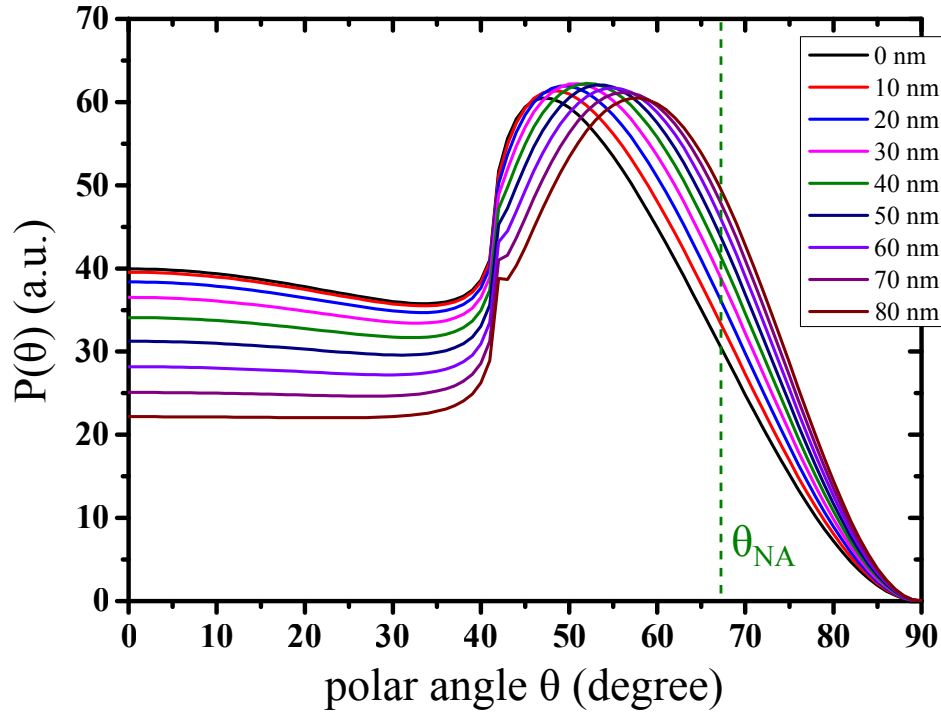


Figure 4.6: Power density integrated over all azimuthal angles ϕ , as a function of polar angle θ for a DBT molecule embedded in anthracene at different distances from the interface with air as indicated in the legend. The dashed line represents the cutoff angle for the objective.

4.3 Planar optical antennas

This section enlists the various configurations of multilayer antennas that were investigated experimentally, drawing parallels with the simulated results. Two main configurations have been exploited: when a highly reflecting metal surface (mirror) is placed at the bottom, the reflection from that interface interferes with the direct dipole emission and results in higher transmission from the top side, which can be calculated according to equation 4.16. The other configuration is a modification of the first one - a thin transmitting metal layer is placed on the top side, which modifies the interference effect due to a higher number of reflections and finally results in *beam-forming*, where the final angular distribution of light is in a narrow cone of angles along the transverse $+z$ -direction. These two configurations have been explained in the following subsections.

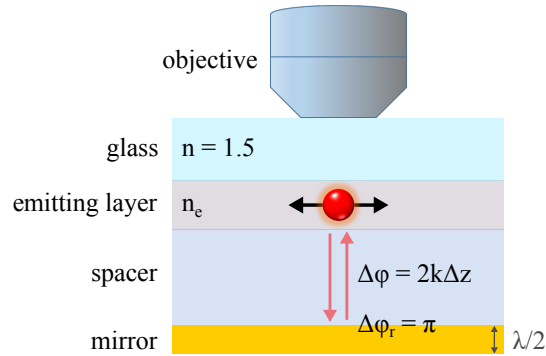


Figure 4.7: One-mirror configuration: the metal mirror at the bottom reflects the field and interferes with the direct emission. Changing the distance of the dipole from the mirror changes the phase of the reflected wave with respect to the original wave.

4.3.1 One mirror configuration

Figure 4.7 shows the layout of the one-mirror configuration. The dipole emitter lies in the emitting medium of refractive index 1.6. It is separated by the mirror by a dielectric *spacer* layer, whose thickness is taken as a variable since it determines the phase difference between the reflected and the original waves at the position of the dipolar emitter. When the total phase shift for $\theta = 0$ becomes even multiples of π , there is a constructive interference effect which produces a brighter net signal in the transverse direction towards the objective. This can be achieved, for example, by using a spacer thickness of $\lambda/4n$. The π phase shift due to the path length (crossed twice after reflection) and π due to the reflection at the interface, results in a wave that is in step with the wave directly generated by the source, and propagating in the same direction. The metal layer at the bottom called the *reflector* is defined by a complex refractive index, and is modelled to have a thickness of $\lambda/2$ for high reflectivity and such that the thickness is much bigger than the skin depth inside gold at 785 nm.

Sample preparation

Referring to figure 4.7, the samples were fabricated with a top-down approach. The DBT:Ac layer was deposited on a reference glass coverslide (RI=1.52) by a spin coating process at 3000 rpm for depositing thin crystals. After which, the dielectric spacer was fabricated. Uniform deposition of this spacer layer is crucial, and polymers were chosen for their ease of fabrication and film uniformity¹. Polyvinyl alcohol (PVA) is a water-soluble polymer which is easily spin coated into thin films, and has an average refractive index of 1.5. PVA layers of different thicknesses were obtained by

¹Many different polymers were tested for this purpose (for example, PVA, PMMA, custom polymers like IP-Dip, IP-G, etc) and selected according to their optical quality and above all, compatibility with the fabrication of other layers in the structure.

changing the concentration (and hence, viscosity) of the PVA-in-water solution, and the rotation speed used for spin coating. Resultant film thicknesses were measured with an interferometric microscope Zygo® (at the Istituto Nazionale di Ottica, CNR), and multiple measurements were taken at different points on a sample to evaluate the mean value and standard deviation. It was observed that the uniformity of the polymer films worsened with increasing viscosity (concentration), which can be explained by considering that a higher resistive force is exerted by the liquid of a higher viscosity against the centrifugal force exerted during spin coating. Finally on top of this spacer, a 100 nm gold film was deposited by sputter-coating, which serves as the reflector layer.

The thickness of the spacer layer can be varied to tune the interference between the direct field and the field scattered by the highly reflecting interface, and different thicknesses were investigated for this purpose. Figure 4.8 shows the simulated radiation patterns obtained with various values of spacer-thickness. Higher-order fringes start to appear after the thickness reaches λ/n .

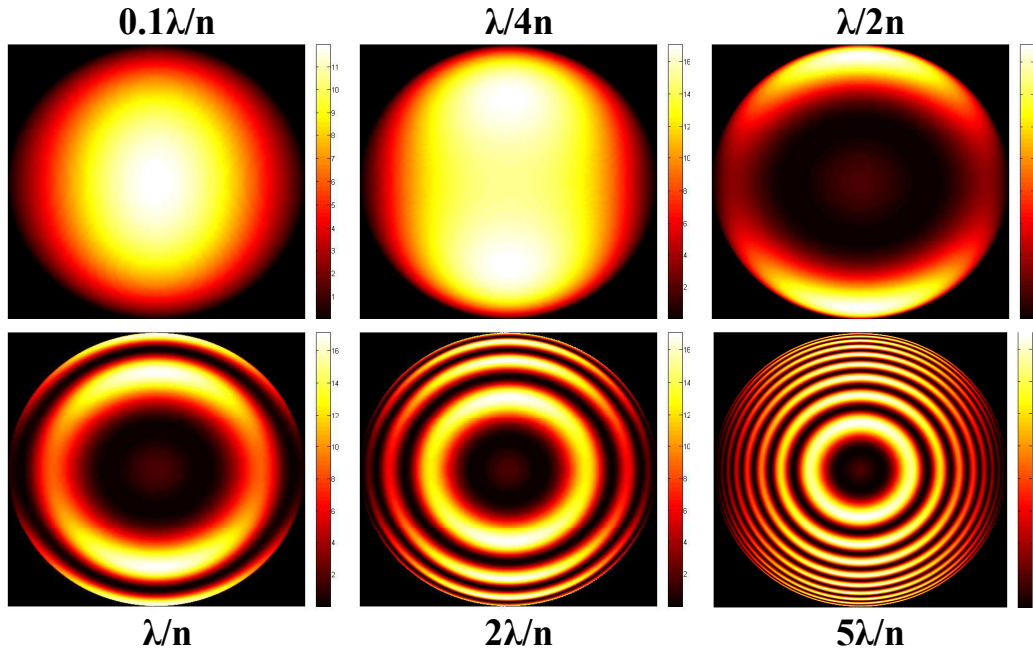


Figure 4.8: Simulated radiation patterns by varying the thickness of the spacer layer (indicated in black text) which has refractive index $n = 1.5$.

To compare different cases, it's required to quantify the amount of light emitted according to the radial angle θ . Figure 4.9 shows the power distribution integrated over the azimuthal angle ϕ for dipoles at different distances from the metal layer, in the range of 40–130 nm (where no dark fringes are seen).

As seen in figure 4.9, the amount of radiative power emitted by an emitter near a metal interface starts decreasing when the emitter is brought closer than 100 nm. This can be compared to figure 1.6 in section 1.4, and explained by the opening up of non-radiative channels at shorter distances to the metal, which results in coupling to surface

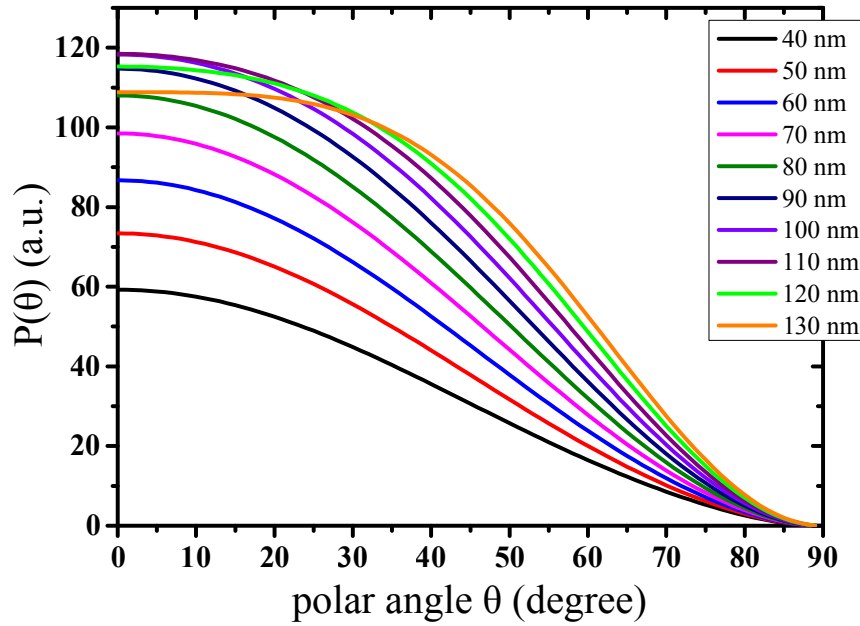


Figure 4.9: Power density as a function of polar angle θ for a DBT molecule embedded in semi-infinite medium with refractive index $n=1.5$, at different distances from the mirror.

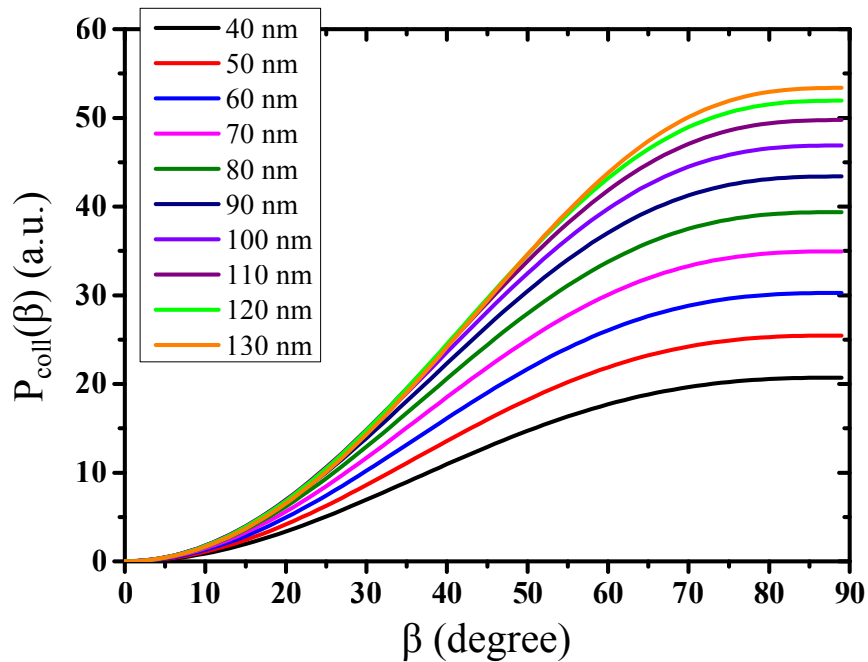


Figure 4.10: Power collected over polar angles from 0 to β , for a DBT molecule embedded in semi-infinite medium with refractive index $n=1.5$, at different distances from the mirror.

plasmons and other dissipative mechanisms. Moreover, it is necessary to consider that some destructive interference can take place and diminish the overall intensity.

This variation is also visible in the power collected by the detector, which is however limited to a given range of angles (equation 4.17) from 0 to β determined by the optical parameters of the system (for example the NA of the objective used). Figure 4.10 shows the collected powers for the same cases as shown in figure 4.9. Note that even at 90° , the magnitude of collected power does not equal the emission power, since the intensities collected are a only projection of the emission intensities on to a flat plane of the detector.

Among different cases for the emitter-reflector distance, three cases were selected for experimental observation that exhibit characterizing features in the emission pattern and span a range of phase shifts. These are summarised in the table shown in figure 4.11.

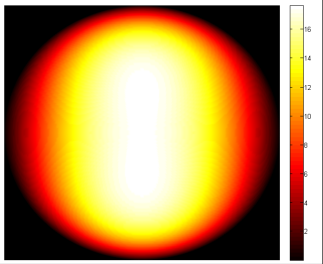
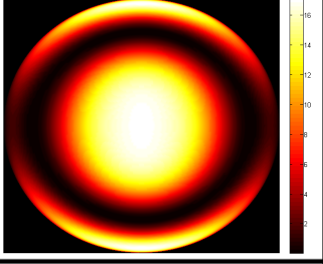
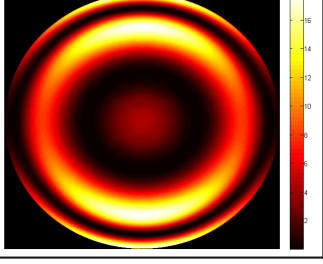
Nickname: ‘Optimal’	
Emitter-reflector distance: 75-130 nm	
Spin parameter: 3% conc. PVA @ 5000 rpm	
Nickname: ‘Internal bright spot’	
Emitter-reflector distance: 340-390 nm	
Spin parameter: 5% conc. PVA @ 1500 rpm	
Nickname: ‘Internal bright ring’	
Emitter-reflector distance: 460-510 nm	
Spin parameter: 7% conc. PVA @ 1500 rpm	

Figure 4.11: Angular emission patterns for 3 particular cases with different thickness of the PVA spacer layer.

Emission patterns were obtained for the above cases, using both single molecule and high concentration samples. Single molecule measurements, free from ensemble-averaging, are expected to show results that resemble the simulations to a higher degree (which are done with single dipoles inside the multilayer structure). As discussed previously in Chapter 3, single molecules can be located by wide-field imaging, and then selectively excited in the confocal mode. Several observations were recorded to

ensure variability in crystal thickness and emitter position, thus making it possible to aptly assess the robustness of the proposed antenna structure.

Emitter-reflector distance 75–130 nm

The 'optimal' configuration has an angular power distribution spread across a large range of angles but still mostly contained within the numerical aperture of the objective (NA=1.4) used. It was realized with a PVA spacer film thickness of about 75 nm combined with the range of distances that a DBT molecule can reside inside the anthracene film (average thickness 50 nm). Figure 4.12 shows the simulated and observed BFP images for DBT molecules embedded in such a system. It is evident that the resultant emission is free from dark interference fringes and fits within the NA of the objective. Note again that images for an ensemble of emitters, with each one having its own azimuthal angle in the crystal plane, is a superposition of their emission patterns which results in a uniform circle of radiation rather than a lobe resembling the simulated version.

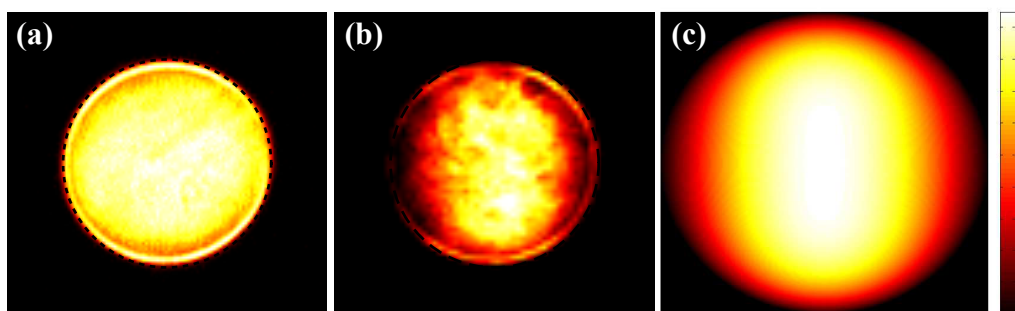


Figure 4.12: Experimentally observed angular emission patterns with a PVA spacer layer thickness of 75 nm for (a) High concentration and (b) Single molecule concentration of DBT molecules in anthracene. (c) Simulated version for the same structure where the height of the molecule inside the crystal is taken to be 30 nm, to closely represent the experimental case.

Emitter-reflector distance 340–390 nm

PVA with 5% concentration in water was spin coated at 1500 rpm yielding thin films with an average thickness of 340 nm. Using this as the spacer layer resulted in a peculiar emission pattern characterised by a big bright spot in the center surrounded by a dark fringe and then a bright fringe at larger angles. As mentioned earlier, the interference between primary and secondary emitter fields starts to show bright and dark fringes at the second order with a total phase difference of 3π which corresponds to a PVA spacer thickness of 260 nm. Figure 4.13 shows the 'internal bright spot' in both the observed and simulated images, and as expected the outermost bright ring is barely

visible because of the limited NA of the objective corresponding to a polar angle of 67° compared to the 90° displayed in the simulation.

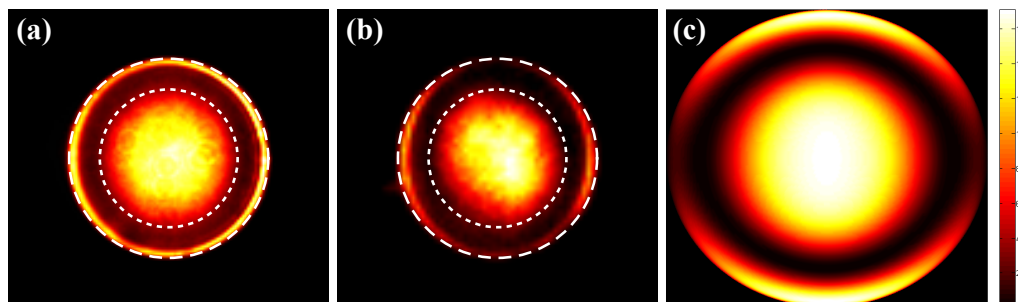


Figure 4.13: Experimentally observed angular emission patterns with a PVA spacer layer thickness of 340 nm for (a) High concentration and (b) Single molecule concentration of DBT molecules in anthracene. (c) Simulated version for the same structure where the height of the molecule inside the crystal is taken to be 20 nm, which closely represents the experimental case. The inner dashed circle corresponds to the critical angle and the outer circle corresponds to the maximum angle collected by the objective.

Emitter-reflector distance 460–510 nm

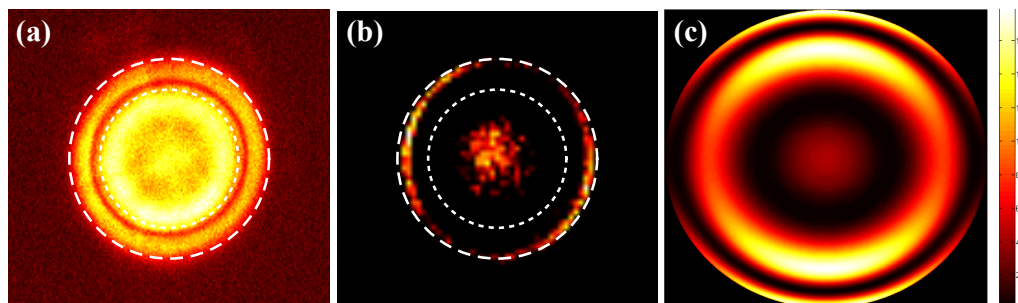


Figure 4.14: Experimentally observed angular emission patterns with a PVA spacer layer thickness of 460 nm for (a) High concentration and (b) Single molecule concentration of DBT molecules in anthracene. (c) Simulated version for the same structure where the height of the molecule inside the crystal is taken to be 30 nm, which closely represents the experimental case. The inner dashed circle corresponds to the critical angle and the outer circle corresponds to the maximum angle collected by the objective.

The third case investigated in experiments was the 'internal bright ring' configuration, where the PVA spacer thickness was around 460 nm over DBT:Ac crystals which have a typical thickness of around 50 nm. As the emitter-reflector distance is increased,

more interference fringes appear, and in this particular case, we observe a dim spot at the very center accompanied by alternate dark and bright rings going out towards higher angles. As seen in the observed patterns shown in figure 4.14(a) and (b), the image is modulated by the system response that cuts off the emission at higher angles. However, the first bright ring is better observed in (b) with a high concentration of molecules, and this can be the result of the variation in spacer-thickness, since simulations show that the position of the fringes tends to move inward with decrease in the emitter-reflector distance. As mentioned earlier, when higher thicknesses of the PVA polymer layer are spin coated (on top of the DBT:Ac crystal layer), the deviation in height tends to be more than for spin coating of thin films, and the superposition of signals from DBT molecules at different heights in the anthracene crystal can blur out the interference fringes. Additionally due to this non-uniformity, part of the emission from molecules closer to the metal layer can excite guided modes on the metal surface called surface plasmon polaritons, and these can scatter back into the glass medium at specific angles θ_{SPP} governed by the resonance condition at the signal wavelength, thus forming additional rings that are visible in the back focal plane. Such an emission is called surface plasmon coupled emission and is discussed in section 5.3.

4.3.2 Two mirror configuration

Controlling the direction of radiation is basically an *antenna problem*, and hence it is useful to look at other antenna structures that have already been devised and discussed in literature. The first requirement is that the dimensions of the structure should be comparable to the wavelength of waves involved, which limits the size of antennas for the visible and near-infrared regions in the nanometer range. Before the advent of fabrication techniques for such dimensions, antennas were devised at the macro scale for longer wavelength waves, such as radio waves and microwaves, which still form the basis for microscopic designs.

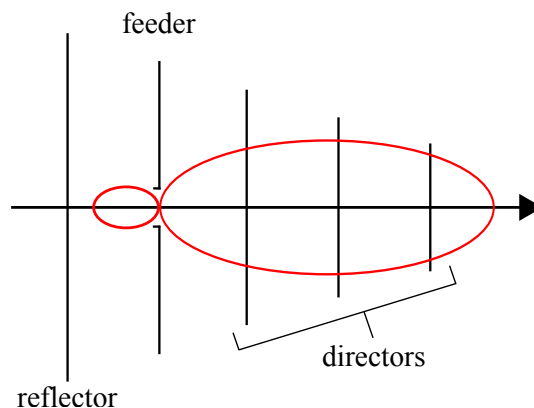


Figure 4.15: Yagi-Uda configuration.

Perhaps the most widely known is the Yagi-Uda design, which consists of different elements arranged in a linear fashion: the active source element is called the *feeder*, and other passive elements placed around the source are called *reflectors* and *directors* depending on their function [67]. Figure 4.15 illustrates the Yagi-Uda configuration. It consists of a single reflector on one side of the driven element and one or more directors on the other side. The feeder induces a current in the other passive elements and results in radiation that is unidirectional and coherent, with the main lobe along the axis perpendicular to the elements directed towards the directors. When the driver is a dipole oscillator, the induced dipole in the other elements can be described by the expression:

$$\vec{p} = \theta_i \left[\sum_{i \neq j} \mathbf{G}(\vec{r}_i - \vec{r}_j) \cdot \vec{p}_j + \mathbf{G}(\vec{r}) \cdot \vec{p}_0 \right] \quad (4.18)$$

where θ_i is the polarizability of the dipoles and the coupling between them takes place in free space as determined by the Green tensor [68]. The solution to the equation above gives us the amplitude and phase of the induced dipoles, and the final emission profile from the antenna can be figured out by substituting values in the following relations for the far-field $\vec{E}(\vec{r})$ and the Poynting vector $\vec{S}(\vec{r})$:

$$\begin{aligned} \vec{E}(\vec{r}) &= \frac{Z c k^2}{4 \pi} \frac{e^{ikr}}{r} \sum_i e^{-ik\hat{r} \cdot \vec{d}_i} (\hat{r} \wedge \vec{p}_i) \wedge \hat{r}, \\ \vec{S}(\vec{r}) &= \frac{Z c k^4}{32 \pi^2 r^2} \sum_{i,j} \text{Re} \left[e^{-ik\hat{r} \cdot (\vec{d}_i - \vec{d}_j)} \left(\vec{p}_i \cdot \vec{p}_j^* - (\hat{r} \wedge \vec{p}_i)(\hat{r} \wedge \vec{p}_j^*) \right) \right] \end{aligned} \quad (4.19)$$

In order to optimise the directionality of emission from the antenna, it is possible to tune the parameters given in these equations, such as polarizability θ_i and more simply the distances d_i between the elements which controls the phase relationship between them and hence can produce a constructive interference in the forward direction and destructive interference in the other.

Antennas for optical wavelengths based on the Yagi-Uda design have indeed been devised in recent years, in which a single quantum emitter has been coupled to the antenna elements in the near-field [69, 70]. Such antennas frequently use metallic reflector and director elements, and thus their complex frequency-dependent dielectric constants have to be taken into account alongwith the possibility of coupling to surface plasmons on the metal surface [71]. The resonance frequency for plasmonic nanoparticles are highly dependent on their geometrical structure [72] and can be tuned to respond to the wavelength of interest in the Yagi-Uda configuration [73].

Applying these concepts to the interference phenomena that take place between the dipole emitter and the induced reflected dipole in structures described in the previous section, it is possible to arrive at a Yagi-Uda configuration by adding a thin transmitting metal layer that acts as the director. The modified structure has been depicted in figure 4.16 and utilises the optimised structure for the one-mirror configuration with

the emitter-reflector distance fixed at $\lambda/4n$. For simplicity, the emitter is embedded in a single finite medium with $\text{RI}=1.5$. The samples are designed for observations by an objective through air, thus they can be tested if they are suitable for low numerical aperture optics.

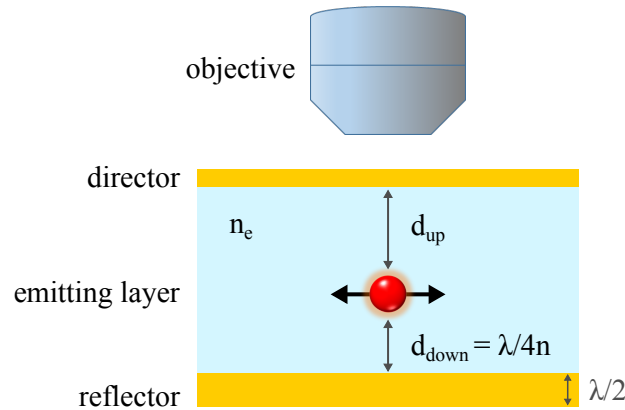


Figure 4.16: Double mirror configuration.

Tuning of the parameters related to the director is done to obtain a highly directional power transmission along the transverse axis towards the objective. First, the thickness of the director was optimised and then for each thickness, a scan of the distance between the emitter and the director was made. The thickness was varied between 1-50 nm, and then for each thickness first a coarse scan for emitter-director distance was made from 50-500 nm with intervals of 50 nm. After identifying favourable distance ranges for each thickness, finer scans on distance were made for the same. For example, figures 4.17 and 4.18 depict power density graphs as a function of polar angle θ for two fine scans on the emitter-director distance for a director thickness of 20 nm, in two interesting ranges around 50 nm and 300 nm which show increased angular confinement along the optical axis. As before, the emitter is taken to be oriented parallel to the interface with the emission wavelength at 785 nm.

It is immediately apparent that the second-range from 300–350 nm is more favourable, as it confines almost all the light within angles less than 45° , which corresponds to a numerical aperture of 0.7 which is comparable to NA of air-objectives typically used in labs. Table 4.1 enlists the best cases of emitter-director distances for thicknesses of the director varying from 1-50 nm to obtain a beam that is more directed along the optical axis towards the detector. For each of the cases mentioned in table 4.1, the emission power density as a function of angle θ from the z-axis and the collected power obtained for angular apertures β have been plotted in figure 4.19(a) and (b) respectively. It is seen that while an increase in director film thickness increases the directionality of the emission, it also reduces the amount of power transmitted outside the structure due to increased thickness of the gold layer. One needs to find an optimum between these cases by considering the power transmission and angular range of emission simultaneously.

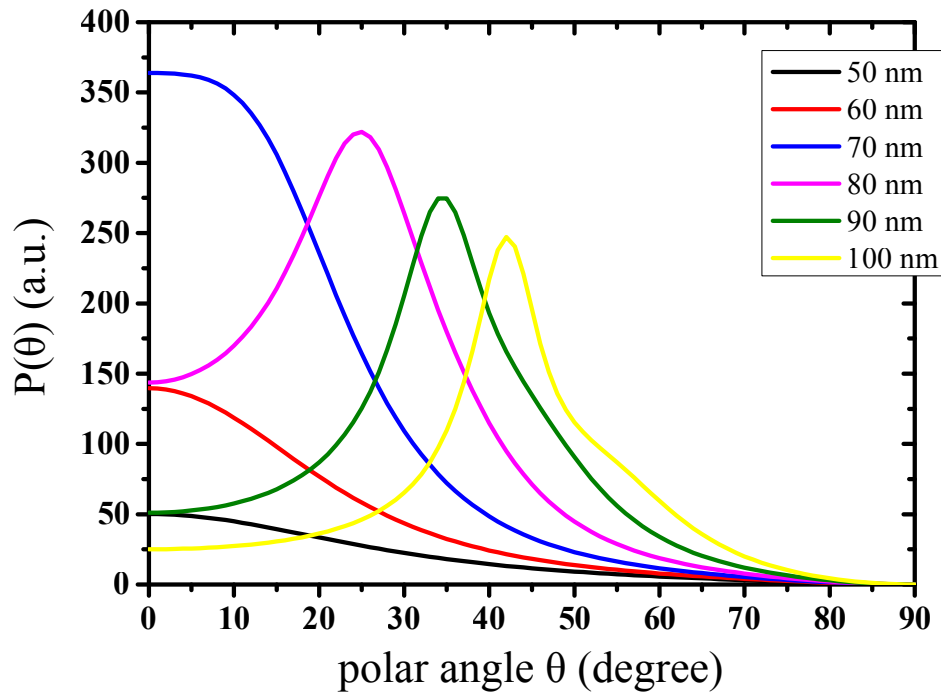


Figure 4.17: Variation of power density for polar angle θ with the distance of the emitter from the director scanned from 50-100 nm, for a fixed thickness of the director layer = 20 nm.

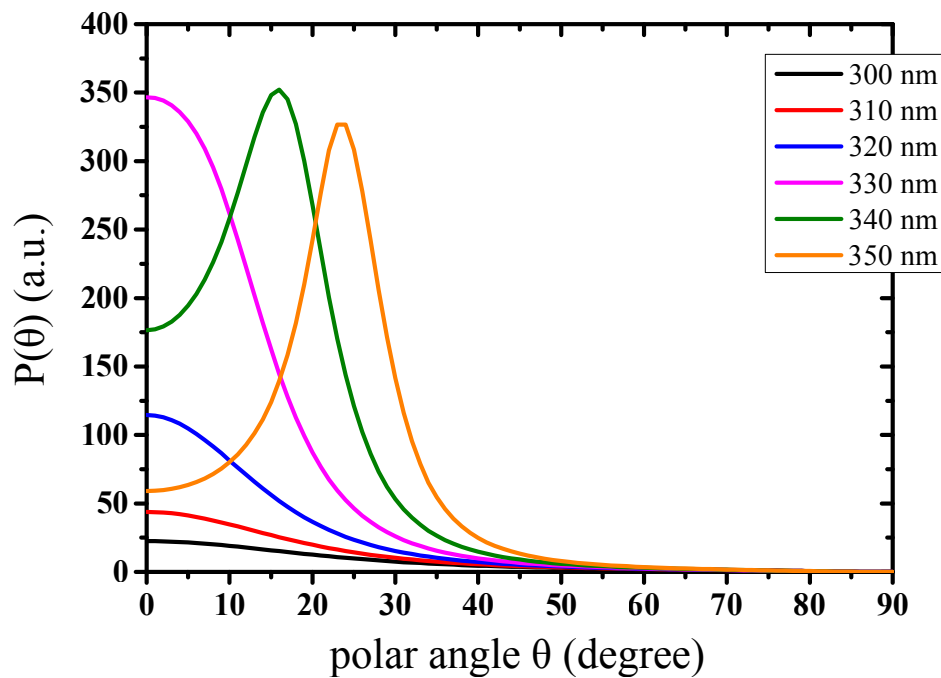


Figure 4.18: Variation of power density for polar angle θ with the distance of the emitter from the director scanned from 300-350 nm, for a fixed thickness of the director layer = 20 nm.

Director thickness	Emitter-director distance
$t_{dir} = 50$ nm	$d_{up} = 340$ nm
$t_{dir} = 40$ nm	$d_{up} = 340$ nm
$t_{dir} = 30$ nm	$d_{up} = 335$ nm
$t_{dir} = 20$ nm	$d_{up} = 330$ nm
$t_{dir} = 10$ nm	$d_{up} = 310$ nm
$t_{dir} = 5$ nm	$d_{up} = 300$ nm
$t_{dir} = 2.5$ nm	$d_{up} = 260$ nm
$t_{dir} = 1$ nm	$d_{up} = 250$ nm

Table 4.1: Optimal emitter-director distances for a given thickness of the director layer, which result in a narrow beam of radiation confined in small angles.

Experimentally as a first test, in a manner similar to the one-mirror design (described in subsection 4.3.1), the sample using the double-mirror was prepared by a top-down approach for the configuration depicted in figure 4.16. Since this approach makes the topmost semi-infinite layer to be the glass coverslip (instead of air), the oil objective was used to take measurements to avoid adding more interfaces. Simulations were modified and an optimal configuration was found with a director thickness of 20 nm with its distance from the emitting layer at 50 nm. Thus, for fabrication of the sample, first a 20 nm gold film (director) was deposited on a cover glass, followed by a 50 nm spacer layer of Hydrogen silsesquioxane (HSQ). HSQ is a commercially available inorganic polymer frequently used for high resolution lithographic processes and gets converted into silicon oxide upon irradiation with an e-beam or extreme-UV (XUV) source, which renders it to have a refractive index of 1.5. The one-mirror configuration is then built upon such a substrate, which involves the deposition of a 50 nm thick DBT:Ac emitting layer followed by a PVA spacer layer of thickness corresponding to $\lambda/4n$ where $n=1.5$. The sample is finished up by depositing a 100 nm thick gold layer serving as the reflector element.

Figure 4.20 shows the angular emission pattern from a single molecule embedded in a sample prepared with the double-mirror configuration. The emission profile clearly displays a distribution which is concentrated in a narrow range of angles around the center and can be referred to as *beam-forming* towards the objective.

To quantify the effect of such a multilayer structure, saturation curves were obtained for single DBT molecules in the double-mirror configuration as shown in figure 4.21. Very high count rates were measured, and the non-linear response of the APD had to be taken into account at such high count rates. It was found that the emitters situated inside the double-mirror configuration had a saturation intensity more than an order of magnitude less than those on the reference sample (figure 3.6). This is probably caused by enhanced excitation efficiencies due to similar mechanisms that enhance the collection efficiencies.

Additionally, in order to verify that the resultant narrow mode distribution is mainly due to the redistribution of intensities in space and not due to the to enhancement/suppression of particular density of states in which emission can take place, it is appropriate

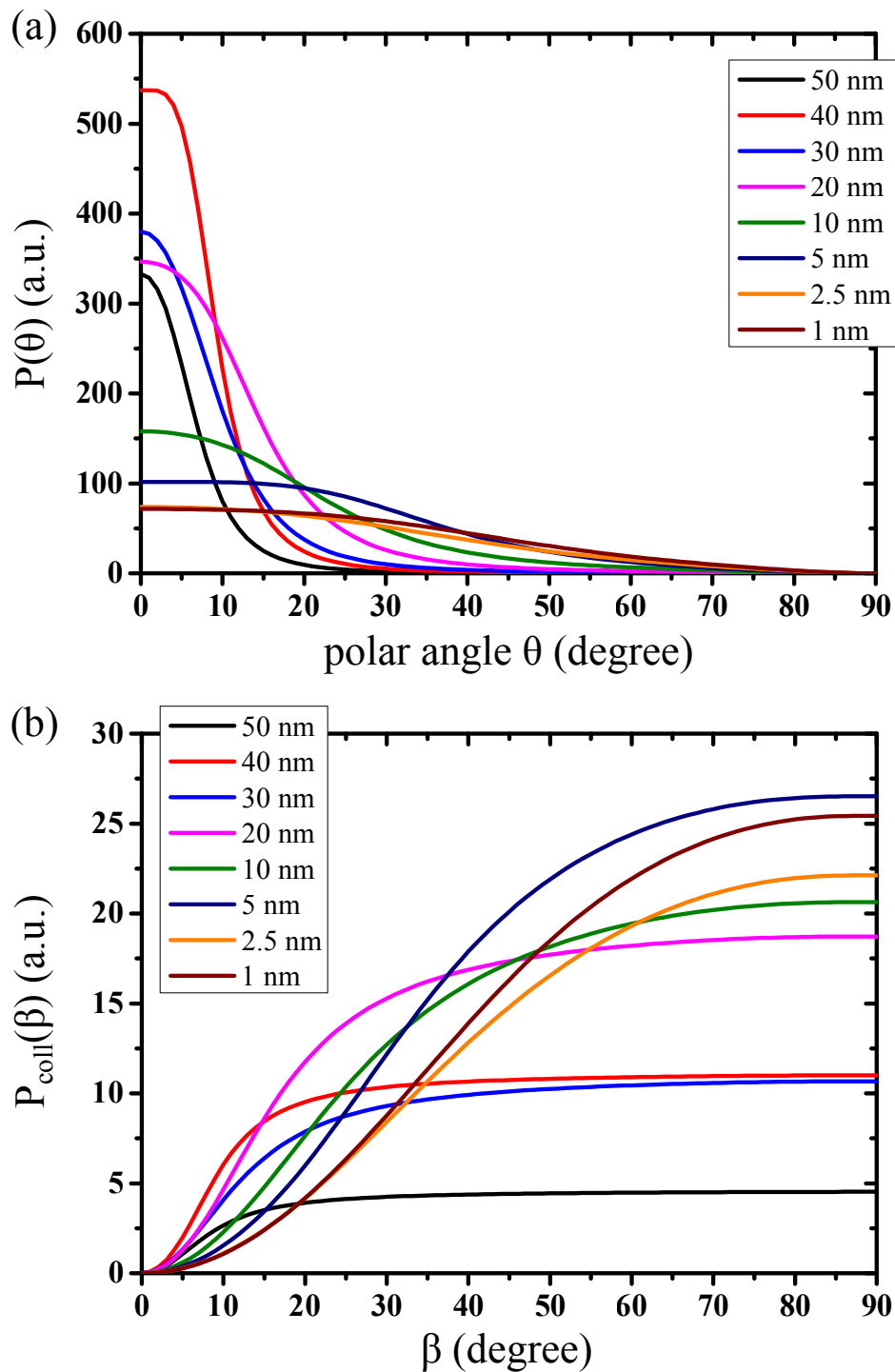


Figure 4.19: (a) Power as a function of polar angle θ for the optimal emitter-director distances for given thicknesses of the director layer that are listed in the legend, and correspond to values given in table 4.1. (b) Power collected in angular apertures from 0 to β for the same cases. An increase in director film thickness increases the directionality of the emission beam, but decreases the power collected by the objective.

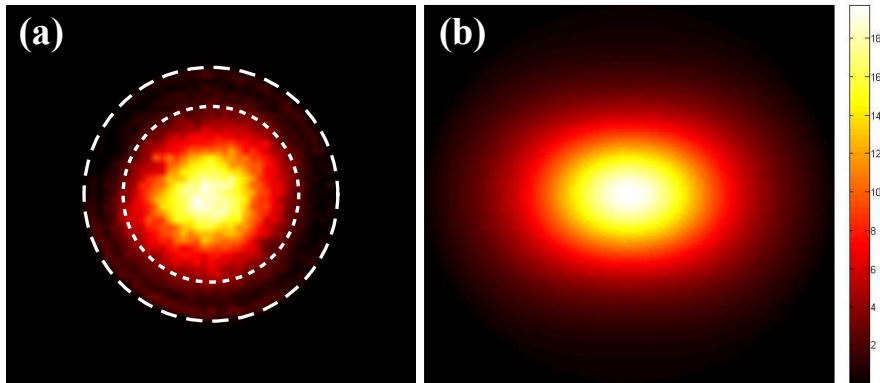


Figure 4.20: (a) Experimental and (b) Simulated angular emission pattern for a Double-mirror configuration (Figure 4.16): the emitter is embedded in an emitting layer of $n=1.5$, where the distance of the emitter from the reflector is $d_{\text{down}} = \lambda/4n$ and the distance from the director $d_{\text{up}} = 50 \text{ nm}$. The inner dashed circle corresponds to the critical angle and the outer circle corresponds to the maximum angle collected by the objective.

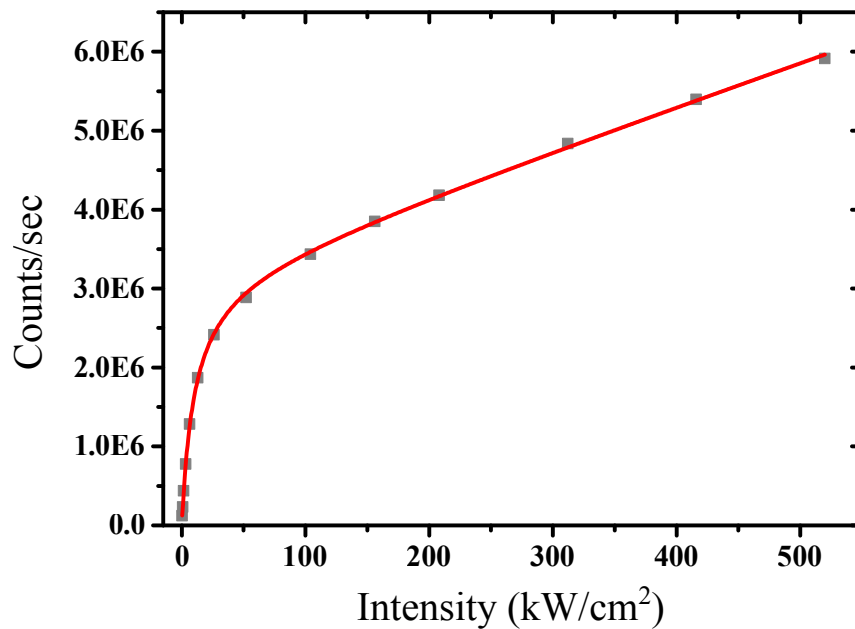


Figure 4.21: Detected rates obtained as a function of excitation intensity for DBT molecules embedded in the double mirror configuration. The background signal has not been subtracted and its linear behaviour is clearly evident at higher excitation intensities.

to calculate the Purcell factor $F_p = \Gamma_{struc}/\Gamma_0$ of the multilayer structure by comparing the radiative decay rates of molecules inside the structure Γ_{struc} to decay rates in a reference configuration. For this, lifetimes were measured for the DBT molecules in the double-mirror configuration and it was found that their distribution is Gaussian centered around 3.9 ns with a standard deviation of 0.43 ns. This shows only a slight decrease in lifetime when compared to the lifetimes obtained for a reference sample with a nominal value of 4.2 ± 0.4 ns (figure 6.6(a)), and renders the Purcell factor close to 1.

4.4 Outlook

Despite the enormous progress in design and fabrication of photonic devices in the last decades, light collection efficiencies from single emitters in tiny sensing volumes can still use some improvement, specially in the optical regime. Several antenna designs have been proposed to direct light from light sources: microcavities [74, 75], photonic nanowires [76, 77], metallic nanoantennas [69, 70], planar antennas [78], hybrid patch antennas [79], etc. However, a majority of these make use of either advanced lithographic techniques for fabrication of the devices or high NA optics for the collection of emitted radiation.

The planar optical antennas presented in this work have been designed and verified for remarkable low-angle collection efficiencies from single emitters without the need for a complicated setup or fabrication procedures, and utilise cost-effective and simple procedures for deposition of thin films such as spin coating and metal-sputtering. These planar antennas are robust and flexible to accomodate a wide variety of layer materials and are tunable in a wide range of operating wavelengths by simple thickness modifications. More importantly, this work has led to the development of optical antennas that can confine dipolar emission in low angles around the optical axis, which can be efficiently collected by low NA optics such as optical fibers. In fact, high collection efficiencies from single photon sources would be beneficial in a wide range of applications including quantum computing protocols, opto-electronic chip components, biosensors, solid-state lighting, and so on.

5 Coupling to surface plasmons

By moving an emitter closer to the metal interface at distances $d < \lambda$, as described in section 1.4, the interface is considered to be in the near-field of the source and has an access to a larger range of spatial frequencies (k_x, k_y) of the emission. Part of this spectrum with $(k_x^2 + k_y^2) > k^2$ is associated with evanescent waves and can couple to modes on the surface of the metal, resulting in charge density oscillations on the metal surface called surface plasmons. When light interacts with the free electrons (the plasma) on the surface of a metal, it can yield a hybrid light-electron oscillating mode called surface plasmon polariton (SPP)¹. SPPs are part of the wider class of surface modes where the interaction between light and matter leads to the possibility of a bound surface mode, which includes surface phonon polaritons [80] and surface exciton polaritons [81].

This chapter gives an introduction to the fundamental SPP properties followed by a discussion on the methods to excite SPPs on a metal surface. Keeping in mind these methods, three configurations were explored during this thesis work to observe coupling to plasmons: a flat metal surface, metallic concentric-ring resonators, and metal waveguides. The first configuration was used to observe coupling between emitters and surface plasmons, while the other two are a work in progress. Ring resonators enable higher confinement in localized plasmon polaritons, associated to geometrical resonances determined by the object shape. They have been studied to easily and reliably observe single molecule SERS (surface enhanced Raman scattering) making use of the Purcell enhancement delivered by subwavelength localized plasmon modes. Finally, 1-D plasmonic waveguides can support highly confined longitudinal plasmonic modes with long propagation lengths, and have the potential to enable long-range intermolecular coupling through surface plasmons [82]. The metal used is gold for its stability and response at the wavelengths of interest (i.e. centered around 785 nm for Dibenzoterrylene (DBT) dye molecules).

5.1 Introduction

5.1.1 Properties of surface plasmon polaritons

Consider a plane interface between two media as shown in Figure 5.1. One medium is characterised by a general, complex frequency-dependent dielectric function $\epsilon_1(\omega)$

¹Higher energy light can also excite bulk (volume) plasmons away from the metallic surface.

whereas the dielectric function of the other medium is $\epsilon_2(\omega)$ is assumed to be real for simplicity. Propagating SPP charge fluctuations can be described by a mixed transverse and longitudinal electromagnetic field which disappears at $|z| \rightarrow \infty$ and has a maximum directly at the interface $z = 0$ (Figure 5.1) [83]. If we consider the propagation direction

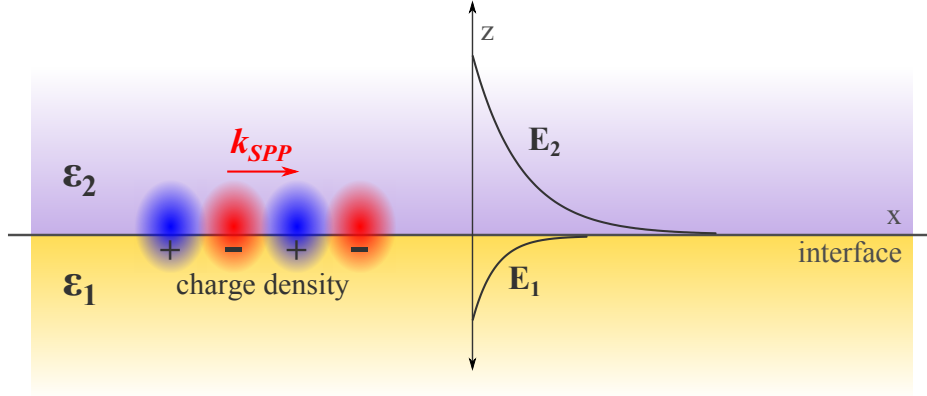


Figure 5.1: SPP field distributions.

along the x -axis, the field is expressed by:

$$E_j^{tot} = E_j e^{i(k_x x \pm k_z z - \omega t)}, \quad j = 1, 2 \quad (5.1)$$

where $+$ is used for medium 2 ($z \geq 0$) and $-$ for medium 1 ($z \leq 0$). Both wavevector components k_x and k_z are assumed to be complex valued.

The dispersion relation, i.e. the relation between the in-plane wavevector and the angular frequency ω , is obtained by solving Maxwell's equations under appropriate boundary conditions [84]:

$$k_x = \frac{\omega}{c} \sqrt{\frac{\epsilon_1 \epsilon_2}{\epsilon_1 + \epsilon_2}} \quad (5.2)$$

The out-of-plane wavevector k_z is given by:

$$k_{j,z} = \frac{\omega}{c} \sqrt{\frac{\epsilon_j^2}{\epsilon_1 + \epsilon_2}}, \quad j = 1, 2 \quad (5.3)$$

In order to represent a surface bound wave, it is required that the normal components of the wavevector are purely imaginary in both media, which indicates that the denominator in equation 5.3 is negative. Additionally for propagating waves in the x -direction, k_x needs to be real in equation 5.2, and therefore the sum and product of ϵ_1 and ϵ_2 are either both positive or both negative. Combining these conditions, we get:

$$\epsilon_1(\omega)\epsilon_2(\omega) < 0 \quad \text{and} \quad \epsilon_1(\omega) + \epsilon_2(\omega) < 0$$

which means that one of the dielectric functions must be negative with an absolute value exceeding that of the other. This perfectly matches with the case of an interface

between a metal such as gold or silver, and a dielectric such as air or water, since metals have a dielectric function composed of a large negative real part and a small imaginary part. This indicates that propagating surface modes can indeed exist at such an interface.

If we assume medium 1 to be a metal as described by the Drude model and medium 2 to be a non-absorbing dielectric, then equations 5.2 and 5.3 define the propagation of SPPs along the interface. The in-plane wavevector thus obtained by equation 5.2 is complex, $k_x = k'_x + ik''_x$ – the real part governs the propagation of the SPP while the imaginary part describes damping of the plasmon as it propagates, due to ohmic losses in the metal. The *propagation length* of the plasmon is defined as the distance after which the SPP field decays to $1/e$ of its initial amplitude and is given by $L_{\text{SPP}} \simeq (k''_x)^{-1}$. However, in experiments intensities are measured (rather than fields), and hence the propagation length is often described as $L_{\text{SPP}} \simeq (2k''_x)^{-1}$, referring to the decay of intensity to $1/e$ of its initial value.

Since the normal component of the wavevector k_z is purely imaginary, it determines the extension of the evanescent field into the two half spaces. Similar to the one defined for k_x , the parameter *skin depth* denotes the distance after which the transverse field decays to $1/e$ of its initial value in each medium and is given by $\delta_j = (k_{j,z})^{-1}$ for $j = 1, 2$ (indices for each medium). Using equation 5.3, it is easy to see that δ_{metal} is a lot less than $\delta_{\text{dielectric}}$. These values are useful in deciding experimental parameters, for example the thickness of metal to be used and distance of approach for a near field probe.

Due to its surface-bound nature, the excitation of SPPs results in an intensity enhancement near the interface [85]. This property has been exploited in numerous experiments to observe increased light-matter interaction through: Fluorescence spectroscopy [86], surface-enhanced Raman Spectroscopy (SERS) [87], bio-sensing [88], just to name a few.

Figure 5.2 shows the dispersion relation, i.e. the relation between momentum in terms of the in-plane wavevector and the energy in terms of angular frequency, for a gold-air interface calculated according to equation 5.2, using dielectric constant values provided by Johnson and Christy [89]. As the lower branch of the dispersion curve approaches the resonance condition (here $\omega = \omega_p/\sqrt{2}$, where ω_p is the plasma-oscillation frequency), it bends when the losses in the metal start to increase drastically. Consequently when ω is further increased, the dispersion curve bends back and connects to the upper branch [90]. This upper branch is considered to be non-physical as the normal component of the wavevector k_z given by equation 5.3 is no longer purely imaginary in this case. Note that this relation is derived from the simplistic Drude model, while a more realistic model includes the effect of interband transitions of bound electrons [84].

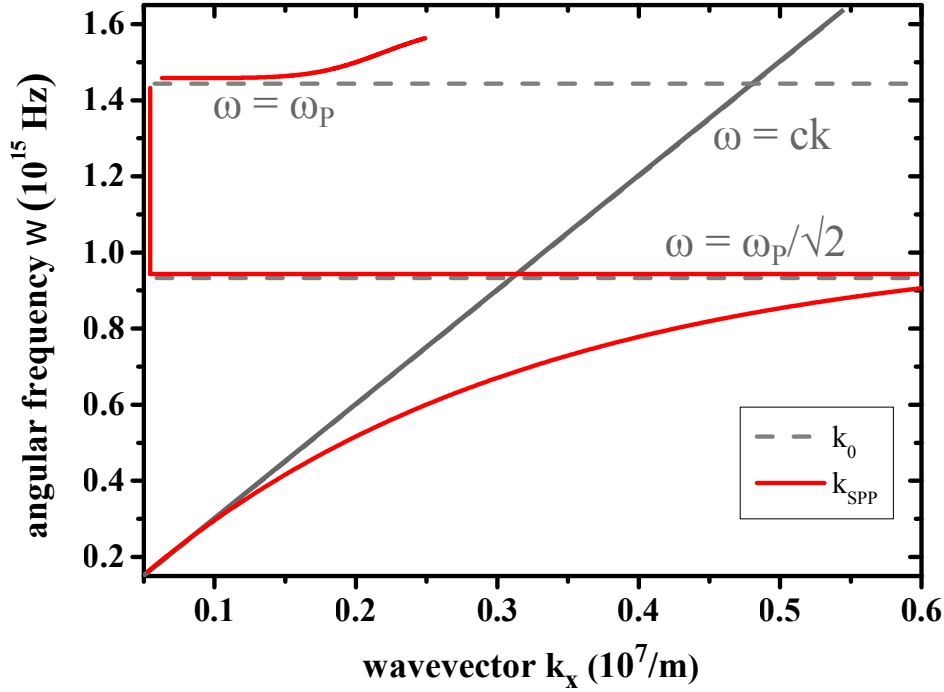


Figure 5.2: Dispersion relation of gold calculated by equation 5.2. The horizontal dashed lines represent the resonance conditions for the lower and upper polariton branches and the solid gray line represents the light line $\omega = ck$.

5.1.2 SPP excitation

The dispersion relation shown in figure 5.2 also indicates the dispersion relation of light in free space called the light line. The light line represents the cone of angles beyond which the light can be considered evanescent. The light line approaches the SPP dispersion asymptotically at low ω but never intersects it. As a consequence, it's not possible to excite plasmons unless they *match the higher momentum of the plasmon* for the same frequency. Several schemes have been proposed to achieve this: by prism coupling [47], grating coupling [91], near-field coupling [92] and non-linear coupling [93]. Figure 5.3 shows some of the schemes to excite surface plasmons.

The Otto and Kretschmann configurations for excitation of plasmons make use of the fact that plane waves travelling in a denser medium have a higher wavevector proportional to its higher refractive index. Thus it is possible to match the momentum required to launch plasmons on the metal surface, by putting the metal layer in between dielectric media with different refractive indices (say $\epsilon_{glass} > \epsilon_d$), as shown in figures 5.3(a) and (b). This can be achieved by sending a light beam through the higher-index material at an angle beyond the critical angle, which can result in plasmon propagation at the interface of the metal with the lower-index material. Since the excitation field is evanescent, in figure (a), plasmons are launched when the metal film is brought within the interaction distance, and in figure (b), the thickness of the metal needs to be thin

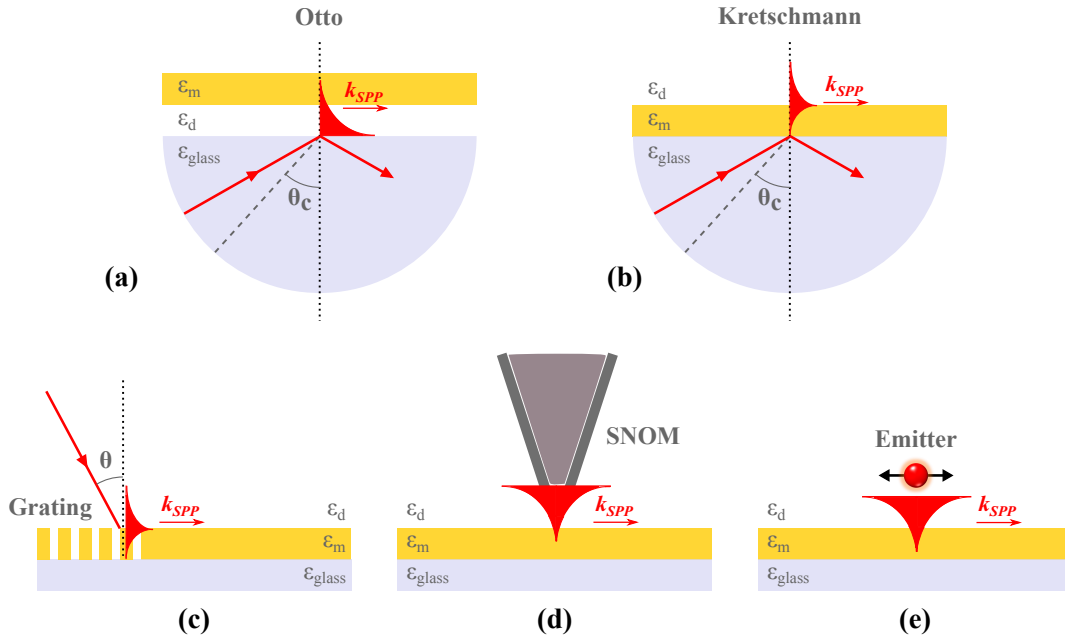


Figure 5.3: SPP excitation schemes: (a) Otto configuration (b) Kretschmann configuration (c) Excitation using a grating (d) Excitation by a SNOM probe (e) Excitation by fluorescent emitters.

enough for the field to reach through it to the other interface. The resonance condition is manifested as a dip in the spectrum of the totally-reflected light, and different reflection curves with different resonant beam wavelengths can be obtained by changing the angle of incidence of the impinging beam.

Other methods shown in figure 5.3 refer to grating coupling and near-field coupling. As shown in figure (c), the metal is patterned in shape of a grating, and thus the condition to match the SPP-wavevector is achieved by adding an additional wavevector component related to the grating, given by:

$$k_{SPP} = \left(\frac{2\pi}{\lambda} \right) n_d \sin \theta + m \frac{2\pi}{g} \quad (5.4)$$

where the n_d is the refractive index of the dielectric. Suitable values for the angle of incidence θ , the lattice constant g and order of refraction m for each excitation wavelength λ are utilised in order to achieve the resonance condition for the SPP [94].

Near-field coupling to plasmons involves directly bringing the excitation sources in the near-field since, as discussed before in section 1.4, in the near-field of the source, there is a larger range of available wavevectors, some of which can match the SPP wavevector. Figures 5.3(d) and (e) illustrate two such methods, namely: excitation by approaching with a SNOM tip (with a subwavelength aperture for illumination), and by putting microscopic emitters (atoms, molecules, quantum dots) near a metal interface. Again due to evanescent nature of the fields, the strength of the coupling

increases with decreasing distance of the emitter from the metal surface. However at very low distances ($d < 20$ nm), other non-radiative channels open up and hamper the SPP-coupling efficiency.

In this thesis, prism coupling and near-field coupling have been used in tandem for the excitation of SPPs over gold. Prism coupling setup has been described in section 2.3.2, where the evanescent field produced due to total internal reflection inside a glass prism has the required k-vectors to match the SPP k-vector at the gold-air interface, and hence is able to excite surface plasmons. Out of the methods that exploit this coupling

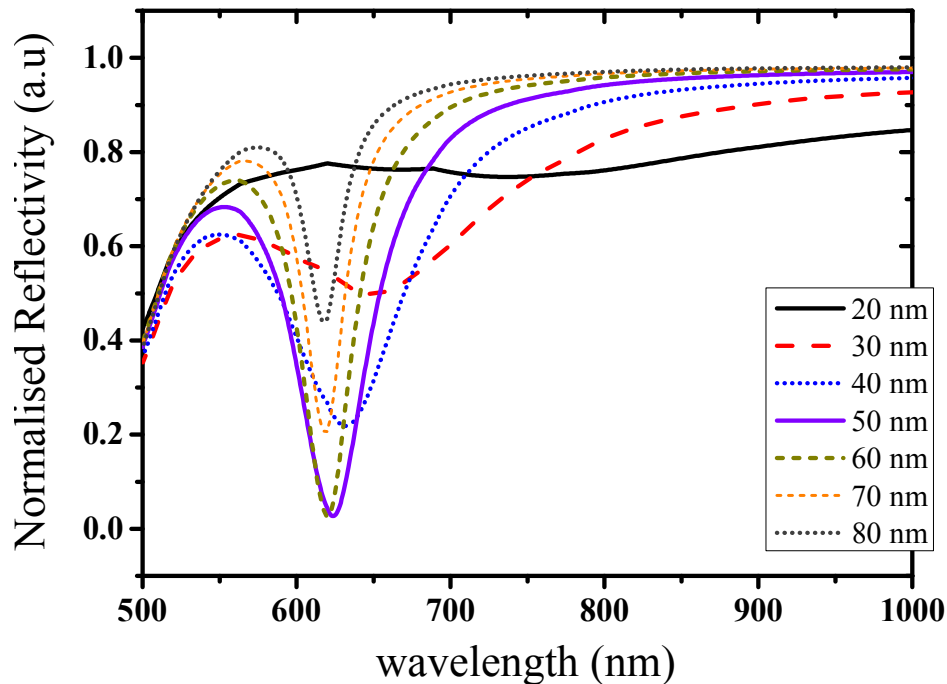


Figure 5.4: Simulation demonstrating the evolution of the dip in reflectivity with thickness of the metal.

mechanism, Otto and Kretschmann, the Kretschmann configuration was chosen due to its ease of implementation compared to the other. However, care has to be taken while choosing the thickness of the metal for such experiments because of the fast exponential decay of the field inside the metal space. If the metal is too thin, the SPP will be strongly damped due to radiation damping into the glass². If the metal is too thick, the SPP can no longer be efficiently excited due to absorption in the metal. Figure 5.4 shows the evolution of the SPP dip with thickness of the metal obtained by simulations.

If fluorescent emitters are placed in the near-field of the metal interface used in the Kretschmann configuration, it is possible to couple the emitters to the plasmonic field generated by prism coupling. For a common plasmonic field, this can lead to

²Radiation damping is the process of conversion of plasmon energy into photons, which propagate mainly inside the glass medium.

coherence between different coupled emitters where inter-emitter energy transfer can become possible [95]. Naturally, the range of such coupling is limited by the field propagation length of the plasmon given by $L_{\text{SPP}} \simeq (k_x'')^{-1}$, due to dissipations in the metal, but is still very large compared to the typical range of dipole-dipole radiative energy transfer which is a few nm. Moreover, when the strength of the coupling between the emitter and the plasmon exceeds the total amount of losses of the combined system, the interaction is said to be in the *strong coupling regime* and leads to quantum coherent oscillations between the two coupled systems with spatial coherence over large distances [96]. Strong coupling is discussed in the next section.

5.2 Crossing over from weak coupling to strong coupling

To understand the physics of the interaction between emitters and surface plasmons, it is beneficial to use a fully quantum description for its clarity. Moreover, even though a semi-classical basis is adequate for systems encountered in this thesis, it seems to break down for deep-subwavelength plasmonic structures such as nanogaps between metal nanoparticles [97]. The following discussion borrows from cavity QED equations which describe the interaction of a quantum system with a cavity field.

For a single quantum emitter with a transition frequency ω_0 , the Hamiltonian is given by:

$$\hat{H}_0 = \hbar\omega_0\hat{\sigma}^\dagger\hat{\sigma} \quad (5.5)$$

where $\hat{\sigma}^\dagger = \rho_{eg}$ and $\hat{\sigma} = \rho_{ge}$ are the raising and lowering operators for the emitter. The SPP-field comprises of a continuum of modes and the Hamiltonian describing the quantized SPP-field can be written as a summation over all in-plane k-vectors [98]:

$$\hat{H}_{\text{SPP}} = \sum_k \hbar\omega(k) \hat{a}_k^\dagger\hat{a}_k \quad (5.6)$$

for \hat{a}^\dagger and \hat{a} denoting the bosonic creation and annihilation operators for plasmons. Thus the Hamiltonian for a quantized field interacting with a two-level system is given by equation:

$$\begin{aligned} \hat{H} &= \hat{H}_0 + \hat{H}_{\text{SPP}} + \hat{H}_{\text{int}} \\ \hat{H} &= \hbar\omega_0\hat{\sigma}^\dagger\hat{\sigma} + \sum_k \hbar\omega(k) \hat{a}_k^\dagger\hat{a}_k + \sum_k \hbar g(\hat{a}_k\hat{\sigma}^\dagger + \hat{a}_k^\dagger\hat{\sigma} + h.c.) \end{aligned} \quad (5.7)$$

This is the generic form of the so-called *Jaynes-Cummings Hamiltonian* where g denotes the coupling parameter between the two modes and is proportional to the dipole moment of the quantum emitter. Here we assume uniform coupling strength across all the modes such that g is independent of wavevector k .

For the case of total N coupled emitters, where N is large but the number of excited emitters is small (i.e. the low excitation regime), the raising and lowering operators $\hat{\sigma}^\dagger$

and $\hat{\sigma}$ for the quantum emitter can be replaced by bosonic operators \hat{b}^\dagger and \hat{b} respectively, using the Holstein-Primakoff transformation [99]. The resultant Hamiltonian then becomes:

$$\hat{H}^N = \sum_N \hbar\omega_0 \hat{b}^\dagger \hat{b} + \sum_k \hbar\omega(k) \hat{a}_k^\dagger \hat{a}_k + \sum_k \sum_N \hbar g (\hat{a}_k \hat{b}^\dagger + \hat{a}_k^\dagger \hat{b} + h.c.) \quad (5.8)$$

This equation, however, does not contain the decoherence terms accounting for the losses of the coupled system. These losses can be due to the radiative decay of the emitter excited state represented by rate γ_e which is the average value of the decay rate of many emitters; decay of the plasmon due to dissipation in the metal with a rate $\gamma_{SPP} = v_g/L_{SPP}$ where v_g and L_{SPP} is the group velocity and propagation length of the plasmon mode respectively; and pure dephasing mechanisms (for example phonon-coupling in solid state systems) with a rate γ_d . These losses can be accounted in the form of Lindblad terms in the master equation for the system dynamics:

$$\frac{d}{dt} \hat{\rho}_k = \frac{i}{\hbar} [\hat{\rho}_k, \hat{H}^N + \hat{H}^{\mathcal{L}}] + \frac{\gamma_e}{2} \mathcal{L}_e + \frac{\gamma_{SPP}}{2} \mathcal{L}_{SPP} + \frac{\gamma_d}{2} \mathcal{L}_d \quad (5.9)$$

This is the *Markovian-Lindblad* master equation [100]. The solution of this equation for $k_0 = k(\omega_0)$, i.e. the in-plane momentum for maximum coupling, is given by

$$R = 2\sqrt{g^2 - (\gamma_e + \gamma_d - \gamma_{SPP})^2/16} \quad (5.10)$$

where R is referred to as *Rabi splitting* and its magnitude indicates the regime of coupling (i.e. weak or strong) between the two modes. The mixed emitter-plasmon states thus created are called *dressed states*.

In the absence of dephasing mechanisms (or $g \gg \gamma_e, \gamma_{SPP}, \gamma_d$), the Rabi splitting R corresponds to the interaction term, i.e. $\Delta E = |\mu_{ge} \cdot E_{SPP}(k)|$. Note that due to the dot product in the expression for ΔE , the consideration of the orientation of the dipole moment is important and in fact, it is known that perpendicular dipoles have a much higher coupling efficiency to surface plasmons than parallel ones [98]. The Jaynes-Cummings model can be adapted to the case of N two-level systems interacting with the single-mode field of a resonant cavity and then it is referred to as the Tavis-Cummings Hamiltonian. In this case the Rabi splitting scales as the square root of N [8]:

$$\Delta E = 2\hbar g = \sqrt{N} \left(\frac{2\mu_{ge}^2 \hbar\omega_0}{\epsilon_0 V} \right)^{1/2} \quad (5.11)$$

The equation above can also be used to describe emitter-SPP coupling when the emitters are within the effective mode volume V of the plasmonic field³, and enables us to de-

³Here the calculation of the mode volume is non-trivial due to the dissipative nature of SPP modes [98, 101]

fine coupling regimes according to the magnitude of coupling constant ($g \propto \mu_{ge} \sqrt{N/V}$) as compared to the losses of the system.

If ($g \ll$ losses), the energy is lost irreversibly to the environment and we are in the weak coupling regime. There is negligible change in the individual energies and it's possible to treat the coupling by perturbation theory. When ($g \gg$ losses), we are in the strong coupling regime where the excitation is delocalized and the coupled system oscillates coherently with a Rabi frequency given by R (equation 5.10).

Thus the value of g is a good order-of-magnitude estimate in order to observe strong coupling in experiments but exact numbers can be extracted only after all microscopic details about the specific system have been considered. Note that this value of g calculated by equation 5.11 considers vacuum as the emitting medium and so ϵ_0 should be replaced by $\epsilon_{med} = \epsilon_r \epsilon_0$ for emitters embedded in a different dielectric medium.

5.3 DBT molecules on a flat gold surface

The simplest system to observe coupling between quantum emitters and surface plasmons, as described by equation 5.7, is the one where the emitter is placed in the vicinity of a planar surface. A simple sample configuration was used to this end: a planar gold film was deposited by sputter-coating on a glass coverslip, following which the emitting layer containing DBT molecules was spin coated on top. This has been illustrated in figure 5.5. Here in this section we will discuss various techniques to experimentally observe the coupling of emitters to surface plasmons.

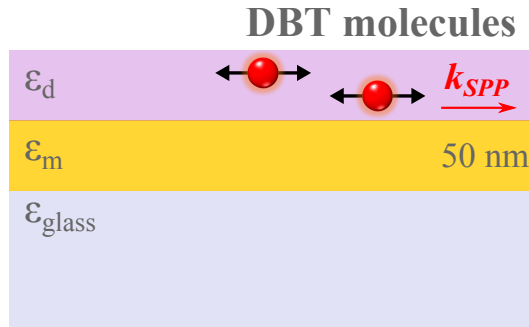


Figure 5.5: Sample schematic for coupling of DBT dye molecules to a planar gold film. The molecules are embedded in a non-absorbing medium with a permittivity ϵ_d .

Surface plasmon coupled emission (SPCE)

In general, light that is coupled into the SPP mode can couple back out by the same process, but the (phase) properties of the out-coupled light are different from the in-coupled light. A common way to detect coupling to plasmons is to observe the *leakage radiation* i.e. the light out-coupled into say, the glass half-space at angles greater than

the critical angle, due to radiation damping of the plasmon. The out-coupling into super-critical angles in glass can be understood as an overall bias of energy flow towards the glass rather than air due to wavevector matching [102]. The resultant emission is referred to as *surface plasmon coupled emission* (SPCE). If emitters are used to excite plasmons, SPCE depends on the interaction of the excited emitters with the metal surface, but is independent of the mode of excitation such that it does not necessarily require excitation of the emitter by an evanescent wave or surface plasmons, since as discussed before in section 5.1.2, sources in the near-field already have the required wavevectors for phase matching with SPPs. An analytical account for the properties of SPCE is given in [103] and a review of experimental studies is presented in [104, 105].

The fundamental property of SPCE is that it is centered around the SP-angle given by the resonance condition:

$$k_{SPP} = \left(\frac{2\pi}{\lambda} \right) n_d \sin \theta_{SPP} \quad (5.12)$$

where n_d is the refractive index of the dielectric in which SPCE occurs. θ_{SPP} is essentially greater than θ_c (critical angle) and the emission is symmetric in azimuthal angles ϕ around the optical axis for purely perpendicular or parallel dipoles. The radius in k-space corresponds to a real angle in 3-D space, and is related to the wavelength of emission according to the relation 5.12, with longer wavelengths with a smaller radius than shorter wavelengths. Secondly, SPCE is highly polarized i.e. it will be p-polarized (TM) at all angles in the emission cone, independent of the mode of excitation. Since only TM-polarized components can excite plasmons [48], it is indeed natural that the out-coupled light is also TM-polarised.

The model discussed in Chapter 4 to simulate angular emission patterns of dipoles embedded in a given multilayer structure also takes into account the absorption by the metal and can be used to simulate SPCE. Figure 5.6 shows the comparison of the simulated and observed angular emission patterns of DBT molecules embedded in anthracene over a gold layer, compared to the emission of the molecules on a reference sample (DBT molecules on glass). The signal from the reference sample is peaked directly above the critical angle for a glass-air interface, while the SPCE from emitters over the gold film has a peak at the surface plasmon angle given by equation 5.12, because of the back-conversion of higher-momentum plasmons into photons by radiation damping. Here, the orientation of the emitters is considered parallel to the sample plane. Note how the polarization (TM or TE) of emission changes between SPCE and reference simulations for the same emitter configuration. The experimental patterns are obtained at different points on different samples, so it is difficult to directly compare their polarizations. However, the assigned polarizations are indicated in the respective figures.

The experimental emission patterns were collected by using the back focal plane imaging setup in confocal configuration (refer section 2.3.1), where the excitation and

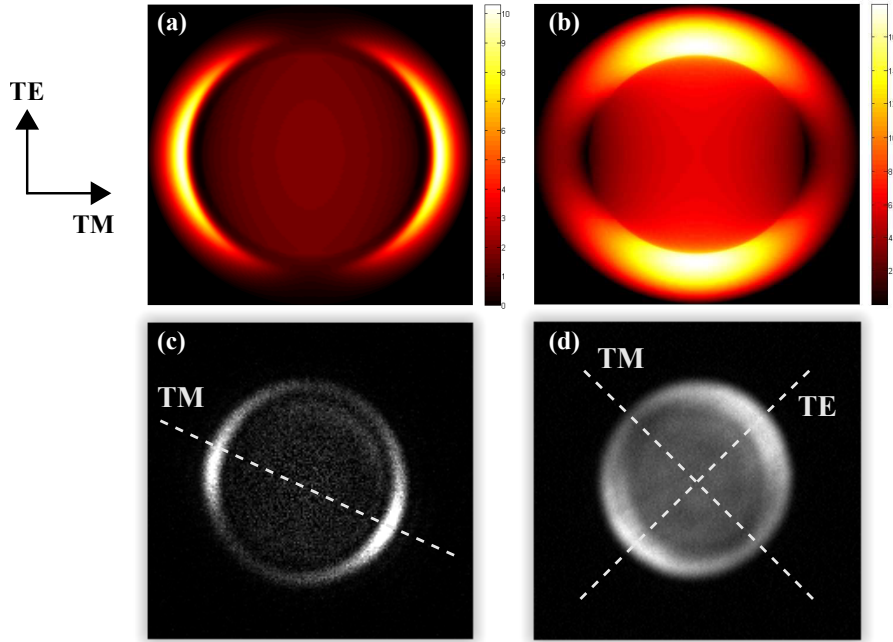


Figure 5.6: SPCE due to coupling of DBT molecules to plasmons in gold. (a) and (b) are simulated versions of angular emission for DBT molecules on gold and DBT molecules on a reference glass coverslip, respectively. It is evident that polarization changes for the same emitter configuration. (c) and (d) are experimental patterns corresponding to (a) and (b) respectively. The emission from the reference sample is peaked at the critical angle, while SPCE has a peak at the plasmon angle θ_{SPP} given by equation 5.12.

collection of radiation is done via the same objective lens. For this reason and the fact that the surface plasmon modes of a thick metal cannot emit into the dielectric due to dissipation in the metal, a thinner gold film was utilised, as compared to the optimal thickness obtained by simulations shown in figure 5.4. This makes the resonance broader and that is evident in the observed emission patterns, which is otherwise very narrowly distributed (in angles) for optimal thickness of the metal. However, we have a qualitatively good agreement which verifies that surface plasmons are launched by the quantum emitters.

Lifetimes

Coupling to SPs opens up a new channel for the decay of the excited state of an emitter, thereby modifying its decay rate according to the Fermi's golden rule, and is given by:

$$\tau = \frac{1}{\gamma_{spont} + \gamma_{SPP}} \quad (5.13)$$

We observed lifetimes of DBT molecules over gold, and compared them to the lifetimes obtained for the reference sample (reference sample figure 6.6(a)), and their distribution

has been plotted in figure 5.7. It shows a distribution peaked at about 3.1 ns which is less than the lifetimes on a reference sample centered at 4.2 ns.

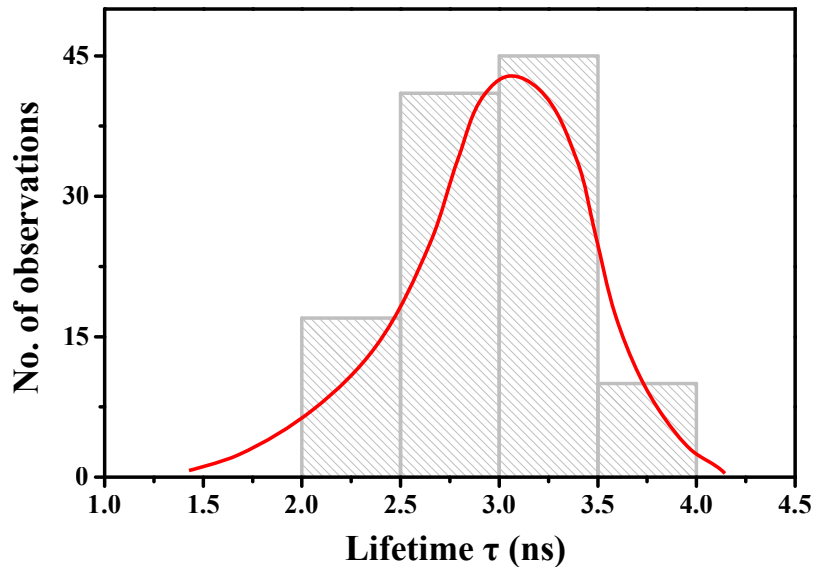


Figure 5.7: Distribution of lifetimes of DBT molecules embedded in anthracene spin coated over a planar gold surface. The red curve is a guideline with a peak value of 3.1 ± 0.43 ns.

The coupling efficiency to plasmons can be calculated as:

$$\eta = 1 - \frac{\tau_{\text{SPP}}}{\tau_0} \quad (5.14)$$

A maximum coupling efficiency of 45.2% was obtained corresponding to a lifetime of 2.3 ns.

Attenuated Total Reflection (ATR) method

As discussed in section 5.1.2, one way to excite plasmons is to use the Kretschmann configuration. Light is incident through a material of higher refractive index in order to match the SPP wavevector and the excitation of plasmons is indicated by the dip in reflection at the wavelength of resonance given by equation 5.12. The Kretschmann setup used in this work for measuring ATR curves has been described earlier in section 2.3.2.

The samples used for ATR measurements were akin to the one shown in figure 5.5, with fluorescent DBT molecules embedded in a non-absorbing dielectric medium, spin coated in thin layers over a gold film of 50 nm. Due to the field enhancement at the surface, SPPs are very sensitive towards the properties of their immediate environment, and therefore the effect of different dielectrics on the dispersion relation needs to be considered. Figure 5.8 shows the variation of the dispersion relation for two different thickness of the two dielectrics used for the emitting medium, namely PMMA and

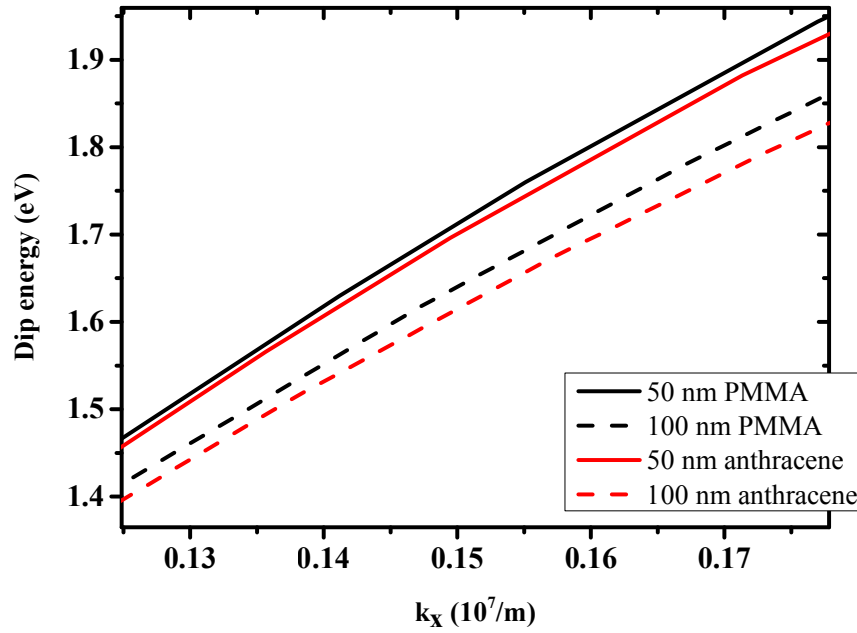


Figure 5.8: Simulated dispersion relation for PMMA (black) and anthracene (red) as the emitter media over a 50 nm gold film, with thicknesses equal to 50 and 100 nm for each case.

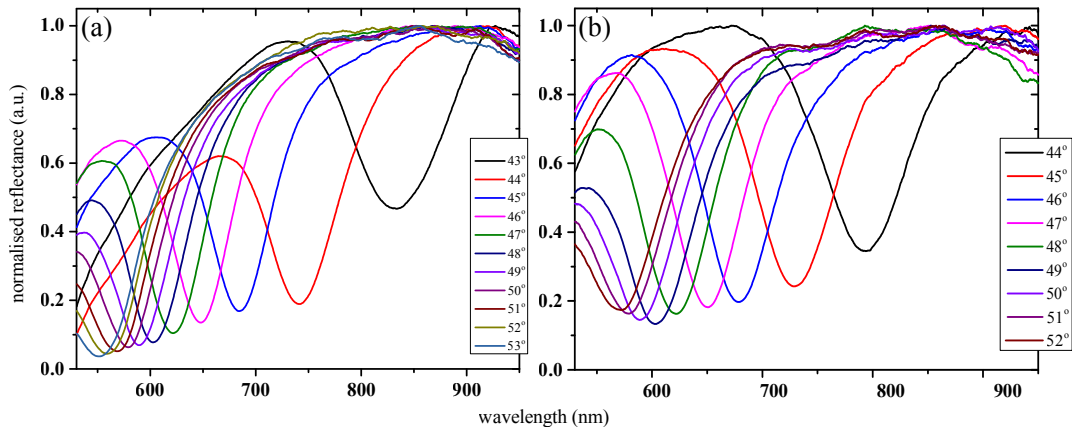


Figure 5.9: Reflectivity curves obtained for (a) PMMA layer (b) anthracene layer over gold with angle of incidence of excitation beam indicated in respective legends.

anthracene with a refractive index of 1.5 and 1.6 respectively. The ATR curves obtained for the configurations considered in figure 5.8 are shown in figure 5.9(a) and (b) for PMMA and anthracene respectively. Increase in the thickness of the dielectric medium with $n > 1$ on top of the gold film red-shifts the curves obtained for the same angle of incidence (and hence the k -vector), in accordance with their dispersion curves. However, it was seen that the curves for the sample with PMMA were often slightly narrower

than for anthracene, possibly due to less dispersion losses at the surface because of better film uniformity.

Strong coupling of DBT molecules with surface plasmons

In section 5.2, it was discussed how the coupling between quantum emitters and surface plasmons depends on various parameters as given by equation 5.11. Given the $\mu\sqrt{N/V}$ dependence of the coupling strength g , one important parameter that emerges is the number of coupled emitters N , given that the dipole moment and mode volume is fixed for a given system. In fact, SPP systems already have such small mode volumes that it is possible to achieve strong coupling at room temperatures (characterised by high dephasing) and without the need for a closed cavity. The Rabi splitting seen in the dispersion curve is proportional to the square root of the number of participating molecules (\sqrt{N}) and this relation can be used to observe the transition from weak to strong coupling between the two systems.

Experimentally however, observing strong coupling is not a simple task. SPP modes are inherently dissipative and thus the coherence times of the hybrid modes created by strong coupling are of the order of only 10–100 fs compared to typical emitter-microcavity coherence times 10–100 μ s [106]. Moreover at room temperatures, phonon-

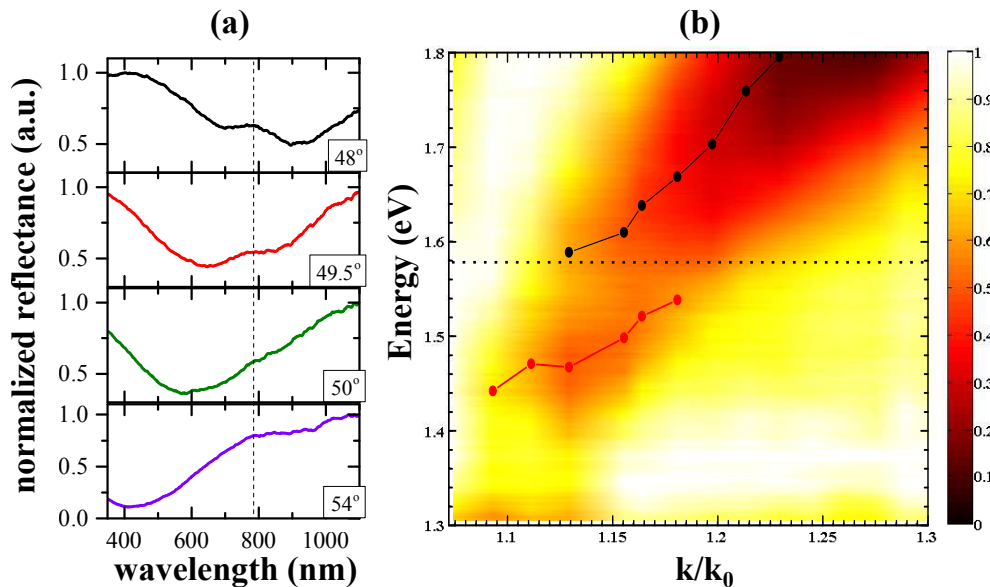


Figure 5.10: (a) Obtained reflectivity curves obtained for a sample with high concentration of DBT molecules in anthracene spin coated over gold with angle of incidence of indicated at the bottom left of each panel. (b) Corresponding dispersion curve indicating the lower (red) and upper (black) polariton branch. The dotted line indicates the DBT molecular mode at 785 nm in both (a) and (b).

coupling for molecules embedded in solid state matrices results in further broadening

of the modes, which makes it difficult to observe splitting in the dispersion curve. As a rule of thumb, the Rabi splitting has to be larger than the width of the individual modes to be observable in the dispersion graph. This issue can be visualised in figure 5.10, where a small splitting is visible in the ATR curves with a sample with high concentration of emitters (10 μM) but is hardly visible in the corresponding dispersion curve.

However, this can be considered an indication that the strong coupling regime is near, so higher concentrations of DBT molecules were spin coated over the gold film since the magnitude of Rabi splitting scales proportional to \sqrt{N} (equation 5.11). Unfortunately, we were unable to observe appreciable splittings in the dispersion curve. This can be attributed to several reasons. Spin coating of DBT:Ac crystals over gold results in a non-uniform distribution of DBT molecules due to poor adhesion of anthracene crystals with gold, and it becomes difficult to find points where the concentration of molecules is high enough. The non-uniformity also gives rise to surface defects where the SPs can scatter out and dissipate. Moreover, since the dipole of DBT molecules in anthracene lies parallel to the sample plane, their coupling to SPs is highly diminished compared to perpendicular dipoles [98].

Increasing the confinement of the plasmon mode is another way to increase the coupling between emitters and SPs since coupling g is considered to scale inversely with \sqrt{V} (see equation 5.11). Increased mode confinement can be achieved by plasmonic structures such ring resonators, waveguides, gratings, etc. compared to planar metal film, and is explained by the fact that these structures have a higher effective refractive index than planar films [107]. Two such structures were chosen for observing DBT-plasmon coupling, i.e. ring resonators and wedge waveguides, and the preliminary characterization results have been discussed in the following sections.

5.4 Plasmonic concentric-ring resonators

It is well-known that, in the weak coupling regime, optical cavities can significantly increase the spontaneous emission rate of active materials due to modifications in the local density of photonic states (LDOS) [3, 108, 109]. The Purcell factor F_p is directly proportional to the resonance Q-factor and inversely to the modal volume, $F_p \propto (Q/V)$, as long as the linewidth of the emitter is smaller than the cavity linewidth. One promising geometry for high Purcell enhancement is the metallic ring resonator, where deep subwavelength gap plasmon modes are formed within a nanoscale annular region. Such resonators give rise to localized surface plasmon modes that can couple to the radiation emitted by emitters placed within the mode volume [110]. Due to high confinement there are increased losses, such that these resonators have relatively low Q-factors and hence any Purcell enhancement induced by the localized plasmon resonances would be observed over a large bandwidth.

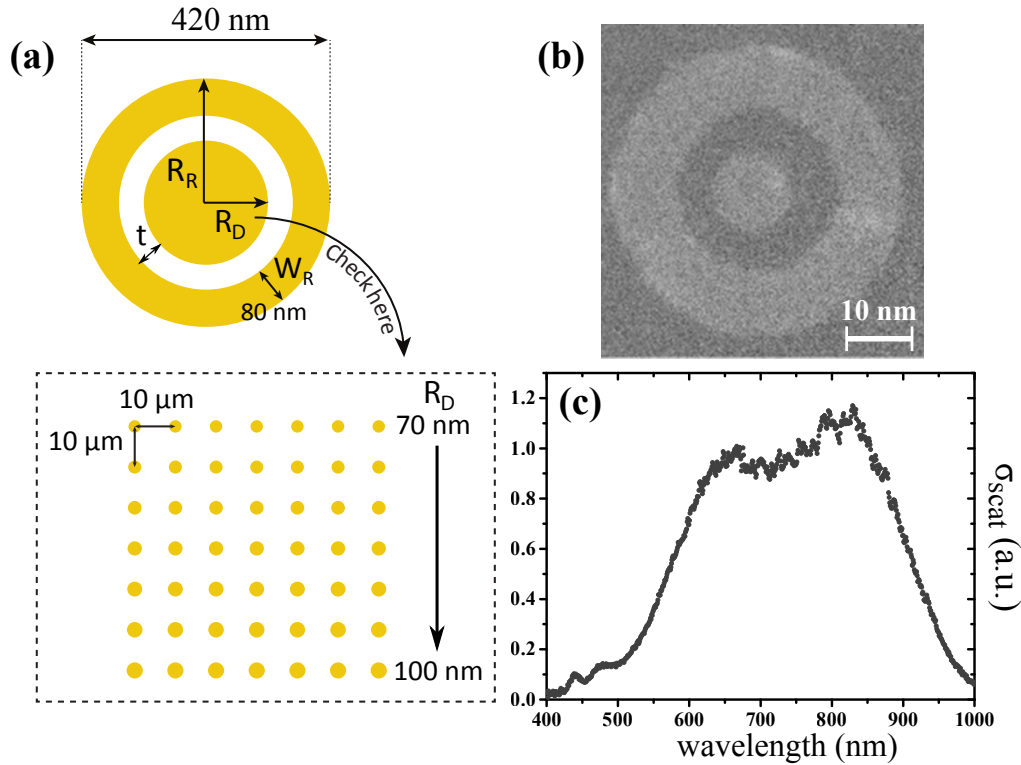


Figure 5.11: Plasmonic concentric-ring resonators: (a) Schematic and layout of the resonators (b) SEM image (c) A typical scattering cross-section obtained for the fabricated resonators by dark field microscopy, showing that they have a broad resonance.

In this work, we aim to characterize plasmonic ring resonators whose structure and spectral response are shown in figure 5.11. The structure consists of a disk located concentrically within an outer ring, both made of a gold film with height $h \simeq 40$ nm in a metal-insulator-metal (MIM) configuration. The radius and width (R_R, W_R) of the outer ring are kept constant throughout at 210 nm and 80 nm respectively, while the radius of the inner disc (R_D) is increased with each row of the layout, thus varying the dielectric gap (t) between them with each row as well.

The fabrication of the devices was carried out at the Imperial College of London. A PMMA-based positive resist was used to define the resonator structure by e-beam lithography, by which the part exposed to the electron beam is etched away, and left empty spaces on the glass where the gold could be deposited. Since gold doesn't adhere well to the silicon oxide (glass) substrate, first a very thin interface layer was introduced. Two options were implemented: an organic self-assembled monolayer (SAM) that adsorbs itself onto the glass, or a 5 nm chromium (Cr) metal layer deposited by thermal evaporation. After this, gold was deposited with thermal evaporation process upto a height of 40 nm. The final structure was obtained by a lift-off technique, where the

remaining PMMA lifts off from the sample and also carries away the other layers deposited on it, thus leaving the resonator structure behind on the sample.

Scattering cross-sections for the resonators were obtained by dark field microscopy, where the resonator only scatters the part of the excitation spectrum it is resonant with [111]. Thus by normalizing the obtained signal with a reference sample which has a unity response for all wavelengths, it is possible to obtain their resonance spectra. Figure 5.11(c) shows that they have a very broad resonance. This can be useful for coupling spectrally different emitters with them, but at the same time is detrimental to the Q -factor, which is defined as $Q = \lambda/\Delta\lambda$.

Following this procedure, a solution with a high concentration of DBT molecules in anthracene was spin coated on top of the sample, resulting in thin DBT:Ac crystals with a nominal height of about 50 nm. Figure 5.12 shows the images of the sample taken with a broadband (whitelight) source and a 763 nm laser in widefield configuration (imaging setup described in section 2.1.1), where the resonators appear as bright (almost diffraction limited) spots on the EM-CCD camera and showed an average of 2.5-3 times photoluminescence enhancement compared to the surrounding molecular fluorescence. It was verified that this enhancement was not merely due to the presence of gold, as it did not appear at other locations having the same gold layer, but instead seemed to be an effect produced due to coupling to the resonators.

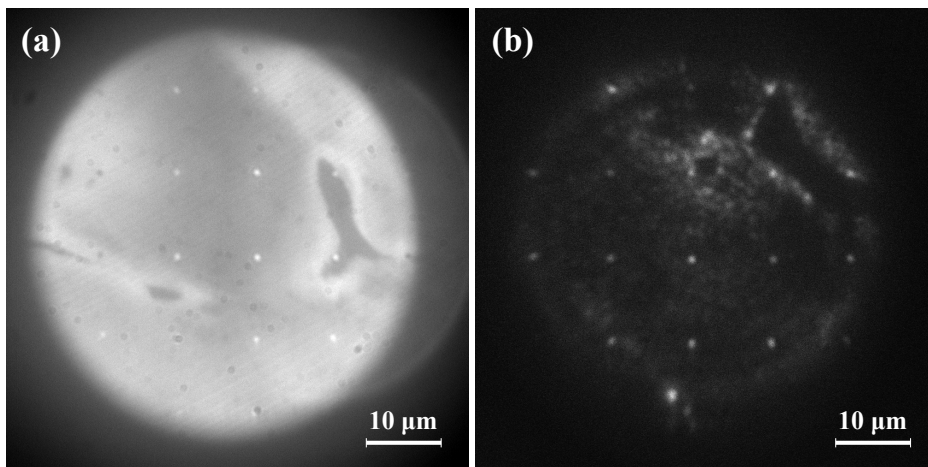


Figure 5.12: (a) Whitelight and (b) widefield (fluorescence) images of the plasmonic resonators.

For further characterization, spectra were measured at resonator locations, which yielded some very interesting results. Figure 5.13 shows the obtained spectrum at one of these resonators, and several sharp peaks are clearly evident. This is in contrast with the broad spectrum of DBT molecules obtained from the sample in a place outside the range of the resonator (also shown in figure 5.13 in light gray). Several other resonators exhibited a similar response with peaks at the same wavelengths as those shown in the figure. These peaks fit a Lorentzian profile which indicates that they can

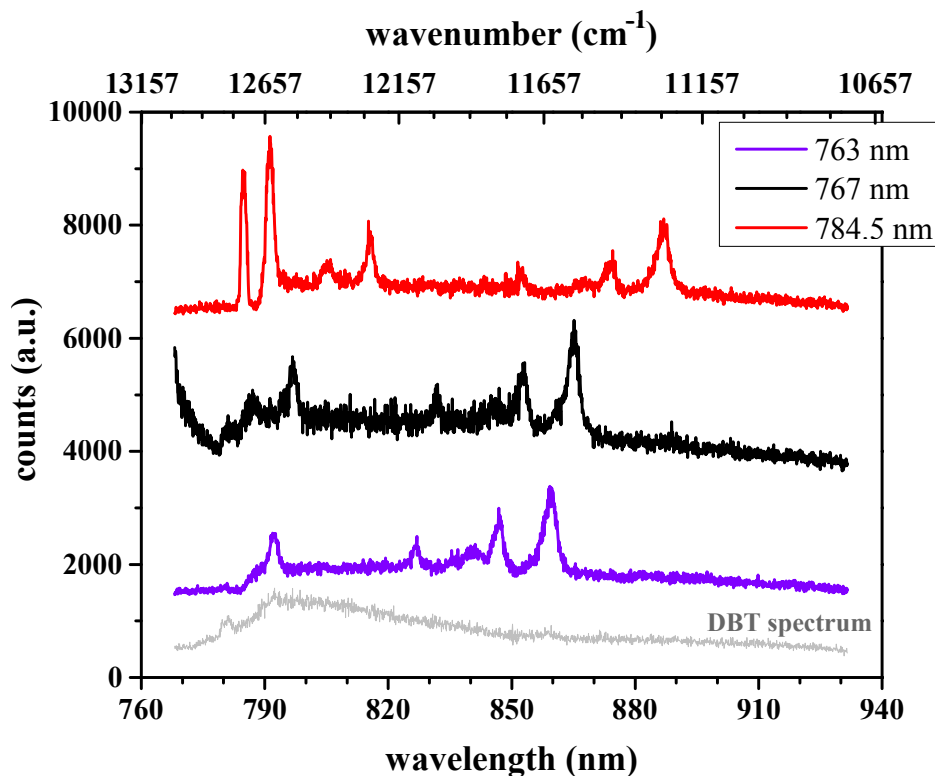


Figure 5.13: Spectral response of the resonators.

be Raman peaks. To verify this assumption, spectral measurements were made with other excitation laser wavelengths. Figure 5.13 collectively shows the emission spectra collected with three different laser wavelengths, namely 763 nm, 767 nm and 784.5 nm. This comparison thus confirms that it is indeed a Raman spectrum, and not peaks corresponding to either the modes of the resonator or vibrational transitions in the molecular species involved.

It was, however, unclear what was the source of this Raman spectrum. The peaks did not match appreciably with the vibrational peaks for either DBT or anthracene, and for this reason, new samples were fabricated and the spectra of bare resonators were measured before adding spin coated DBT:Ac crystals on top. Strangely, some of them did show the same Raman peaks without the presence of either DBT or anthracene. The molecules constituting the SAM layer were ruled out as a possible source because similar spectra were also recorded for resonators with a chromium base layer instead of the SAM. Also, the presence of leftover PMMA-based resist that was used for the e-beam fabrication mask was uncorrelated with the presence of the said Raman peaks. A likely candidate could be a chemical called eSpacer, which was used for SEM imaging of these resonators.

Regardless of the source of these features, it seems like the resonators present a viable platform for observing Raman enhancement since due to their low-noise response and small size, it might become possible to perform single molecule SERS by probing Raman

scattering in the optical near field. Now it is hard to quantify the increase in radiative emission rate in such resonators due to Purcell enhancement by solely looking at the photoluminescence intensity, since large modifications of the non-radiative decay rate, pumping and collection efficiencies are also possible at the same time. Therefore, it would be useful to perform full 3-D full-vector finite difference time domain (FDTD) simulations in the future to rigorously quantify the modification of decay rates due to Purcell enhancement.

5.5 Plasmonic waveguides

In addition to mode confinement and enhancement, plasmonic structures can also offer directionality in the propagation of SPPs by tailoring the geometry of the metal structure. Various geometries of plasmonic waveguides have been proposed in literature: stripes [112], nanowires [113, 114], channels [115, 116], wedges [117, 118], hybrids [119, 120]. Among the many possible shapes, wedge and channel waveguides offer extremely small mode sizes while still maintaining relatively long propagation lengths. This can allow quantum emitters to couple efficiently to the confined mode and transmit signals over long distances [82].

The transversal mode confinement in wedge and channel waveguides can be understood as a consequence of a break in symmetry in the cross-section plane (orthogonal to the direction of propagation). Such spatial modification increases the effective index experienced by the SPP on a waveguide, which is higher than the one for free space and that for the SPPs on flat surfaces [117]. Thus, the SPP is more confined in this plane and left to propagate in the 1D-invariant direction along the length of the guide. However, with increased mode confinement comes increased mode loss, which is reflected in the value of the propagation length. However, in general, these losses arise both from intrinsic dissipation in the material and imperfections in the fabricated structure. The propagation length of the plasmon along the guide can be estimated according to $L_{\text{SPP}} \simeq (2k_x'')^{-1}$ as before. For decreasing wavelengths, it has been observed how the propagation length diminishes due to the general trade-off between confinement and loss for SPPs [117].

Wedge waveguides

As a first step, it was considered to develop a sample with different waveguide lengths and widths for operating wavelengths around 785 nm, which is specific to DBT molecules in anthracene. The sample consists of multiple sets of waveguides with four widths, $W = 3, 5, 7.5$ and $10 \mu\text{m}$. Their lengths vary from 10–40 μm in steps of 2.5 μm . The various steps involved in the fabrication of the waveguides are illustrated in the figure 5.14. A Silicon wafer with a crystal plane $\langle 100 \rangle$ is used and channels are made into it with KOH etching. The angle of the etch θ_t is given by the crystal plane of the Si wafer

and is fixed, and therefore the height $H = (W/2) \tan 56^\circ$ is determined by the width of the guide. The radius of the tip R_t depends in general on the etching process. These samples were also fabricated at the Imperial College of London.

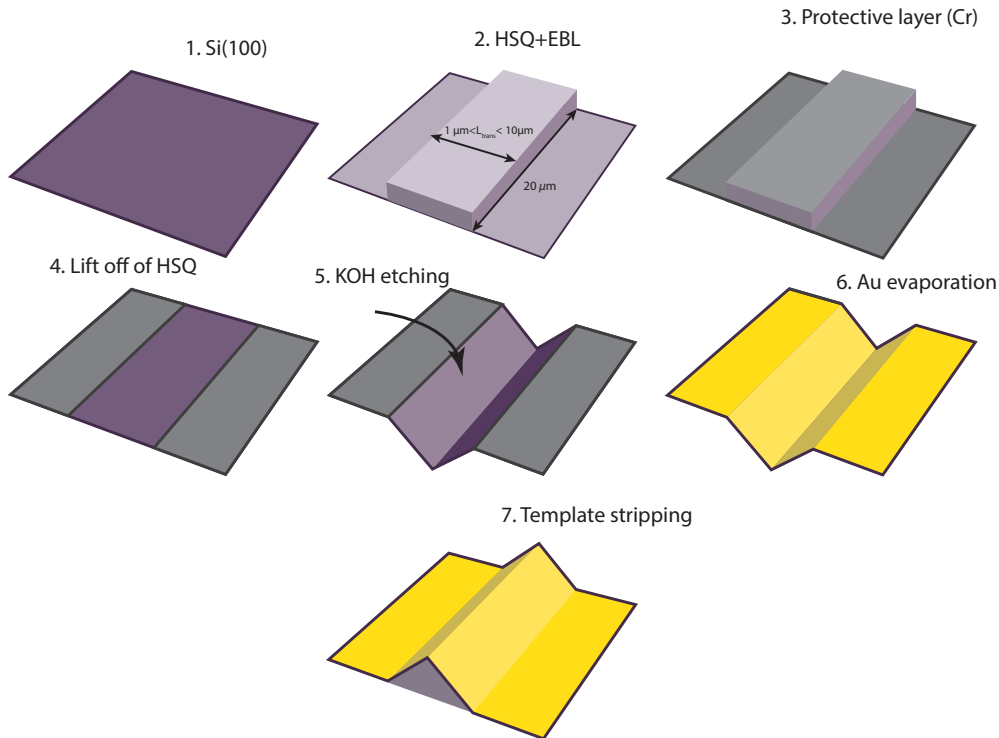


Figure 5.14: Fabrication process for plasmonic wedge waveguides.

Figure 5.15 shows the 2D-simulation of a plasmonic wedge waveguide used in this work. The finite element method (FEM) simulations were performed in COMSOL to estimate the effect of anthracene layer, since other parameters i.e. height H , the taper angle θ_t and the radius of the tip R_t were all given by the chosen fabrication process. After a certain critical height H_c of the waveguide for a certain mode frequency, the effective refractive index of the guide saturates and hence the height of the guide has rather no influence on the confinement of the mode beyond that value [117]. This can be understood as: for decreasing heights the mode on the tip feels the presence of the substrate more significantly, and consequently the substrate starts expelling the mode from the tip and the modal effective index decreases. For a waveguide higher than this interaction region, the surrounding flat surface has negligible influence.

It is evident that the wedge waveguide concentrates the electric fields on the apex to tiny sub-wavelength volumes and produce large field enhancements, thereby aiding better coupling with emitters placed within this region, as well the directionality of the propagating SPP mode. For a basic characterization, thin layers of anthracene

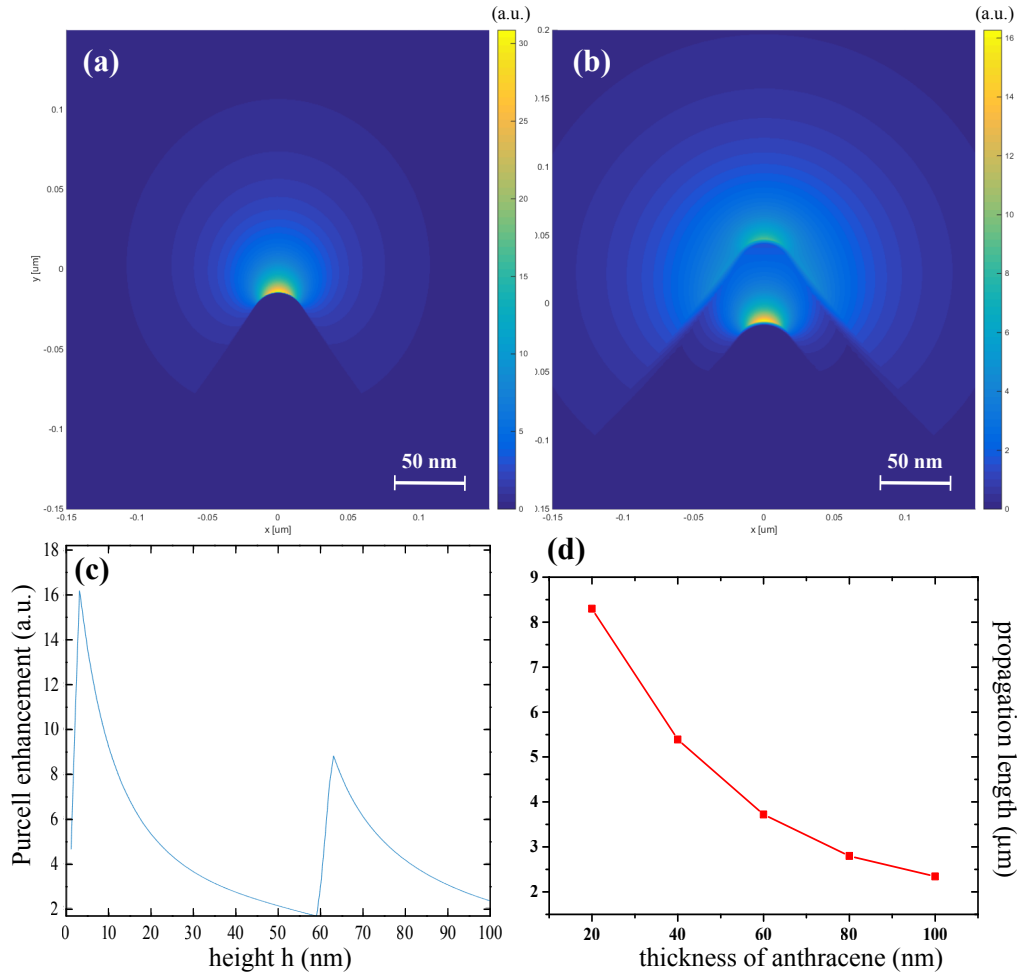


Figure 5.15: Wedge waveguide structure mode distribution (a) without anthracene (b) with 60 nm anthracene layer (c) Purcell enhancement with height h going vertically up from the apex in panel (b). (d) Variation in propagation length with thickness of anthracene layer.

containing a high concentration of DBT molecules were spin coated on top of these structures. Figure 5.16 shows images taken with whitelight and laser sources in the widefield and confocal microscope configurations.

However, in general, we found it quite difficult to find wedges that were completely covered as those shown in the figure 5.16 and the crystals typically failed to reach the apex in many occasions. This is probably due to less affinity between the gold and the anthracene crystals, which becomes crucial when spin coating on non-planar surfaces. We are currently looking at surface modification of the gold layer by thiol chemistry, which has been shown to increase its adhesion for organic materials [121].

The above is part of an ongoing work, where we are also trying similar experiments with channel waveguides. These two geometries exhibit propagation lengths of several microns, but till date few experimental works have achieved significant coupling effi-

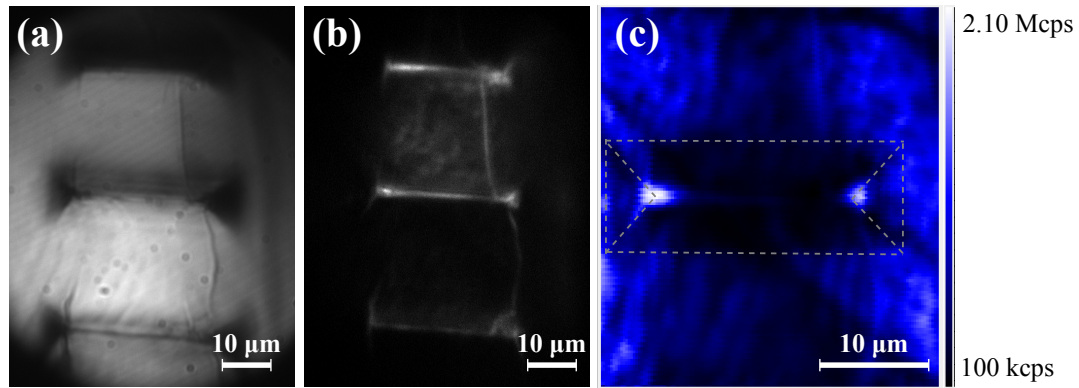


Figure 5.16: (a) Whitelight (b) Widefield and (c) confocal scan images for wedge waveguides. Both (b) and (c) were obtained with the long-pass filter in detection, so the intensity represents the fluorescence counts. Bright lines along the apex were observed alongwith high scattering at the end points of the waveguide.

ciencies while utilising them [116, 122, 123]. These waveguides have also been predicted to enable efficient dipole-dipole resonant energy transfer along the longitudinal axis of the waveguide, and such an energy transport empowered through plasmon transport can also give rise to interesting quantum coherent effects such as Dicke superradiance and entanglement between distant emitters [82]. Moreover, the guiding functionality of these waveguides extends from the visible to the terahertz range of the spectrum, and it can be interesting to couple other single photon sources that emit at longer wavelengths, where losses of the waveguides are deemed to be lower.

6 Coupling to Lossy waves in Graphene

6.1 Introduction

Graphene is a two-dimensional sheet of carbon atoms arranged in a honeycomb-shaped lattice. It can also be considered the building block of other forms of carbon like graphite, carbon nanotubes, fullerenes, etc. Successfully isolated in 2004, graphene became the first example of a truly 2-D material stable at room temperature and has since been widely studied due to its exceptional structural, electronic and optical properties.

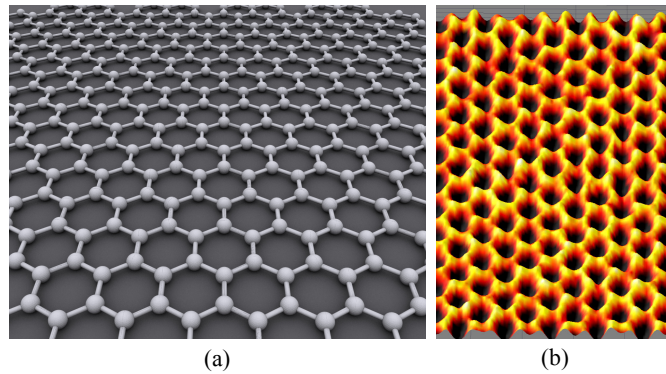


Figure 6.1: (a) Lattice model (b) Scanning probe microscopy image of graphene. Ref: Wikipedia

Many of its interesting electrical and optical properties arise from its unusual band structure which is shown in figure 6.2. Graphene exhibits a gapless band-structure and thus can be considered as a semimetal with a zero band overlap or a semiconductor with zero band gap [124]. Moreover, in the low energy range around the Fermi level, the conduction and valence bands have conic shape - the so-called *Dirac cones* - and the relation between energy E and momentum k for an electron in graphene becomes:

$$E(k) = \hbar v_F k \quad (6.1)$$

where v_F is the Fermi velocity. This *linear* dependence on the wavevector makes it similar to a relativistic particle [125], and thus charge carriers in graphene at the Fermi energy E_F level have zero effective mass and behave as Dirac fermions. They are described by the relativistic Dirac equation rather than the Schrödinger equation with

$v_F = 10^6 \text{ m s}^{-1}$ being the Fermi velocity in graphene, only a factor of 100 lower than the speed of light [124].

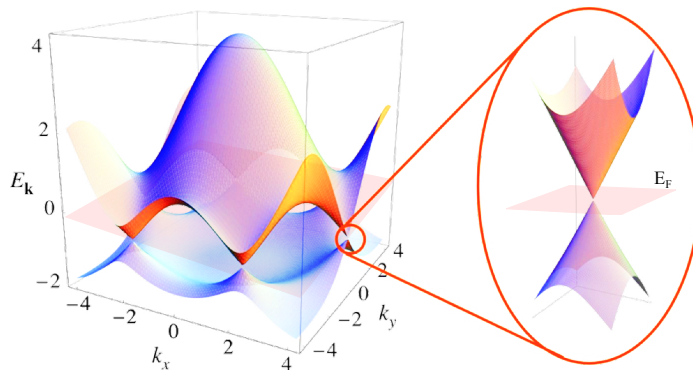


Figure 6.2: Graphene band-structure: in the low energy range around the Fermi level, the conduction and valence bands form Dirac-cones and the electronic dispersion relation becomes linear.

The observed carrier mobility μ only weakly depends on temperature T and is thus only limited by impurity scattering even at 300 K. Highly crystalline samples show mobilities up to $\sim 2 \times 10^5 \text{ cm}^2 \text{ V}^{-1} \text{ s}^{-1}$ [126], which is the highest mobility observed at room temperature when compared with typical values of $\mu_{\text{Cu}} \sim 30 \text{ cm}^2 \text{ V}^{-1} \text{ s}^{-1}$ and $\mu_{\text{Si}} \simeq 10^3 \text{ cm}^2 \text{ V}^{-1} \text{ s}^{-1}$, for copper and silicon respectively. All these properties translate into ballistic transport on a submicrometre scale at 300 K, which makes graphene a potential material for nanoelectronics [127, 128].

Graphene also shows remarkable optical properties derived from its gapless band-structure. Since an absorbed photon of any visible frequency ω can produce an electron-hole pair, undoped graphene strongly interacts with light and exhibits a nearly constant optical absorption across the VIS spectral region [129]. The optical absorption depends only on fundamental constants (proportional to $\pi\alpha$, with α being the fine structure constant), and is approximately equal to 2.3% [130]. This means that graphene, despite being only one-atom thick, can absorb a significant fraction of an incident white light and can be visible to the naked eye.

A recent study [131] demonstrates that graphene indeed exhibits a strong photore-sponse, which means that the conversion of light into free electron-hole pairs is very efficient. Carrier-carrier scattering prevails as a relaxation process over optical-phonon emission, allowing for highly efficient graphene-based photodetectors.

6.2 Graphene-DBT coupling

While the discussion above describes far-field interaction between light and graphene, new coupling mechanisms emerge when light sources are brought in the near-field:

Charge Transfer

This mechanism involves the transfer of a charge-carrier belonging to an excited single quantum emitter to a nearby graphene monolayer [132, 133]. Changing the charge carrier density shifts the Fermi level and thus introduces *doping* in graphene. This specific process can thus be described as photo-induced doping and has been exploited, for example, to enhance the responsivity of graphene-based photodetectors by covering the graphene sheet with colloidal quantum dots [134].

Energy Transfer

Depending on the energy of the emitter with respect to the Fermi energy [135], the energy transfer mechanism can assume two different forms: it can excite collective excitations (plasmons) ($E < 2E_F$) or it can be absorbed as ohmic losses ($E > 2E_F$).

Graphene plasmons exhibit a tight confinement, a relatively long propagation distance and a highly tunable spectrum, and thus represent an attractive alternative to traditional metal plasmons for QED studies [135].

The non-coherent energy transfer to lossy waves is theoretically described as a FRET-like mechanism where the two interacting dipoles are the emitter and the electron-hole pair in graphene [136–138].

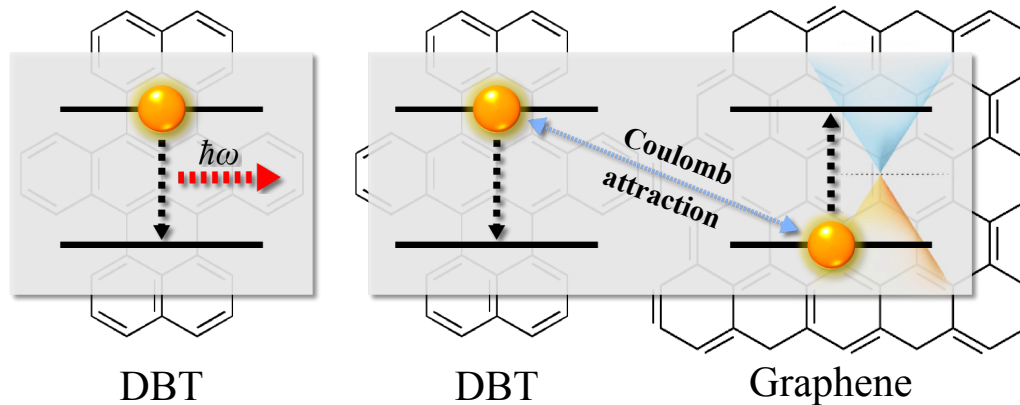


Figure 6.3: Energy diagram of a DBT molecule in free space and nearby an undoped graphene monolayer sheet, where the relaxation of the excited state occurs primarily through non-radiative dipole-dipole energy transfer to graphene, and thus reduces the number of photons that would normally be emitted due to radiative relaxation (quenching). The lifetime of the emitter excited state (τ_g) is shorter than the one in free space ($\tau_g < 1/\Gamma_0$), due to the new non-radiative relaxation channel.

The **Förster resonance energy transfer** (FRET) mechanism involves an excited emitter, say a donor, and an unexcited acceptor molecule [23]. If the emission spectrum of the donor overlaps with the absorption spectrum of the acceptor and their reciprocal

distance d is within the so-called Förster critical distance d_0 , energy transfer occurs due to Coulomb interaction between the two dipoles.

When FRET occurs, a non-radiative channel opens up and the donor's fluorescence quenches. Since the fluorescence lifetime depends on both radiative and non-radiative processes (see equation 1.37), the energy transfer results in the reduction of donor's lifetime. Therefore, by measuring the donor fluorescence lifetime in the presence (τ_a) and absence (τ_0) of an acceptor (or measuring equivalently the quenching of donor fluorescence), it is possible to quantify the energy transfer process. For an isolated dipole-dipole interaction, the transfer energy rate k has a d^{-6} dependence, allowing distance d and efficiency η of energy transfer to be determined through the following relations:

$$k = \frac{1}{\tau_0} \left(\frac{d_0}{d} \right)^6 \quad (6.2)$$

$$\eta = 1 - \frac{\tau_a}{\tau_0} \quad (6.3)$$

where d_0 is the maximum separation between donor and acceptor molecules under which resonance energy transfer can occur and whose value can be derived from spectroscopic data measured on the donor-acceptor pairs.

The FRET mechanism described so far for two nearby interacting molecules can easily be extended to more complex coupled systems. If the acceptor takes the form of a line of dipoles, integration over all possible transfer sites yields a d^{-5} dependence. A surface of acceptors gives instead a d^{-4} dependence and transfer to the bulk shows a d^{-3} dependence. Because of this strong distance-dependence and since the critical distance value typically falls within a range of ~ 10 nanometers, FRET mechanism has been suggested [139] and up to now mainly exploited as a ruler capable of measuring small nanometric distances. Indeed, FRET-based nanorulers are used to report conformational changes, molecular interactions and intermolecular distances between directly interacting biomolecules like proteins, nucleic acids and macromolecular complexes [140–143]. As a non-invasive technique, FRET holds several advantages over biochemical methods, in which the cells involved in the mechanism under investigation are disrupted. Nevertheless, FRET-based nanoruler made of a donor-acceptor dye pair suffer from an upper distance limit of about 10 nm [144].

In this work, the modification of the spontaneous emission rate of DBT dye molecules caused by a single metallic planar surface made of a graphene sheet is investigated (see figure 6.3). Graphene's unequaled conductivity gives rise to a very strong polarizability, resulting in an efficient energy transfer from donor molecules. As will be discussed in the next section, with the chosen experimental parameters the main coupling mechanism is a FRET-like energy transfer to graphene. Because of the 2-D character of graphene, the FRET efficiency scales with the 4-th power of distance. With this distance-dependence, the rate of energy transfer can be extended up to a distance of 30 nm [145], potentially

overcoming the maximum distance limit of the traditional FRET nanoruler. Indeed, based on the near-field interaction between biomolecules and graphene and on the universality of its strong distance-dependence, a wealth of sensing applications have been proposed [146–148].

6.3 Experimental details

The graphene sample used in this work was provided by the Institute of Photonic Sciences (ICFO) in Barcelona. It was grown by a chemical vapour deposition (CVD) technique on copper, and then transferred to a microscope coverslide, after which it was annealed in an H_2 -Ar (1:5) atmosphere at 300°C for 3 hours.

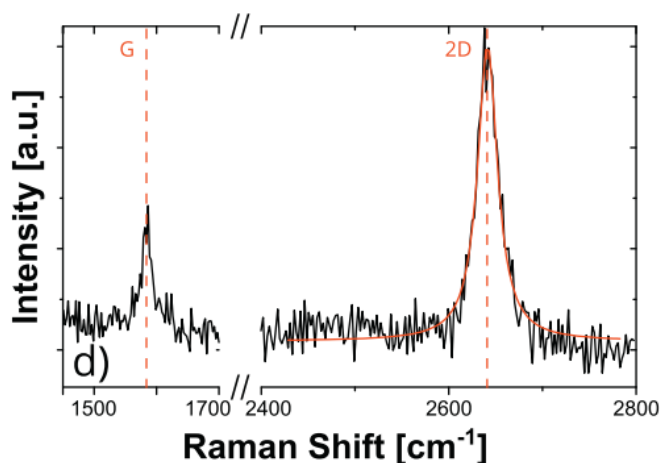


Figure 6.4: Measured Raman spectrum of the CVD graphene sample, acquired at ambient light turned off. Note that the characteristic lines are at 1581 cm^{-1} and 2640 cm^{-1} , with a relative ratio between the intensity of the 2D and the G bands being around 2 - evidence of an atomic monolayer.

To check its quality and uniformity, the CVD-specimen was probed in confocal configuration with the CW green laser with an impinging power of 3 mW, which is about 600 kW cm^{-2} for a 532 nm-diffraction-limited spot (see Chapter 2).

The Raman spectrum measured is shown in Figure 6.4: the intensity ratio I_{2D}/I_G of ~ 2 and the Lorentzian fit of the 2D-band indicate that the CVD-graphene sample is a monolayer.

As in previous experiments, a small amount of DBT:Ac solution was then spincoated onto the graphene substrate at a spin speed of 3000 rpm which yields anthracene crystals with a thickness between 20–80 nm. Hence, the embedded DBT molecules are positioned at a distance d from graphene that is much smaller than their emission wavelength $\lambda \simeq 785\text{ nm}$. This means that DBT-graphene interaction is by definition in the near-field. As the CVD-sample is an undoped monolayer, the excitation energies are above twice the Fermi energy and graphene plasmons cannot be excited. Moreover,

the charge transfer mechanism is prevented because DBT molecules in anthracene are electrically isolated. Hence, with these chosen experimental parameters, only the non-radiative dipole-dipole energy transfer can occur.

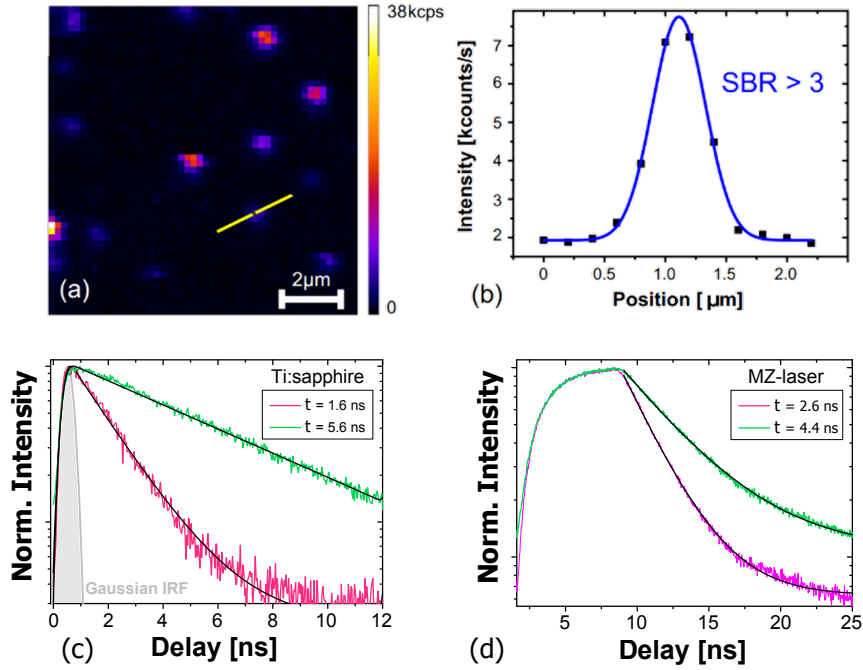


Figure 6.5: (a) Confocal fluorescence scan showing DBT molecules over graphene. This map helps to spatially pin-point single molecules for further measurements. (b) A selected bright spot fits a Gaussian profile with a signal-to-background ratio (SBR) > 3 . (c) and (d) Measurements with Ti:sa and MZ-modulated laser respectively. The traces are fitted with a single exponential decay function to obtain fluorescence lifetimes.

With the single molecule detection techniques highlighted in section 2.1, single DBT molecules were selected using a lower-bound SNR of 3 (since fluorescence quenching is a sign of energy transfer). The chosen molecules were excited with the pulsed source (Ti:sapphire or MZ-modulated laser) in confocal configuration, with an impinging power of $250 \mu\text{W}$ (about 100 kW cm^{-2} for a 767 nm -diffraction-limited spot). The excitation source polarization was aligned with the emitter dipole by means of a half-wave plate in the excitation line and by maximizing the photon count rate detected with the APD. The DBT-relaxation dynamics were then recorded by a single APD, coupled to the TCSPC unit (20 s acquisition time).

Typical recorded fluorescence signals are shown in Figure 6.5 (c) and (d), for the Ti:sapphire and MZ-modulated excitations respectively. With the same detection conditions and acquisition time, a background (BG) signal was recorded, focusing the

confocal laser-spot on the anthracene crystal far from DBT molecules. This BG signal was subtracted from each fluorescence signal to give a reliable baseline for lifetime extraction. For the specific DBT:Ac system, intensity is physically described by a single exponential decay. The lifetime fits were done by DecayFit software [149] using a Gaussian instrument response function (IRF).

As molecules are placed in different positions within the anthracene crystal, the fluorescence lifetime and intensity significantly vary from one molecule to the other, as they depend on the local nano-environment (see Section 6.4). To isolate the impact of graphene on the fluorescence of single DBT molecules, more than one scan were done, when possible, on the same crystal and far from edges, to avoid inhomogeneity and to ensure the same crystal-thickness. Additionally, statistics were also taken for a reference sample produced by spin coating DBT:Ac on a reference glass coverslip.

6.4 Results and discussion

A total of about 225 single DBT molecules were observed and recorded: 75 molecules on the reference sample and 150 molecules placed on the graphene monolayer. Figures 6.6(a) and (b) show the excited-state lifetime distributions for the reference and graphene samples respectively. The bin size is given by the time resolution of the setup, amounting to 400 ps. At first glance, it is evident that the histogram for reference molecules presents a symmetric distribution, while the one for molecules situated over graphene is asymmetric with a long tail for short lifetimes, indicating the coupling to graphene excitons.

The distribution in figure 6.6(a) can be fitted predictably with a Gaussian centered around $\tau_0 = 4.2$ ns with a standard deviation $\sigma_0 \simeq 0.4$ ns. Assuming a 40 nm thick anthracene crystal and the in-plane orientation of DBT molecules, while imposing proper boundary conditions, we estimate a 10% total lifetime variation due to interface effects, resulting in approximately half the experimental spread. As suggested in [150, 151], the observed variation of lifetimes for DBT can be inferred as a combination of both local environment and edge effects, that do not alter the symmetry of the Gaussian distribution.

The distribution for DBT molecules over graphene was analysed with a semi-classical model introduced in section 1.4, adapted for the case of a molecule interacting with a two-dimensional material. The emitter is described by the electric dipole moment of the electronic transition, and the decay rate Γ_g of the emitter at a distance d from a monolayer graphene can be calculated using the power radiated by the electric dipole, placed in a semi-infinite medium with permittivity ϵ_{med} [152].

Considering the total field as a result of the interference between the dipole emission and its Fresnel reflection, the spontaneous emission rate Γ_g follows a universal distance-scaling law governed by the fine structure constant α and the fluorescence wavelength λ_0 [137]. Referring to the analysis in [153] in which graphene is represented through

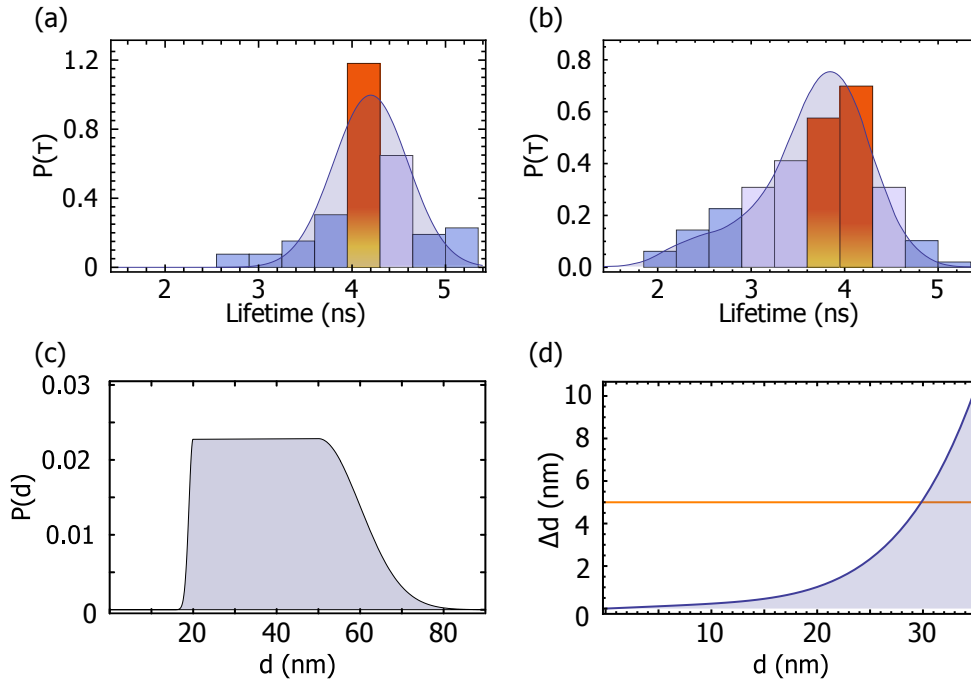


Figure 6.6: Probability density function of single molecule excited-state lifetimes on (a) the reference sample and (b) the graphene monolayer sheet. The histogram represents the experimental values collected with both pulsed sources. The solid lines result from the semiclassical model given by equation 6.4. (c) The assumed molecule depth distribution inside anthracene crystals used in the theoretical model. This distribution accounts for the shortest detectable lifetime and the average crystal thickness of (50 ± 10) nm, according to AFM measurements [30]. (d) The uncertainty in position measurement Δd is calculated based on the model and takes into account the lifetime spread of DBT molecules. The horizontal line cuts the graph at 30nm, where the critical distance for DBT-graphene FRET transfer has been estimated.

its DC conductivity ($e^2/4\hbar$), Γ_g is found to be:

$$\frac{\Gamma_g}{\Gamma_0} \simeq 1 + \frac{9\nu\alpha}{256\pi^3(\epsilon_{\text{sub}} + \epsilon_{\text{med}})} \left(\frac{\lambda_0}{d}\right)^4 \quad (6.4)$$

where Γ_0 is the free-space decay rate, ν accounts for the dipole orientation ($\nu = 1$ or 2 when the emitter is oriented parallel or perpendicular to graphene), $\epsilon_{\text{med}} = \epsilon_{\text{anthracene}}$ and ϵ_{sub} is the permittivity of the substrate. Note that in equation (6.4), reference to graphene's properties is included in the fine structure constant (related to its absorption coefficient) and in the d^{-4} distance dependence (attributed to its 2D character).

In order to test the model with the actual system, an educated guess for the molecule position distribution is made and then inserted in equation 6.4. It is assumed that DBT molecules are homogeneously distributed inside anthracene crystals, whose thicknesses

are on average 50 ± 10 nm, according to AFM measurements. A cutoff on the distribution is introduced, accounting for the aforementioned quenching of molecules, which makes detection difficult for distances to graphene closer than 20 nm. The resulting probability density function (PDF) of the molecule position distribution is shown in figure 6.6(c).

The expected PDF for molecular lifetimes are plotted against experimentally observed distributions, as shown in figures 6.6 (a) and (b). The agreement clearly confirms the validity of the model, whose simple final formulation and dependence on universal parameters makes this system a promising candidate for a nanoscopic ruler.

Finally, in figure 6.6(d), the uncertainty in position measurement is shown for the specific case of DBT molecules in anthracene. Only the effect of the intrinsic DBT:Ac lifetime spread has been included and no cutoff due to detection is considered, assuming an ideal setup. The distance of DBT molecules to the graphene interface can be determined with an accuracy below 5 nm, for distances smaller than 30 nm.

The energy transfer efficiency by the Förster mechanism can be calculated by equation 6.3 when the emitter intrinsic quantum yield amounts to 1. In this work, 12% of the measured molecules show an energy transfer efficiency higher than 40%, which is the maximum value reported in literature for single emitters [154, 155]. The maximum observable efficiency is limited by instrumental issues, such as minimum detectable lifetime and SNR, and thus does not represent absolute limitations for the proposed nanoruler. The maximum observed efficiency amounted to $(61 \pm 21\%)$ given by:

$$\eta_{\max} = 1 - \frac{\tau_g}{\tau_0} \simeq 0.61 \quad (6.5)$$

where $\tau_g = 1.6$ ns is the smallest fluorescence lifetime measured of a single DBT molecule on graphene. The uncertainty is estimated taking into account the fluctuations in the reference value and the precision of lifetime measurements.

Bibliography

- [1] W. Barnes. “Fluorescence near interfaces: the role of photonic mode density”. In: *journal of modern optics* 45.4 (1998), pp. 661–699.
- [2] E. Fermi. “Quantum theory of radiation”. In: *Reviews of Modern Physics* 4 (1932), pp. 87–132.
- [3] E. M. Purcell. “Spontaneous emission probabilities at radio frequencies”. In: *Physical Review* 69 (1946), p. 681.
- [4] K. H. Drexhage. “IV interaction of light with monomolecular dye layers”. In: *Progress in Optics* 12 (1974), pp. 163–232.
- [5] T. Schwartz, J. A. Hutchison, C. Genet, and T. W. Ebbesen. “Reversible switching of ultrastrong light-molecule coupling”. In: *Physical review letters* 106.19 (2011), p. 196405.
- [6] B. Lounis and M. Orrit. “Single-photon sources”. In: *Reports on Progress in Physics* 68.5 (2005), p. 1129.
- [7] P. Hänggi, P. Talkner, and M. Borkovec. “Reaction-rate theory: fifty years after Kramers”. In: *Reviews of Modern Physics* 62.2 (1990), p. 251.
- [8] M. Fox. *Quantum Optics: An Introduction*. Vol. 15. Oxford University Press, 2006.
- [9] D. A. Steck. *Quantum and Atom Optics*. 2006.
- [10] J. R. Lakowicz. *Principles of fluorescence spectroscopy*. Springer, 2007.
- [11] M. Kasha. “Characterization of electronic transitions in complex molecules”. In: *Discussions of the Faraday society* 9 (1950), pp. 14–19.
- [12] R. G. Hulet, E. S. Hilfer, and D. Kleppner. “Inhibited spontaneous emission by a Rydberg atom”. In: *Physical Review Letters* 55 (1985), pp. 2137–2140.
- [13] D. Englund, D. Fattal, E. Waks, G. Solomon, B. Zhang, T. Nakaoka, Y. Arakawa, Y. Yamamoto, and J. Vučković. “Controlling the spontaneous emission rate of single quantum dots in a two-dimensional photonic crystal”. In: *Physical review letters* 95.1 (2005), p. 013904.
- [14] P. Goy, J. Raimond, M. t. Gross, and S. Haroche. “Observation of cavity-enhanced single-atom spontaneous emission”. In: *Physical Review Letters* 50 (1983), pp. 1903–1906.

- [15] F. L. Kien, N. H. Quang, and K. Hakuta. “Spontaneous emission from an atom inside a dielectric sphere”. In: *Optics Communications* 178.1 (2000), pp. 151–164.
- [16] A. Bouhelier, M. Beversluis, A. Hartschuh, and L. Novotny. “Near-field second-harmonic generation induced by local field enhancement”. In: *Physical Review Letters* 90.1 (2003), p. 013903.
- [17] M. Bayer, T. Reinecke, F. Weidner, A. Larionov, A. McDonald, and A. Forchel. “Inhibition and enhancement of the spontaneous emission of quantum dots in structured microresonators”. In: *Physical Review Letters* 86.14 (2001), p. 3168.
- [18] T. Gutbrod, M. Bayer, A. Forchel, P. Knipp, T. Reinecke, A. Tartakovskii, V. Kulakovskii, N. Gippius, and S. Tikhodeev. “Angle dependence of the spontaneous emission from confined optical modes in photonic dots”. In: *Physical Review B* 59.3 (1999), p. 2223.
- [19] J. Aizpurua, P. Hanarp, D. Sutherland, M. Käll, G. W. Bryant, and F. G. De Abajo. “Optical properties of gold nanorings”. In: *Physical Review Letters* 90.5 (2003), p. 057401.
- [20] D. Beaglehole and O. Hunderi. “Study of the interaction of light with rough metal surfaces. I. Experiment”. In: *Physical Review B* 2.2 (1970), p. 309.
- [21] R. Chance, A. Prock, and R. Silbey. “Molecular fluorescence and energy transfer near interfaces”. In: *Advances in Chemical Physics* 37.1 (1978), p. 65.
- [22] L. Novotny and B. Hecht. *Principles of nano-optics*. Cambridge University Press, 2012.
- [23] T. Förster. “Zwischenmolekulare energiewanderung und fluoreszenz”. In: *Annalen der physik* 437.1-2 (1948), pp. 55–75.
- [24] W. Moerner and T. Carter. “Statistical fine structure of inhomogeneously broadened absorption lines”. In: *Physical review letters* 59.23 (1987), p. 2705.
- [25] N. H. Bonadeo, J. Erland, D. Gammon, D. Park, D. Katzer, and D. Steel. “Coherent optical control of the quantum state of a single quantum dot”. In: *Science* 282.5393 (1998), pp. 1473–1476.
- [26] M. Bayer and A. Forchel. “Temperature dependence of the exciton homogeneous linewidth in In 0.60 Ga 0.40 As/GaAs self-assembled quantum dots”. In: *Physical Review B* 65.4 (2002), p. 041308.
- [27] W. Moerner, T. Plakhotnik, T. Irngartinger, M. Croci, V. Palm, and U. P. Wild. “Optical Probing of Single Molecules of Terrylene in a Shpol’kii Matrix: A Two-State Single-Molecule Switch”. In: *The Journal of Physical Chemistry* 98.30 (1994), pp. 7382–7389.
- [28] S. Empedocles and M. Bawendi. “Quantum-confined stark effect in single CdSe nanocrystallite quantum dots”. In: *Science* 278.5346 (1997), p. 2114.

-
- [29] E. Abbe. “Beiträge zur Theorie des Mikroskops und der mikroskopischen Wahrnehmung”. In: *Archiv für mikroskopische Anatomie* 9.1 (1873), pp. 413–418.
- [30] C. Toninelli, K. Early, J. Breimi, A. Renn, V. Sandoghdar, et al. “Near-infrared single-photons from aligned molecules in ultrathin crystalline films at room temperature”. In: *Optics Express* 18.7 (2010), pp. 6577–6582.
- [31] L. Mandel and E. Wolf. *Optical coherence and quantum optics*. Cambridge University Press, 1995.
- [32] K. K. Rebane and I. Rebane. “Peak value of the cross-section of zero-phonon line’s absorption”. In: *Journal of luminescence* 56.1 (1993), pp. 39–45.
- [33] T. Plakhotnik, E. A. Donley, and U. P. Wild. “Single-molecule spectroscopy”. In: *Annual review of physical chemistry* 48.1 (1997), pp. 181–212.
- [34] R. H. Webb. “Confocal optical microscopy”. In: *Reports on Progress in Physics* 59.3 (1996), p. 427.
- [35] R. Loudon. *The quantum theory of light*. Oxford university press, 2000.
- [36] C. Gerry and P. Knight. *Introductory quantum optics*. Cambridge University Press, 2005.
- [37] X. Zou and L. Mandel. “Photon-antibunching and sub-Poissonian photon statistics”. In: *Physical Review A* 41 (1990), pp. 475–476.
- [38] R. H. Brown and R. Twiss. “A test of a new type of stellar interferometer on Sirius”. In: *Nature* 178.4541 (1956), pp. 1046–1048.
- [39] H. Kimble, M. Dagenais, and L. Mandel. “Photon antibunching in resonance fluorescence”. In: *Physical Review Letters* 39.11 (1977), pp. 691–695.
- [40] M. A. Lieb, J. M. Zavislan, and L. Novotny. “Single-molecule orientations determined by direct emission pattern imaging”. In: *JOSA B* 21.6 (2004), pp. 1210–1215.
- [41] T. Taminiau, F. Stefani, F. Segerink, and N. Van Hulst. “Optical antennas direct single-molecule emission”. In: *Nature Photonics* 2.4 (2008), pp. 234–237.
- [42] J. A. Schuller, S. Karaveli, T. Schiros, K. He, S. Yang, I. Kymissis, J. Shan, and R. Zia. “Orientation of luminescent excitons in layered nanomaterials”. In: *Nature nanotechnology* 8.4 (2013), pp. 271–276.
- [43] N. Hartmann. “Kopplung der Strahler In den Plasmonen Oberflächen Vom hinteren Brennebene mikroskopisch untersucht”. PhD thesis.
- [44] L. Novotny. “Allowed and forbidden light in near-field optics. I. A single dipolar light source”. In: *JOSA A* 14.1 (1997), pp. 91–104.
- [45] H. Weyl. “The propagation of electromagnetic waves over a plane conductor”. In: *Ann. der Phys* 60 (1919), pp. 481–500.

- [46] B. Richards and E. Wolf. “Electromagnetic diffraction in optical systems. II. Structure of the image field in an aplanatic system”. In: *Proceedings of the Royal Society of London A: Mathematical, Physical and Engineering Sciences*. Vol. 253. 1274. The Royal Society. 1959, pp. 358–379.
- [47] E. Kretschmann. “Die bestimmung optischer konstanten von metallen durch anregung von oberflächenplasmaschwingungen”. In: *Zeitschrift für Physik* 241.4 (1971), pp. 313–324.
- [48] J. Pitarke, V. Silkin, E. Chulkov, and P. Echenique. “Theory of surface plasmons and surface-plasmon polaritons”. In: *Reports on progress in physics* 70.1 (2007), p. 1.
- [49] C. V. Raman. “A new radiation”. In: *Indian Journal of physics* 2 (1928), pp. 387–398.
- [50] H. J. Bowley, D. L. Gerrard, J. D. Loudon, G. Turrell, D. J. Gardiner, and P. R. Graves. *Practical raman spectroscopy*. Springer Science & Business Media, 2012.
- [51] L. Malard, M. Pimenta, G. Dresselhaus, and M. Dresselhaus. “Raman spectroscopy in graphene”. In: *Physics Reports* 473.5 (2009), pp. 51–87.
- [52] S. M. Angel and M. L. Myrick. “Wavelength selection for fiber optic Raman spectroscopy. Part 1”. In: *Applied optics* 29.9 (1990), pp. 1350–1352.
- [53] S. D. Costa, A. Righi, C. Fantini, Y. Hao, C. Magnuson, L. Colombo, R. S. Ruoff, and M. A. Pimenta. “Resonant Raman spectroscopy of graphene grown on copper substrates”. In: *Solid State Communications* 152.15 (2012), pp. 1317–1320.
- [54] C. Hofmann, A. Nicolet, M. A. Kol’chenko, and M. Orrit. “Towards nanoprobes for conduction in molecular crystals: Dibenzoterrylene in anthracene crystals”. In: *Chemical Physics* 318.1 (2005), pp. 1–6.
- [55] J.-B. Trebbia, H. Ruf, P. Tamarat, and B. Lounis. “Efficient generation of near infra-red single photons from the zero-phonon line of a single molecule”. In: *Optics express* 17.26 (2009), pp. 23986–23991.
- [56] B. Valeur. “Characteristics of fluorescence emission”. In: *Molecular Fluorescence: Principles and Applications* (2002), pp. 34–71.
- [57] J. Macklin, J. Trautman, T. Harris, and L. Brus. “Imaging and time-resolved spectroscopy of single molecules at an interface”. In: *Science* 272.5259 (1996), p. 255.
- [58] A. A. Nicolet, C. Hofmann, M. A. Kol’chenko, B. Kozankiewicz, and M. Orrit. “Single dibenzoterrylene molecules in an anthracene crystal: Spectroscopy and photophysics”. In: *ChemPhysChem* 8.8 (2007), pp. 1215–1220.

-
- [59] L. Fleury, B. Sick, G. Zumofen, B. Hecht, and U. P. Wild. “High photo-stability of single molecules in an organic crystal at room temperature observed by scanning confocal optical microscopy”. In: *Molecular Physics* 95.6 (1998), pp. 1333–1338.
- [60] S. Arrhenius. “Über die Reaktionsgeschwindigkeit bei der Inversion von Rohrzucker durch Säuren”. In: *Zeitschrift für physikalische Chemie* 4 (1889), pp. 226–248.
- [61] K. A. Neyts. “Simulation of light emission from thin-film microcavities”. In: *JOSA A* 15.4 (1998), pp. 962–971.
- [62] E. Lalor. “Conditions for the validity of the angular spectrum of plane waves”. In: *JOSA* 58.9 (1968), pp. 1235–1237.
- [63] W. Lukosz and R. Kunz. “Light emission by magnetic and electric dipoles close to a plane interface. I. Total radiated power”. In: *JOSA* 67.12 (1977), pp. 1607–1615.
- [64] W. Lukosz. “Theory of optical-environment-dependent spontaneous-emission rates for emitters in thin layers”. In: *Physical Review B* 22.6 (1980), p. 3030.
- [65] S. So, W. Choi, L. Leung, and K. Neyts. “Interference effects in bilayer organic light-emitting diodes”. In: *Applied physics letters* 74.14 (1999), pp. 1939–1941.
- [66] A. N. Krasnov. “High-contrast organic light-emitting diodes on flexible substrates”. In: *Applied physics letters* 80.20 (2002), pp. 3853–3855.
- [67] S. Uda and Y. Mushiake. *Yagi-Uda Antenna*. Research Institute of Electrical Communication, Tohoku University, 1954.
- [68] C. Balanis et al. “Antenna theory: A review”. In: *Proceedings of the IEEE* 80.1 (1992), pp. 7–23.
- [69] T. Kosako, Y. Kadoya, and H. F. Hofmann. “Directional control of light by a nano-optical Yagi–Uda antenna”. In: *Nature Photonics* 4.5 (2010), pp. 312–315.
- [70] A. G. Curto, G. Volpe, T. H. Taminiau, M. P. Kreuzer, R. Quidant, and N. F. van Hulst. “Unidirectional emission of a quantum dot coupled to a nanoantenna”. In: *Science* 329.5994 (2010), pp. 930–933.
- [71] Q.-H. Park. “Optical antennas and plasmonics”. In: *Contemporary physics* 50.2 (2009), pp. 407–423.
- [72] D. K. Gramotnev and S. I. Bozhevolnyi. “Plasmonics beyond the diffraction limit”. In: *Nature photonics* 4.2 (2010), pp. 83–91.
- [73] H. F. Hofmann, T. Kosako, and Y. Kadoya. “Design parameters for a nano-optical Yagi–Uda antenna”. In: *New Journal of Physics* 9.7 (2007), p. 217.
- [74] M. Pelton, C. Santori, J. Vucković, B. Zhang, G. S. Solomon, J. Plant, and Y. Yamamoto. “Efficient source of single photons: a single quantum dot in a micropost microcavity”. In: *Physical review letters* 89.23 (2002), p. 233602.

- [75] S. Strauf, N. G. Stoltz, M. T. Rakher, L. A. Coldren, P. M. Petroff, and D. Bouwmeester. “High-frequency single-photon source with polarization control”. In: *Nature photonics* 1.12 (2007), pp. 704–708.
- [76] J. Claudon, J. Bleuse, N. S. Malik, M. Bazin, P. Jaffrennou, N. Gregersen, C. Sauvan, P. Lalanne, and J.-M. Gérard. “A highly efficient single-photon source based on a quantum dot in a photonic nanowire”. In: *Nature Photonics* 4.3 (2010), pp. 174–177.
- [77] T. M. Babinec, B. J. Hausmann, M. Khan, Y. Zhang, J. R. Maze, P. R. Hemmer, and M. Loncar. “A diamond nanowire single-photon source”. In: *Nature nanotechnology* 5.3 (2010), pp. 195–199.
- [78] X.-W. Chen, S. Götzinger, and V. Sandoghdar. “99% efficiency in collecting photons from a single emitter”. In: *Optics letters* 36.18 (2011), pp. 3545–3547.
- [79] F. Bigourdan, F. Marquier, J.-P. Hugonin, and J.-J. Greffet. “Design of highly efficient metallo-dielectric patch antennas for single-photon emission”. In: *Optics express* 22.3 (2014), pp. 2337–2347.
- [80] A. Huber, N. Ocelic, D. Kazantsev, and R. Hillenbrand. “Near-field imaging of mid-infrared surface phonon polariton propagation”. In: *Applied Physics Letters* 87.8 (2005), p. 081103.
- [81] M. Gentile, S. Núñez-Sánchez, and W. L. Barnes. “Optical field-enhancement and subwavelength field-confinement using excitonic nanostructures”. In: *Nano letters* 14.5 (2014), pp. 2339–2344.
- [82] D. Martín-Cano, L. Martín-Moreno, F. J. García-Vidal, and E. Moreno. “Resonance energy transfer and superradiance mediated by plasmonic nanowaveguides”. In: *Nano letters* 10.8 (2010), pp. 3129–3134.
- [83] H. Raether. *Surface plasmons on smooth surfaces*. Springer, 1988.
- [84] L. Novotny and B. Hecht. *Principles of nano-optics*. Cambridge university press, 2012.
- [85] W. H. Weber and G. Ford. “Optical electric-field enhancement at a metal surface arising from surface-plasmon excitation”. In: *Optics letters* 6.3 (1981), pp. 122–124.
- [86] T. Liebermann and W. Knoll. “Surface-plasmon field-enhanced fluorescence spectroscopy”. In: *Colloids and Surfaces A: Physicochemical and Engineering Aspects* 171.1 (2000), pp. 115–130.
- [87] P. L. Stiles, J. A. Dieringer, N. C. Shah, and R. P. Van Duyne. “Surface-enhanced Raman spectroscopy”. In: *Annu. Rev. Anal. Chem.* 1 (2008), pp. 601–626.
- [88] J. N. Anker, W. P. Hall, O. Lyandres, N. C. Shah, J. Zhao, and R. P. Van Duyne. “Biosensing with plasmonic nanosensors”. In: *Nature materials* 7.6 (2008), pp. 442–453.

-
- [89] P. B. Johnson and R.-W. Christy. “Optical constants of the noble metals”. In: *Physical Review B* 6.12 (1972), p. 4370.
- [90] A. Archambault, T. V. Teperik, F. Marquier, and J.-J. Greffet. “Surface plasmon Fourier optics”. In: *Physical Review B* 79.19 (2009), p. 195414.
- [91] F. López-Tejiera, S. G. Rodrigo, L. Martín-Moreno, F. J. García-Vidal, E. Devaux, T. W. Ebbesen, J. R. Krenn, I. Radko, S. I. Bozhevolnyi, M. U. González, et al. “Efficient unidirectional nanoslit couplers for surface plasmons”. In: *Nature physics* 3.5 (2007), pp. 324–328.
- [92] H. Morawitz and M. Philpott. “Coupling of an excited molecule to surface plasmons”. In: *Physical Review B* 10.12 (1974), p. 4863.
- [93] J. Renger, R. Quidant, N. van Hulst, S. Palomba, and L. Novotny. “Free-space excitation of propagating surface plasmon polaritons by nonlinear four-wave mixing”. In: *Physical review letters* 103.26 (2009), p. 266802.
- [94] E. Hecht. “Optics, 4th”. In: *International edition, Addison-Wesley, San Francisco* (2002), pp. 467–473.
- [95] V. N. Pustovit and T. V. Shahbazyan. “Cooperative emission of light by an ensemble of dipoles near a metal nanoparticle: The plasmonic Dicke effect”. In: *Physical review letters* 102.7 (2009), p. 077401.
- [96] S. A. Guebrou, C. Symonds, E. Homeyer, J. Plenet, Y. N. Gartstein, V. M. Agranovich, and J. Bellessa. “Coherent emission from a disordered organic semiconductor induced by strong coupling with surface plasmons”. In: *Physical review letters* 108.6 (2012), p. 066401.
- [97] R. Esteban, A. G. Borisov, P. Nordlander, and J. Aizpurua. “Bridging quantum and classical plasmonics with a quantum-corrected model”. In: *Nature communications* 3 (2012), p. 825.
- [98] A. González-Tudela, P. Huidobro, L. Martín-Moreno, C. Tejedor, and F. García-Vidal. “Theory of strong coupling between quantum emitters and propagating surface plasmons”. In: *Physical review letters* 110.12 (2013), p. 126801.
- [99] T. Holstein and H. Primakoff. “Field dependence of the intrinsic domain magnetization of a ferromagnet”. In: *Physical Review* 58.12 (1940), p. 1098.
- [100] H.-P. Breuer and F. Petruccione. *The theory of open quantum systems*. Oxford university press, 2002.
- [101] C. Sauvan, J.-P. Hugonin, I. Maksymov, and P. Lalanne. “Theory of the spontaneous optical emission of nanosize photonic and plasmon resonators”. In: *Physical Review Letters* 110.23 (2013), p. 237401.
- [102] E. H. Hellen and D. Axelrod. “Fluorescence emission at dielectric and metal-film interfaces”. In: *JOSA B* 4.3 (1987), pp. 337–350.

- [103] W. Weber and C. Eagen. “Energy transfer from an excited dye molecule to the surface plasmons of an adjacent metal”. In: *Optics Letters* 4.8 (1979), pp. 236–238.
- [104] J. R. Lakowicz. “Radiative decay engineering 3. Surface plasmon-coupled directional emission”. In: *Analytical biochemistry* 324.2 (2004), pp. 153–169.
- [105] I. Gryczynski, J. Malicka, Z. Gryczynski, and J. R. Lakowicz. “Radiative decay engineering 4. Experimental studies of surface plasmon-coupled directional emission”. In: *Analytical biochemistry* 324.2 (2004), pp. 170–182.
- [106] J. Lehmann, M. Merschdorf, W. Pfeiffer, A. Thon, S. Voll, and G. Gerber. “Surface plasmon dynamics in silver nanoparticles studied by femtosecond time-resolved photoemission”. In: *Physical review letters* 85.14 (2000), p. 2921.
- [107] D. M. Cano. “Phd thesis- Plasmonic Waveguides: Classical applications and Quantum Phenomena”. PhD thesis.
- [108] P. Goy, J. Raimond, M. Gross, and S. Haroche. “Observation of cavity-enhanced single-atom spontaneous emission”. In: *Physical review letters* 50.24 (1983), p. 1903.
- [109] K. J. Vahala. “Optical microcavities”. In: *Nature* 424.6950 (2003), pp. 839–846.
- [110] N. Lawrence and L. Dal Negro. “Radiation rate enhancement in subwavelength plasmonic ring nanocavities”. In: *Nano letters* 13.8 (2013), pp. 3709–3715.
- [111] A. Grigorenko, A. Beloglazov, P. Nikitin, C. Kuhne, G. Steiner, and R. Salzer. “Dark-field surface plasmon resonance microscopy”. In: *Optics communications* 174.1 (2000), pp. 151–155.
- [112] B. Lamprecht, J. Krenn, G. Schider, H. Ditlbacher, M. Salerno, N. Felidj, A. Leitner, F. Aussenegg, and J. Weeber. “Surface plasmon propagation in microscale metal stripes”. In: *Applied physics letters* 79.1 (2001), pp. 51–53.
- [113] H. Ditlbacher, A. Hohenau, D. Wagner, U. Kreibig, M. Rogers, F. Hofer, F. R. Aussenegg, and J. R. Krenn. “Silver nanowires as surface plasmon resonators”. In: *Physical review letters* 95.25 (2005), p. 257403.
- [114] B. Wild, L. Cao, Y. Sun, B. P. Khanal, E. R. Zubarev, S. K. Gray, N. F. Scherer, and M. Pelton. “Propagation lengths and group velocities of plasmons in chemically synthesized gold and silver nanowires”. In: *ACS nano* 6.1 (2012), pp. 472–482.
- [115] S. I. Bozhevolnyi, V. S. Volkov, E. Devaux, J.-Y. Laluet, and T. W. Ebbesen. “Channel plasmon subwavelength waveguide components including interferometers and ring resonators”. In: *Nature* 440.7083 (2006), pp. 508–511.

-
- [116] C. L. Smith, A. H. Thilsted, C. E. Garcia-Ortiz, I. P. Radko, R. Marie, C. Jeppesen, C. Vannahme, S. I. Bozhevolnyi, and A. Kristensen. “Efficient excitation of channel plasmons in tailored, UV-lithography-defined V-grooves”. In: *Nano letters* 14.3 (2014), pp. 1659–1664.
- [117] E. Moreno, S. G. Rodrigo, S. I. Bozhevolnyi, L. Martin-Moreno, and F. Garcia-Vidal. “Guiding and focusing of electromagnetic fields with wedge plasmon polaritons”. In: *Physical review letters* 100.2 (2008), p. 023901.
- [118] D. F. Pile, T. Ogawa, D. K. Gramotnev, T. Okamoto, M. Haraguchi, M. Fukui, and S. Matsuo. “Theoretical and experimental investigation of strongly localized plasmons on triangular metal wedges for subwavelength waveguiding”. In: *Applied Physics Letters* 87.6 (2005), p. 061106.
- [119] R. F. Oulton, V. J. Sorger, D. Genov, D. Pile, and X. Zhang. “A hybrid plasmonic waveguide for subwavelength confinement and long-range propagation”. In: *Nature Photonics* 2.8 (2008), pp. 496–500.
- [120] F. Bernal Arango, A. Kwadrin, and A. F. Koenderink. “Plasmonic antennas hybridized with dielectric waveguides”. In: *ACS nano* 6.11 (2012), pp. 10156–10167.
- [121] C. D. Bain and G. M. Whitesides. “Molecular-level control over surface order in self-assembled monolayer films of thiols on gold”. In: *Science* 240.4848 (1988), pp. 62–63.
- [122] E. Bermúdez-Ureña, C. Gonzalez-Ballester, M. Geiselmann, R. Marty, I. P. Radko, T. Holmgaard, Y. Alaverdyan, E. Moreno, F. J. García-Vidal, S. I. Bozhevolnyi, et al. “Coupling of individual quantum emitters to channel plasmons”. In: *Nature Communications* 6 (2015).
- [123] S. J. Kress, F. V. Antolinez, P. Richner, S. V. Jayanti, D. K. Kim, F. Prins, A. Riedinger, M. P. Fischer, S. Meyer, K. M. McPeak, et al. “Wedge waveguides and resonators for quantum plasmonics”. In: *Nano letters* 15.9 (2015), pp. 6267–6275.
- [124] A. C. Neto, F. Guinea, N. Peres, K. S. Novoselov, and A. K. Geim. “The electronic properties of graphene”. In: *Reviews of modern physics* 81.1 (2009), p. 109.
- [125] G. W. Semenoff. “Condensed-matter simulation of a three-dimensional anomaly”. In: *Physical Review Letters* 53.26 (1984), p. 2449.
- [126] K. I. Bolotin, K. Sikes, Z. Jiang, M. Klima, G. Fudenberg, J. Hone, P. Kim, and H. Stormer. “Ultrahigh electron mobility in suspended graphene”. In: *Solid State Communications* 146.9 (2008), pp. 351–355.
- [127] M. C. Lemme, T. J. Echtermeyer, M. Baus, and H. Kurz. “A graphene field-effect device”. In: *arXiv preprint cond-mat/0703208* (2007).

- [128] M. Y. Han, B. Özyilmaz, Y. Zhang, and P. Kim. “Energy band-gap engineering of graphene nanoribbons”. In: *Physical Review Letters* 98.20 (2007), p. 206805.
- [129] L. Falkovsky. “Optical properties of graphene”. In: *Journal of Physics: Conference Series*. Vol. 129. 1. IOP Publishing. 2008, p. 012004.
- [130] R. Nair, P. Blake, A. Grigorenko, K. Novoselov, T. Booth, T. Stauber, N. Peres, and A. Geim. “Fine structure constant defines visual transparency of graphene”. In: *Science* 320.5881 (2008), pp. 1308–1308.
- [131] K. Tielrooij, J. Song, S. Jensen, A. Centeno, A. Pesquera, A. Z. Elorza, M. Bonn, L. Levitov, and F. Koppens. “Photoexcitation cascade and multiple hot-carrier generation in graphene”. In: *Nature Physics* 9.4 (2013), pp. 248–252.
- [132] Y.-M. Lin, C. Dimitrakopoulos, K. A. Jenkins, D. B. Farmer, H.-Y. Chiu, A. Grill, and P. Avouris. “100-GHz transistors from wafer-scale epitaxial graphene”. In: *Science* 327.5966 (2010), pp. 662–662.
- [133] A. Klekachev, M. Cantoro, M. Van Der Veen, A. Stesmans, M. Heyns, and S. De Gendt. “Electron accumulation in graphene by interaction with optically excited quantum dots”. In: *Physica E: Low-dimensional Systems and Nanostructures* 43.5 (2011), pp. 1046–1049.
- [134] G. Konstantatos, M. Badioli, L. Gaudreau, J. Osmond, M. Bernechea, F. P. G. de Arquer, F. Gatti, and F. H. Koppens. “Hybrid graphene-quantum dot phototransistors with ultrahigh gain”. In: *Nature Nanotechnology* 7.6 (2012), pp. 363–368.
- [135] F. H. L. Koppens, D. E. Chang, and F. J. García de Abajo. “Graphene Plasmonics: A Platform for Strong Light-Matter Interactions”. In: *Nano Letters* 11.8 (2011), pp. 3370–3377.
- [136] R. Swathi and K. Sebastian. “Resonance energy transfer from a dye molecule to graphene”. In: *The Journal of Chemical Physics* 129.5 (2008), p. 054703.
- [137] G. Gómez-Santos and T. Stauber. “Fluorescence quenching in graphene: A fundamental ruler and evidence for transverse plasmons”. In: *Physical Review B* 84.16 (2011), p. 165438.
- [138] K. A. Velizhanin and A. Efimov. “Probing plasmons in graphene by resonance energy transfer”. In: *Physical Review B* 84.8 (2011), p. 085401.
- [139] L. Stryer and R. P. Haugland. “Energy transfer: a spectroscopic ruler”. In: *Proceedings of the National Academy of Sciences of the United States of America* 58.2 (1967), p. 719.
- [140] R. M. Clegg. “FRET tells us about proximities, distances, orientations and dynamic properties.” In: *Journal of Biotechnology* 82.3 (2002), pp. 177–179.

-
- [141] J. Mukhopadhyay, E. Sineva, J. Knight, R. M. Levy, and R. H. Ebright. “Antibacterial peptide microcin J25 inhibits transcription by binding within and obstructing the RNA polymerase secondary channel”. In: *Molecular Cell* 14.6 (2004), pp. 739–751.
- [142] J. L. Knight, V. Mekler, J. Mukhopadhyay, R. H. Ebright, and R. M. Levy. “Distance-restrained docking of rifampicin and rifamycin SV to RNA polymerase using systematic FRET measurements: developing benchmarks of model quality and reliability”. In: *Biophysical Journal* 88.2 (2005), pp. 925–938.
- [143] B. Schuler and W. A. Eaton. “Protein folding studied by single-molecule FRET”. In: *Current Opinion in Structural Biology* 18.1 (2008), pp. 16–26.
- [144] S. Weiss. “Fluorescence spectroscopy of single biomolecules”. In: *Science* 283.5408 (1999), pp. 1676–1683.
- [145] R. Swathi and K. Sebastian. “Long range resonance energy transfer from a dye molecule to graphene has (distance)- 4 dependence”. In: *The Journal of Chemical Physics* 130.8 (2009), p. 086101.
- [146] M. Zhang, B.-C. Yin, X.-F. Wang, and B.-C. Ye. “Interaction of peptides with graphene oxide and its application for real-time monitoring of protease activity”. In: *Chemical Communications* 47.8 (2011), pp. 2399–2401.
- [147] Y. Wang, Z. Li, J. Wang, J. Li, and Y. Lin. “Graphene and graphene oxide: biofunctionalization and applications in biotechnology”. In: *Trends in Biotechnology* 29.5 (2011), pp. 205–212.
- [148] F. Liu, J. Y. Choi, and T. S. Seo. “Graphene oxide arrays for detecting specific DNA hybridization by fluorescence resonance energy transfer”. In: *Biosensors and Bioelectronics* 25.10 (2010), pp. 2361–2365.
- [149] *DecayFit - Fluorescence Decay Analysis Software 1.3, FluorTools, www.fluortools.com.*
- [150] M. Kreiter, M. Prummer, B. Hecht, and U. Wild. “Orientation dependence of fluorescence lifetimes near an interface”. In: *The Journal of chemical physics* 117.20 (2002), pp. 9430–9433.
- [151] L. Rogobete and C. Henkel. “Spontaneous emission in a subwavelength environment characterized by boundary integral equations”. In: *Physical Review A* 70.6 (2004), p. 063815.
- [152] L. Blanco and F. G. De Abajo. “Spontaneous light emission in complex nanostructures”. In: *Physical Review B* 69.20 (2004), p. 205414.
- [153] L. Gaudreau, K. Tielrooij, G. Prawiroatmodjo, J. Osmond, F. G. de Abajo, and F. Koppens. “Universal distance-scaling of nonradiative energy transfer to graphene”. In: *Nano letters* 13.5 (2013), pp. 2030–2035.

- [154] J. Tisler, T. Oeckinghaus, R. J. Stöhr, R. Kolesov, R. Reuter, F. Reinhard, and J. Wrachtrup. “Single defect center scanning near-field optical microscopy on graphene”. In: *Nano letters* 13.7 (2013), pp. 3152–3156.
- [155] X. Liu, G. Wang, X. Song, F. Feng, W. Zhu, L. Lou, J. Wang, H. Wang, and P. Bao. “Energy transfer from a single nitrogen-vacancy center in nanodiamond to a graphene monolayer”. In: *Applied Physics Letters* 101.23 (2012), p. 233112.

List of Figures

1.1	Schematic illustration of the absorption and emission processes	14
1.2	Excited-state population behaviour at resonant excitation for different values of the damping rate γ_C	18
1.3	Jablonski diagram of a three-level molecule	20
1.4	Absorption (yellow) and emission (red) spectra of single molecules embedded in solid matrix at room temperature	22
1.5	(a) Image dipoles produced by a reflecting surface for small surface-emitter distance (b) Electric field of an emitter nearby an interface . . .	24
1.6	Distance dependence of the spontaneous emission lifetime of Eu^{3+} ions in the vicinity of an Ag mirror obtained by Drexhage et al in 1974 . . .	26
2.1	3-D intensity map of a single molecule sample	30
2.2	Confocal microscope	32
2.3	Scheme of the combined setup	33
2.4	Sample images taken with the setup	35
2.5	(a) Comparison of the photon number distributions (b) Second-order correlation functions $g_2(\tau)$ for coherent, thermal and quantum light. . .	36
2.6	(a) Schematic diagram of a HBT (b) $g_2(\tau)$ function at room temperature	38
2.7	(a) Schematic diagram of the power distribution in the upper and lower half spaces (b) Schematic of the projection of angular emission by an imaging lens onto the BFP	39
2.8	Schematic of the BFP imaging setup	40
2.9	(a) Simulated and (b) Observed angular emission pattern of a horizontal dipole	41
2.10	Dispersion relation for an SPP mode (left). Kretschmann configuration (right).	42
2.11	Schematic of the Kretschmann setup in the lab	43
2.12	(a) Observed ATR curves (b) Simulated ATR curves	44
2.13	Energy level diagram showing different types of scattering processes: Rayleigh and Raman scattering	45
2.14	(a) Raman spectrum of graphene (b) The number of layers can be distinguished by the 2D/G-bands intensity ratio and inspecting the lineshape of the 2D-band.	46

3.1	(a) Chemical structures of DBT and Ac (b) Jablonsky diagram for a single DBT molecule embedded in anthracene	47
3.2	Emission spectrum of a single DBT molecule embedded in anthracene at room temperature	48
3.3	(a) SEM image of a co-sublimated DBT:Ac crystal (b) Microscope image of a sample produced by spin coating	49
3.4	(a) Whitelight (b) Widefield (c) Confocal scan (d) Intensity profile for a DBT molecule embedded in anthracene	51
3.5	Measured photon anti-bunching from single DBT molecule emission without any background correction (grey points)	52
3.6	Detected rates for the fluorescence of a single DBT molecule plotted as a function of the excitation intensity	53
3.7	Linewidth of a DBT molecule at a temperature of 2.9K	53
4.1	Thin-film structure: active medium containing the emitter with refractive index n_e and thickness d_e situated between a number of M and N layers	56
4.2	(a) wavevector k of a plane wave making an angle θ with the z -axis (b) TE and TM polarizations	57
4.3	Dipole position in the resultant three-layer structure	58
4.4	Schematic depicting the mapping of k-vectors in the BFP	61
4.5	Reference sample configuration and BFP patterns	63
4.6	Power density for a DBT molecule embedded in anthracene at different distances from the interface with air	64
4.7	One-mirror configuration	65
4.8	Simulated radiation patterns by varying the thickness of the spacer layer	66
4.9	Power density as a function of polar angle θ for a DBT molecule embedded in semi-infinite medium with refractive index $n=1.5$	67
4.10	Power collected over polar angles from 0 to β , for a DBT molecule embedded in semi-infinite medium with refractive index $n=1.5$	67
4.11	Angular emission patterns for 3 particular cases with different thickness of the PVA spacer layer	68
4.12	Experimentally observed angular emission patterns with a PVA spacer layer thickness of 75 nm for (a) High concentration and (b) Single molecule concentration of DBT molecules in anthracene. (c) Simulated version	69
4.13	Experimentally observed angular emission patterns with a PVA spacer layer thickness of 340 nm for (a) High concentration and (b) Single molecule concentration of DBT molecules in anthracene. (c) Simulated version	70

4.14	Experimentally observed angular emission patterns with a PVA spacer layer thickness of 460 nm for (a) High concentration and (b) Single molecule concentration of DBT molecules in anthracene. (c) Simulated version	70
4.15	Yagi-Uda configuration	71
4.16	Double mirror configuration	73
4.17	Variation of power density for polar angle θ with the distance of the emitter from the director scanned from 50-100 nm	74
4.18	Variation of power density for polar angle θ with the distance of the emitter from the director scanned from 300-350 nm	74
4.19	(a) Power as a function of polar angle θ for the optimal emitter-director distances for given thicknesses of the director layer (b) Power collected in angular apertures from 0 to β for the same cases	76
4.20	(a) Experimental and (b) Simulated angular emission pattern for a Double-mirror configuration	77
4.21	Detected rates obtained as a function of excitation intensity for DBT molecules embedded in the double mirror configuration	77
5.1	SPP field distributions.	80
5.2	Dispersion relation of gold	82
5.3	SPP excitation schemes	83
5.4	Simulation demonstrating the evolution of the dip in reflectivity with thickness of the metal	84
5.5	Sample schematic for coupling of DBT dye molecules to a planar gold film	87
5.6	SPCE due to coupling of DBT molecules to plasmons in gold	89
5.7	Distribution of lifetimes of DBT molecules embedded in anthracene spin coated over a planar gold surface	90
5.8	Simulated dispersion relation for PMMA and anthracene over gold . . .	91
5.9	Reflectivity curves obtained for PMMA layer anthracene layer over gold	91
5.10	Obtained reflectivity curves and dispersion curve for high concentration of DBT molecules over gold	92
5.11	Plasmonic concentric-ring resonators	94
5.12	Images of the plasmonic resonators	95
5.13	Spectral response of the resonators	96
5.14	Fabrication process for plasmonic wedge waveguides	98
5.15	Wedge waveguide structure mode distribution (a) without anthracene (b) with 60 nm anthracene layer (c) Purcell enhancement with height h (d) Variation in propagation length with thickness of anthracene layer. .	99
5.16	(a) Whitelight (b) Widefield and (c) confocal scan images for wedge waveguides	100

6.1	(a) Lattice model (b) Scanning probe microscopy image of graphene . . .	101
6.2	Graphene band-structure	102
6.3	Energy diagram of a DBT molecule in free space and nearby an undoped graphene monolayer sheet	103
6.4	Measured Raman spectrum of the CVD graphene sample	105
6.5	Measurements with DBT molecules over graphene	106
6.6	Probability density function of single molecule excited-state lifetimes on (a) the reference sample and (b) the graphene monolayer sheet (c) The assumed molecule depth distribution inside anthracene crystals used in the theoretical model (d) The uncertainty in position measurement Δd .	108